HIGH ENERGY GAMMA RAY PRODUCTION IN PROTON INDUCED REACTIONS AT ENERGIES OF 104, 145 AND 195 MeV

By

JAMES EDWARD CLAYTON

A DISSERTATION

Submitted to
Michigan State University
in partial fulfillment of the requirements
for the Degree of

DOCTOR OF PHILOSOPHY

Department of Physics and Astronomy

1991

ABSTRACT

HIGH ENERGY GAMMA RAY PRODUCTION IN PROTON INDUCED REACTIONS AT ENERGIES OF 104, 145 AND 195 MeV

by

James Edward Clayton

The production of high energy gamma rays ($E_\gamma \geq 20$ MeV) was studied using two barium fluoride (BaF_2) crystal detectors. Each detector consists of two right cylinders of the inorganic scintillator BaF_2 12.5 cm in diameter and 11.45 cm in length. The response of the BaF_2 detector to gamma rays in the range from 75–200 MeV was calibrated using the tagged photon facility of the Saskatchewan Accelerator Laboratory at the University of Saskatchewan. The measured detector response and efficiency were then compared to the experimental data using electromagnetic shower code EGS4. The resolution of the BaF_2 crystal is approximately $4.3 \pm 0.3\%/\sqrt{E_p}$ where E_p is the most probable energy deposition in the BaF_2 crystal. A method of reestablishing the calibration using cosmic ray muons passing through the detector is also presented. This method is necessary for measurements which require high full scale energies where extrapolations from standard gamma ray sources energies are unreliable.

The BaF_2 detector was used to study photon production from the following proton induced reactions: p + C, p + Zn and p + Pb at incident energies of 104, 145 and 195 MeV. The reaction of p + ^{2}H was also investigated at bombarding energies of 145 and 195 MeV. The double differential photon cross sections are not the usual exponential

shape expected from heavy-ion reactions but have a power law dependence. This type of behavior has been predicted in a theoretical model which uses first chance neutron–proton bremsstrahlung as the production mechanism. The maximum energy available to create a photon is given by a simple expression which incorporates the kinetic energy of the system in the nucleon–nucleon center-of-mass system and the Fermi momentum of the target nucleons. The energy spectra measured with the ^{2}H target are important since these spectra yield information about free npγ bremsstrahlung as well as p + nucleus gamma ray production processes. The energy spectra from the ^{2}H target will permit theoretical calculations to investigate the importance of the internal momentum distribution of colliding nucleons.

To my wife *Cynthia*

Acknowledgements

I would like to offer my sincere thanks to my advisor, Walter Benenson. His calm demeanor and thorough understanding of science and life helped me in completing this degree. I would like to thank him for the support he gave me during some of the more difficult times in my stay at the laboratory.

This work was shaped by important contributions from John Stevenson and Takeshi Murakami. Their patience and guidance helped me in so many ways that they will never be aware of. Special credit has to be given to "Ken" who taught me much of what I know about experimental techniques in Nuclear Physics.

There are many others who are deserving of recognition for their part in this project. Wolfgang Bauer and George Bertsch for their help and guidance in the calculation of the gamma energy spectra and the interpretation of the results. Dave Morrissey for his help in understanding the data in this work and with other measurements. Ron Fox and Andrew Vandermolen for all their help with the data acquisition system here at the NSCL and at IUCF. Michael Maier for his many ideas on detectors and electronics and their implementation. Craig Snow, Len Morris and Steve Bricker who turned my ideas and sketches into something useful.

I can honestly say that I really enjoyed the many people that I have worked with here at the NSCL. The list is not exhaustive but I have to acknowledge some of the major contributors, Mike Mohar, Mats Cronqvist, Jeff Karn, Raman Pfaff, Gary Westfall, Ken Wilson, John Winfield, and Brian Young, who have helped, encouraged and shared ideas with me. Without their knowledge and support this project would still be on tape.

I owe a great debt to my parents and most of all to my wife who put up with all the insanity that comes with graduate student life.

Contents

List of Tables

List of Figures

Chapter 1

Introduction

I Introduction

Since the discovery of high energy gamma rays ($E_\gamma \geq 20$ MeV) in intermediate heavy-ion collisions, the thrust of both the experimental and theoretical research has concentrated on understanding the production mechanism. The experimental discovery was made independently by two research groups one at GSI [Grosse 85] and one at Michigan State University [Beard 85]. The study of these photons is quite intriguing since, unlike subthreshold pions and charged particles, the photons do not interact strongly within the surrounding nuclear matter and are not reabsorbed. This property gives the photon the distinct advantage that it can serve as a relatively clean probe of the reaction dynamics in intermediate heavy ion reactions.

Several theoretical models have been proposed to explain the production of high energy gamma rays at these bombarding energies. The assumption for the vast majority of these models is that the production mechanism is nucleon–nucleon or nucleus–nucleus bremsstrahlung which happens during the early stages of the collision.

Early model calculations by Vasak, Mueller, and Greiner [Vasak 85] suggested that the production mechanism might be coherent nucleus–nucleus bremsstrahlung. In this model the sudden deceleration of the target and projectile produces high energy

photons with a quadrupole angular distribution. This deceleration in the early stages of the collision also offered the possibility of determining the nuclear "stopping time" via the gamma ray production cross section.

More recent models of high energy gamma ray production have assumed that the microscopic production mechanism is incoherent neutron–proton bremsstrahlung from the nucleon–nucleon collisions within the heavy ion reaction. For example, Bauer et al. [Bauer 86b] conducted a dynamical study based on the Boltzmann–Uehling–Uhlenbeck equation, which describes the time evolution of the nucleon phase space density during the collision process. Nakayama and Bertsch [Nakayama 86] performed calculations using infinite nuclear matter approximations with first–chance neutron–proton interactions, and Remington et al. [Remington 87] incorporated the semiclassical bremsstrahlung formula into the Boltzmann Master Equation [Harp 68].

Nifenecker and Bondorf [Nifenecker 85] in their ground breaking paper suggested a model in which the photon production was attributed to multiple scattering during the latter stages of the collision. In this approach the gamma rays are produced during incoherent nucleon–nucleon collisions within a recoiling fireball formed from the target and projectile nucleons. The kinetic energy of participating nucleons is assumed to be converted to the thermal energy of the fireball; this allows photons of relatively high energy to be produced, and the angular distribution is expected to be isotropic in the rest frame of the moving source. Neuhauser and Koonin [Neuhauser 87], combining a fireball model with the elementary nucleon–nucleon bremsstrahlung cross section, found reasonable agreement with experimental data.

In a more recent calculation, J. Randrup and R. Vandenbosch [Randrup 88] extended a model previously developed for pre-equilibrium nucleon emission. This model follows a stochastic exchange of nucleons and includes photon production as a perturbative effect. The photons arise from bremsstrahlung radiation associated with

proton-neutron scattering of the transferred nucleons as they propagate through the receptor nucleus. They found moderate agreement in a comparison of their calculations to experimental data.

Shortly after the first high energy gamma ray observations by Beard *et al.* [Beard 85] with the NSCL Enge Split-pole spectrograph, it became clear that a better detection scheme was needed for further investigation of this phenomenon. The development of the MSU plastic Čerenkov stack detector was conceived and carried out by John Stevenson. This detector was used by the research group at MSU for several ground breaking measurements studying high energy gamma ray production in intermediate energy heavy ion collisions [Stevenson 86,Lampis 88,Tam 88,Tam 89a,Clayton 89]. These measurements ranged from very light systems ^{2}H + C [Tam 89a] to the heaviest system studied as of this date ^{136}Xe + Sn. Bombarding energies also ranged from E/A= 20 MeV [Stevenson 86] to the highest energies used in these studies E/A= 124 MeV [Clayton 89].

The calibration of the Čerenkov detector at the tagged photon facility of the University of Illinois has shown that the resolution of this detector was not as good as expected, which meant that for continued studies a better solution should be investigated. At about the same time, BaF_2 , a new scintillator material was brought to the marketplace as a detector for photons. This thesis describes the calibration and use of the new BaF_2 detector system in the study of high energy gamma ray production in proton induced reactions.

The proton nucleus bremsstrahlung studies are important since the colliding system is easier to model and will yield information on the more complex heavy ion reactions. One of the simplest cases is p + d since the gamma ray energy spectra can yield information about the free $p + n \rightarrow \gamma$ cross section as well as the contribution to the cross section from the internal momentum distribution of the neutron in the nucleus. The information on the number gamma rays and their angular distribution

can help the theorists in their calculations on free pnγ processes. For reactions with heavy targets the internal momentum of both the target and projectile need to be accounted for in a complete calculation to completely characterize the gamma ray production cross section.

II Thesis Organization

This thesis will be organized as follows: Chapter 2 of this work covers the development of the gamma ray telescope and its contemporaries used by other research groups in their studies of high energy gamma ray production. Included will be a discussion of the advantages and drawbacks of the various detectors used by the experimental research groups.

Chapter 3 describes the hardware and electronic set-up used in the design and calibration of the BaF_2 crystal at the tagged photon facility at the Saskatchewan Accelerator Laboratory. A method of reproducing the energy calibration using the passage of cosmic ray muons along the diameter of the BaF_2 will also be presented.

Chapter 4 presents a historical overview of the field of high energy gamma ray production. Chapter 4 also presents the hardware, electronics set-up and data from an experiment performed at the Indiana University Cyclotron Facility studying bremsstrahlung photon production from proton induced reactions. This study is the confirmation experiment for results from Kwato *et al.* [Kwato 88a] and Pinston *et al.*[Pinston 89] which found a discrepancy between their results and the earlier measurements of Edgington and Rose [Edgington 66]. Results will also be presented from a measurement on p + d at incident energies of 145 and 195 MeV. These measurements give insights into the free neutron–proton bremsstrahlung cross section.

Chapter 5 deals with comparison and contrasts of this measurement to all the other

known data from proton induced reactions. Finally, the summary and conclusions are in Chapter 6.

Chapter 2

Detectors for High Energy Gamma Ray Measurement

I Introduction

The detection of photons in the energy range from 20 to 200 MeV produced in nucleus-nucleus collisions presents unique problems for the design and implementation of the detector system. The first major difficulty is the production cross section for these high energy gamma rays is approximately 10^5 –10^6 times less than the yield of low energy photons and particles. This background of low energy photons, fast and slow neutrons, and charged particles has lead to a variety of detection schemes by the several experimental groups studying this phenomenon. The various methods for detecting and identifying these high energy photons from the millieu of background particles will be discussed in this chapter. Also included in this chapter will be a discussion of the advantages and disadvantages of these detector systems.

II Detection of High Energy Gamma Rays

The behavior of high energy photons in a material is different from charged particles, and this difference arises from the fact that the photon lacks electric charge which eliminates the possibility of the many inelastic collisions with atomic elec-

trons. The gradual slowing of charged particles through the continuous interactions of the incident particle with the many absorber atoms is a characteristic of charged particle interaction in matter. Instead, the photon can undergo complete or partial energy transfer to a single electron. These energy loss mechanisms give rise to abrupt changes in the gamma ray history, in that the photon disappears entirely or is scattered through a significant angle. The main interactions of x-rays and gamma-rays in material are:

1. Photoelectric Effect.
2. Compton Scattering (which includes Thomson and Rayleigh Scattering).
3. Pair Production.

Other reactions are possible such as nuclear dissociation reactions, for example (γ,n), but these are small compared with the major three and will be neglected in this work.

These reactions explain two of the main features of x-ray and gamma-ray interaction in matter:

1. X-rays and γ-rays are much more penetrating than charged particles.
2. A beam of x-rays or γ-rays for the most part is not degraded in energy as it traverses through a given thickness of material; only its intensity is reduced.

The former is due to the much smaller cross section for these three processes relative to the inelastic cross section for atomic electron collisions, while the latter is due to the nature of the three processes in that the photon is usually removed from the incident beam entirely, either by absorption or scattering. The relative importance of these three processes in different materials is illustrated in Figure 2.1 [Evans 55]. In Figure 2.1, the curve on the left separates the energy region at which the photoelectric cross

section and Compton Scattering cross section are equally probable as a function of the atomic number of the interacting material. The curve on the right side of Figure 2.1 divides the energy region for which Compton Scattering and Pair Production are equally probable as a function of the atomic number of the absorber material. It is clear that for $E_\gamma \geq 20$ MeV, the process of photoelectric absorption is negligible and the Compton Scattering cross section is small in comparison to the pair production cross section. Since the pair production cross section for an absorber material is proportional to Z^2, the best choices are for materials with a high atomic number. As detectors for high energy gamma rays, the majority of the research groups have used some of the many available inorganic scintillator materials such as NaI(Tl), CsI, BGO (Bismuth Germinate Oxide), and BaF_2. Figure 2.2 shows the relative efficiency for photons undergoing Compton scattering and pair production for the scintillator BaF_2. It can be seen that for the photons of interest $E_\gamma \geq 20$ MeV, pair production is the dominant process.

III Calorimetry with Inorganic Scintillators

A device that measures the total energy deposited by a particle or group of particles is known as a calorimeter, and for the detection of high energy photons, scintillator crystals comprised of alkali halide compounds have been used widely for this purpose. The calorimeter or shower detector operates on the basis of the formation of a large number of electron-positron pairs, "the shower", inside the active part of the detector. This type of detector is usually comprised of materials with a large atomic number Z to enhance the production of e^+e^- pairs. The number of particles, photons and e^+e^- pairs, present after t radiation lengths of a detector medium is

$$N(t) = 2^t \tag{2.1}$$

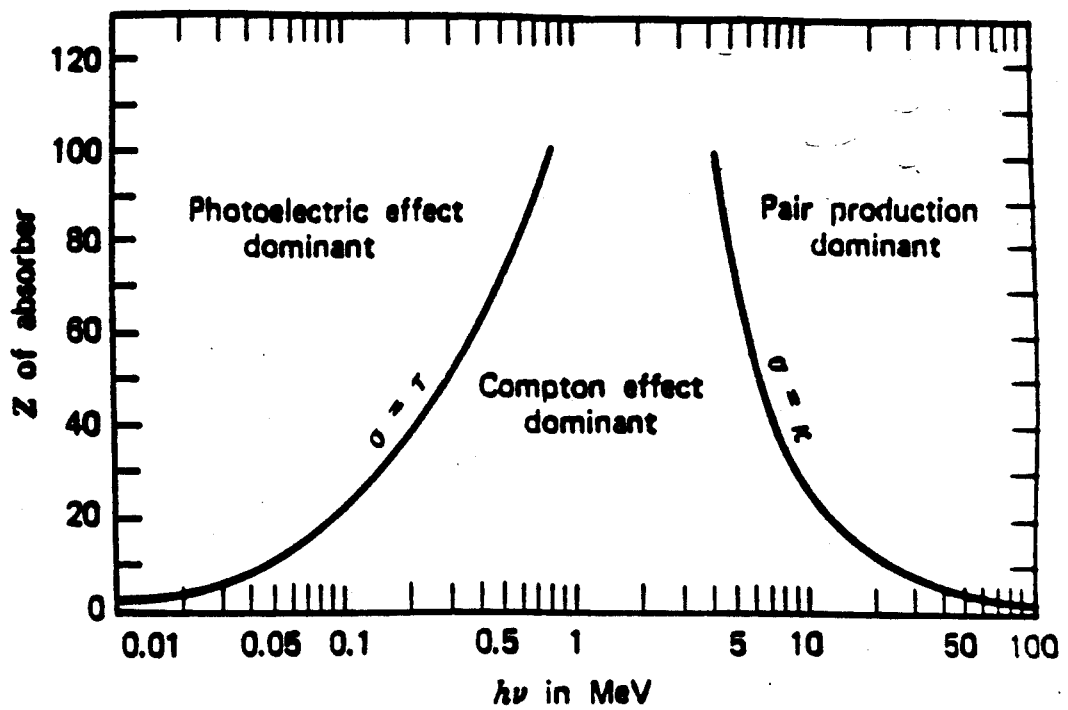

Figure 2.1: Relative importance of the three major types of photon interactions as a function to the incident photon energy and the atomic number of the absorber medium [Evans 55].

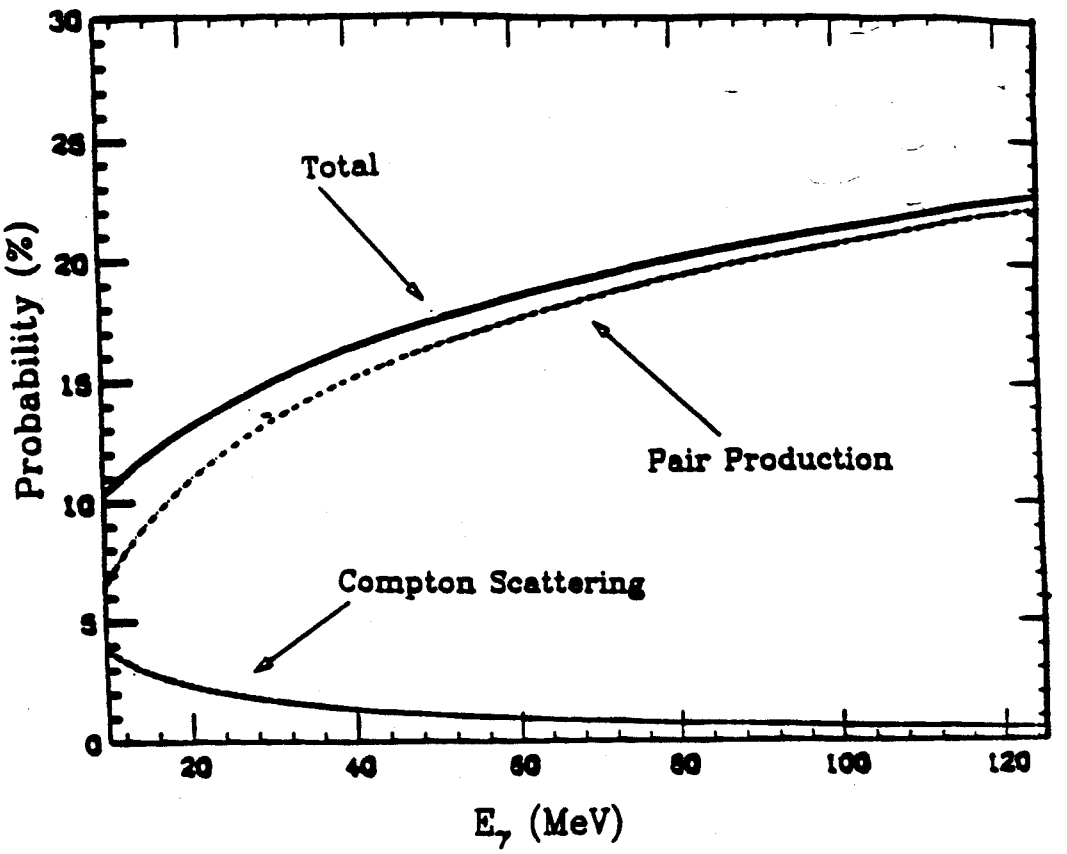

Figure 2.2: The relative probability of Compton Scattering vs. pair production in the inorganic scintillator BaF_2 .

Table 2.1: Radiation lengths and minimum ionization energy loss for common detector materials. [Leo 87]

Material	gm/cm^2	cm	dE/dx min $\frac{MeV}{gm/cm^2}$
NaI(Tl)	9.49	2.59	1.32
BaF_2	9.91	2.05	1.35
BGO $Bi_4Ge_3O_13$	7.98	1.12	1.27
Polystyrene scintillator (CH)	43.8	42.4	1.95
Lucite $C_5H_8O_2$	40.5	34.4	1.95
Carbon	42.7	18.8	1.78
Iron	13.8	1.76	1.48
Lead	6.37	0.56	1.13

A radiation length is defined as distance over which the electron energy is reduced by a factor 1/e due to radiation losses only [Leo 87]. In the limit that collisional losses can be ignored relative to radiative losses the radiation length L_{rad} for a material is given by:

$$\frac{1}{L_{rad}} \simeq \left(4Z(Z+1)\frac{\rho N_a}{A}\right) r_e^2 \alpha \cdot \ln(183Z^{-1/3}) \qquad (2.2)$$

The radiation lengths for some common materials are given in Table 2.1. Within the electromagnetic shower, the number of electrons and positrons is roughly the same. In order to contain the electromagnetic shower produced, the size of the detector must be several radiation lengths deep. The lateral development of the shower is not significant until the end of the shower is reached. It has been shown that 90% of the electromagnetic shower is contained in a cylinder less than one L_{rad} up to the maximum energy deposition [Fabjan 82]. Beyond this point the electrons are increasingly affected by multiple scattering, and the lateral shower size scales with the Molière

Table 2.2: Characteristics for common scintillators.

Scintillator Material	Density g/cm^3	Wavelength of Maximum Emission λ (nm)	Index of Refraction at λ_{max}	Decay Constant (μs)
NaI(Tl)	3.67	415	1.85	0.23
CsI(Tl)	4.51	550	1.80	1.0
CsI Pure	4.51	305 fast 400 slow	1.79	10^{-3} 1.0
BaF_2	4.9	220 310	1.49	$0.6x10^{-3}$ 0.620
BGO	7.13	480	2.15	0.3

radius which is approximately given in Equation 2.3 as:

$$\rho_M \simeq \frac{7A}{Z}\, g/cm^2 \tag{2.3}$$

The propagation of photons in the shower causes deviations from Molière radius scaling [Amaldi 87]. However, roughly 95% of the shower is contained in a cylinder with a radius of $2\rho_M$. Therefore, the detector must be collimated to minimize the portion of the shower escaping from the active volume. Table 2.2 gives some of the properties of the common scintillators used in gamma ray detection. As can be seen in the Table 2.2 these detectors have similarities regarding high atomic number and their emitted wavelengths, but there are subtle differences as will be discussed below.

A The Scintillation Mechanism

The scintillation mechanism in inorganic materials depends on the energy states determined by the crystal lattice of the detector material. The electrons in the material have only discrete bands available in materials classified as insulators or semiconductors. The lower band is called the valence band and represents those electrons that are bound to lattice sites, whereas the conduction band represents those electrons that have sufficient energy to move freely throughout the crystal. An intermediate

band of energies between the valence and conduction band exists, is called the forbidden band, in which electrons can never be found in a pure crystal. When energy is absorbed by the crystal, this can result in the elevation of an electron from its normal position in the valence band into the conduction band. In a pure crystal, the return of the electron to the valence band via the emission of a photon is an inefficient process. Since typical band widths are such that the resulting photon wavelength would be too short to lie in the visible light range.

In a effort to enhance the probability of the crystal emitting a photon with energy in the visible portion of the electromagnetic spectrum, small amounts of an impurity are commonly added to inorganic scintillators. These impurities are called activators, and activators create special sites within the lattice at which the normal band structure is modified from the pure crystal structure. As a result there will be energy states created within the forbidden band, and thereby, giving the electron a path to deexcite back to the valence band. Since the energy in the forbidden band is less than the conduction band, this transition can now give rise to a visible photon and therefore, the crystal can serve as a scintillation detector. NaI(Tl) and CsI(Tl) or CsI(Na) are examples scintillators which use an activator to bring the scintillation light output into the visible spectrum.

B NaI(Tl) Crystal Detector

Thallium-activated sodium iodide (NaI(Tl)) crystals are often used for measurements of low energy gamma rays. NaI(Tl) is characterized by excellent energy resolution, high light output and the possibility of growing large volume crystals. As is the case with all detectors of this type, the incident photon is converted to an e^+e^- pair either by a separate converter or in the active volume of the NaI(Tl) crystal, and an electromagnetic shower is formed. The total light output of crystal assuming

complete containment of the electromagnetic shower is directly related to the energy of the incident photon.

The primary disadvantage of NaI(Tl) is that it is hygroscopic; if exposed to the atmosphere, it will deteriorate due to absorption of water. If exposed to sunlight it will develop F-centers, which inhibit the production of scintillation light. It is also sensitive to thermal neutrons because of the large capture cross section of Iodine, and the large neutron background in heavy-ion collisions make NaI(Tl) a poor choice. Attempts can be made to shield the detector from the thermal neutron background, but this can exacerbate the situation due to all the capture gamma rays produced in the shielding material. The most serious problem with NaI(Tl) is the slow risetime of the scintillation light; this fact gives NaI(Tl) poor time resolution for large volume crystals and makes discrimination of fast neutrons from gamma rays difficult with time-of-flight (TOF) methods. The time resolution for a 25.4 cm diameter and 30.5 cm long NaI(Tl) crystal is approximately 5 ns full width at half maximum (FWHM). The long decay time for NaI(Tl) scintillation spectrum requires either a long acceptance gate on charge sensitive analog-to-digital converters (QDC) or a long shaping time for amplifiers used with peak sensing ADCS which can cause pile-up problems in high rate experiments.

The energy resolution of NaI(Tl) is excellent and is limited by the loss of secondary particles produced in the electromagnetic shower. Figure 2.3 shows the response of a right cylinder of NaI(Tl) 15 cm in diameter and 20 cm in length (7.72 L_{rad}) illuminated by monochromatic photons [Bertholet 87]. In measurements on high energy gamma ray production in heavy ion collisions Bertholet *et al.* [Bertholet 87] have combined a large block of NaI(Tl) with a BaF_2 converter. The converter is "active", in the sense that the energy lost by the e^+e^- pair is included in the total energy sum and a coincidence between the converter and the NaI(Tl) crystal is required. The resolution obtained

with this telescope detector scheme is moderate, $6.5\%/\sqrt{E_{inc}}$. The response for the telescope configuration is shown in Figure 2.3. The addition of a BaF_2 converter is an attempt to improve the time resolution for the detector system since BaF_2 exhibits a fast risetime signal.

C CsI

Cesium Iodide is another alkali halide that has gained popularity as a scintillation material. It is commercially available doped with thallium or sodium as an activator material. Recently it is also available in a pure form which exhibits a fast component in its scintillation light output. CsI has a slightly larger γ-ray absorption coefficient per unit volume than NaI. It is also less brittle than NaI(Tl) so it can be exposed to larger extremes of shock and vibration. When cut into thin sheets, CsI may be bent into various shapes without fracturing. Since it is grown in a process similar to NaI(Tl), it can be made into very large volumes, and it costs roughly the same per cm^3 as NaI(Tl). The energy resolution for pure CsI is poor relative to NaI(Tl), which is due to the low light output. No experimental group has published any experimental data using a large volume CsI detector. However, it has been used in a recent measurement of gamma ray production on various tin isotopes at Michigan State University, and the data are being analyzed at this time. Timing measurements have been made for a small volume pure CsI crystal and a value of 750 ps FWHM was obtained

D BGO

In the late 1970's a new scintillator became commercially available, $Bi_4Ge_3O_{12}$ (BGO), and has been rapidly growing in applications for gamma ray measurements. BGO has the highest gamma ray absorption coefficient of all the common inorganic scintillators.

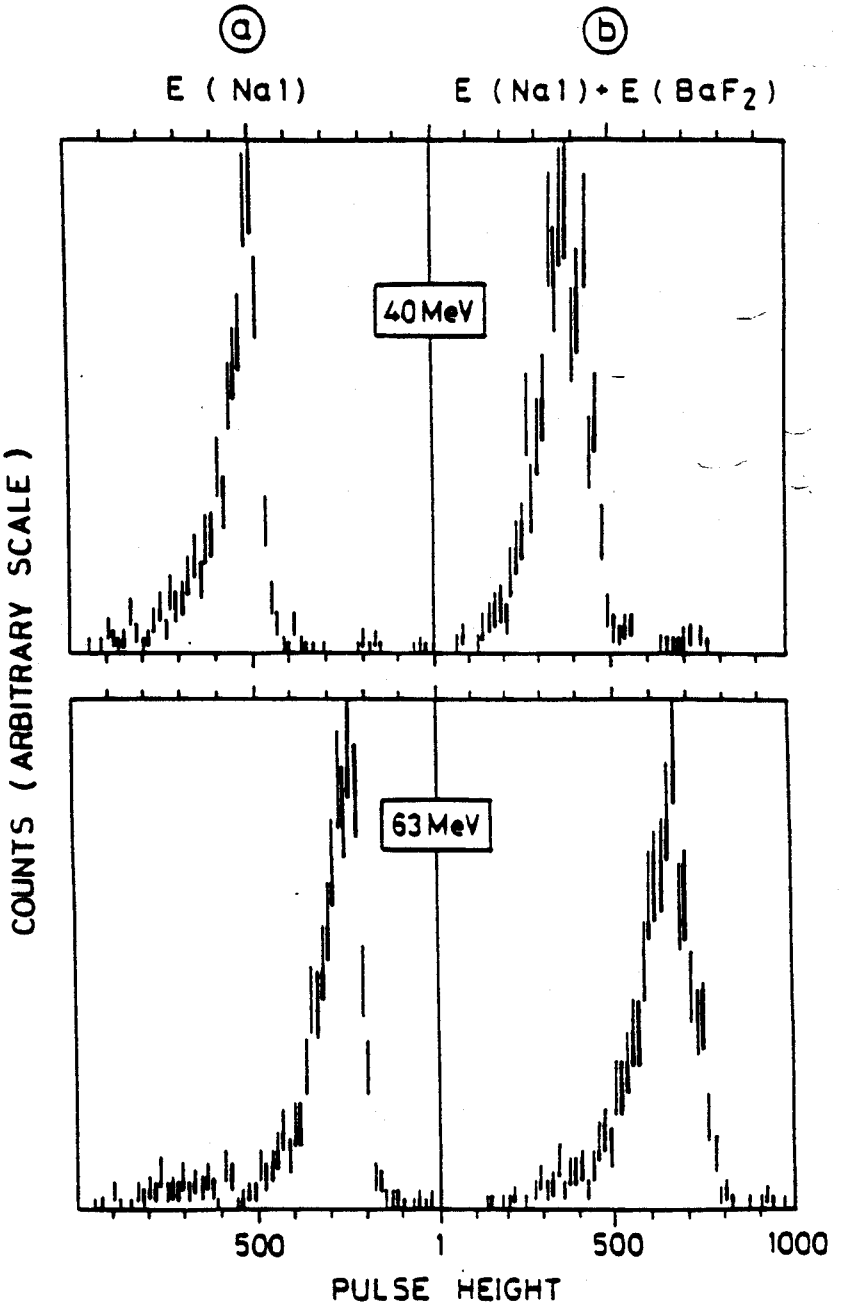

Figure 2.3: The response function for a NaI(Tl) crystal (a) 15 cm in diameter and 20 cm in length to tagged photons at 40 and 63 MeV. The response of the NaI(Tl) + BaF_2 converter telescope to photons at 40 and 63 MeV [Bertholet 87].

It has a very high density (7.13 g/cm^3) and a radiation length, of 1.13 cm, and these two factors would yield reduction of approximately 16 times in the volume necessary to contain a gamma ray shower when compared to NaI(Tl). BGO is non-hygroscopic, inert, and resistant to vibration and other physical shocks. The drawbacks for BGO are its low light output relative to NaI(Tl) (12-14)%, large self absorption of its scintillation light, and slow risetime. Time resolution of approximately 3 ns FWHM is possible with BGO. Due to the low light output, the energy resolution is worse than that obtained for NaI(Tl). BGO has energy resolution of about about 15% FWHM for ^{137}Cs. BGO has been used for some measurements on high energy gamma ray production [Hanold 88] and [Murakami 89]. The results obtained with these crystals were in reasonable agreement with experimental results from other research groups. The response function for a 7.6 cm diameter 7.6 cm long right cylinder BGO crystal is shown in Figure 2.4. The use of BGO as a detector has been recently abandoned in high energy gamma ray production studies because of the availability of large volume BaF_2 crystals.

E BaF_2

As a scintillation detector the inorganic crystal BaF_2 has been known for quite some time [Faruki 71]. However, since the discovery of the fast component in the scintillation light of BaF_2 [Laval 83] it has received much attention as a scintillation detector for gamma rays [Wisshak 84,Novotny 87,Agodi 88], charged particles [Agodi 88,Murakami 86,Karwowski 86], and also neutrons [Madey 87,Matulewicz 89,Kubota 89]. BaF_2 has excellent time resolution approaching 80 ps Full Width at Half Maximum (FWHM) for small crystals [Laval 83] and 400 ps FWHM for large crystals [Wisshak 84]. The scintillator has a relatively high density (4.89 g/cm^3), and the high atomic number of Ba (56) give BaF_2 good stopping power for gamma rays (radiation length L_{rad} = 2.05 cm). Karle, Knoop and

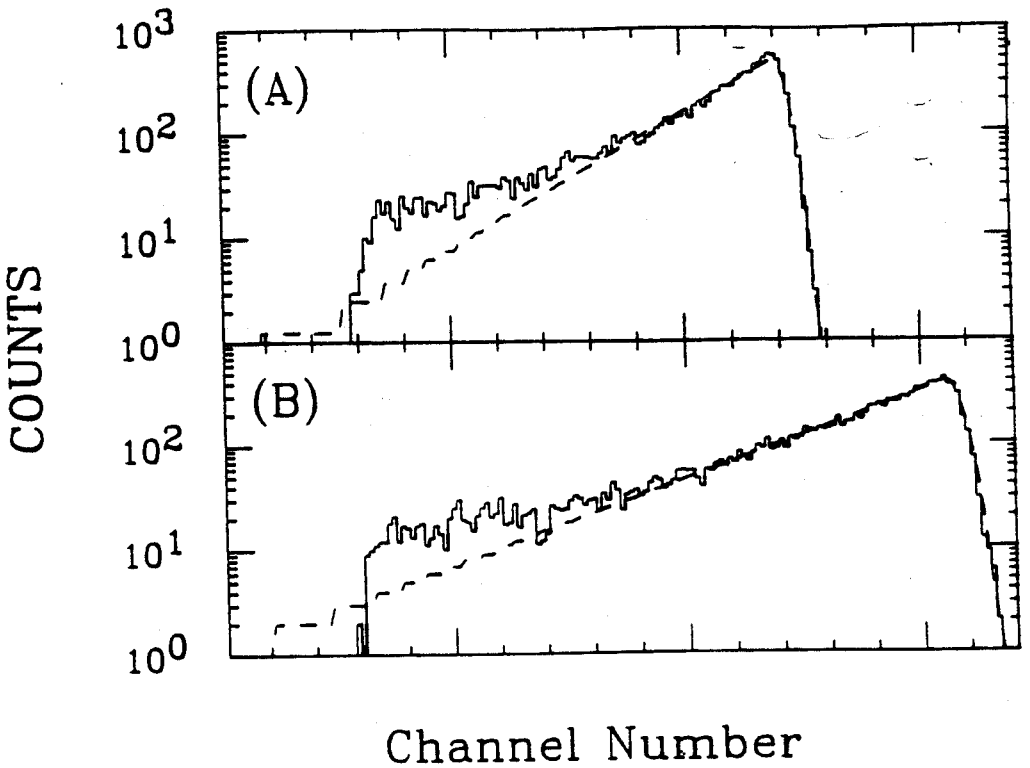

Figure 2.4: The response functions for a 7.6 cm x 7.6 cm BGO detector for incident gamma rays at 17.2 and 22.5 MeV [Hanold 88].

Speidel [Karle 88] report energy resolution of 9.1% FWHM and 6.3% FWHM for 662 keV and 1332 keV gamma rays, respectively. The presence of two components in the scintillation light output gives BaF_2 the advantage that charged particle events can be distinguished from gamma ray events [Wisshak 84,Agodi 88,Murakami 86,Kubota 86]. BaF_2 has an index of refraction of 1.5, it is not hygroscopic, and it displays a relative insensitivity to radiation damage [Majewski 85,Murashita 86]. Since the detection of photons in heavy-ion collisions is made difficult due to the large background of charged particles and neutrons, the use of BaF_2 with its excellent timing resolution and pulse shape information make it the superior choice for this type of measurement. A typical spectrum which shows the separation of particle types by plotting the fast component versus the total light output for gamma rays, protons, deuterons and alpha particles is shown in Figure 2.5. The combination of all of these properties has lead to proposals for large detectors which consist of an array of many BaF_2 crystal elements or to single crystals with volumes approaching several liters (see for example [GSI 87]).

F Lead Glass Detector

One other type of shower detector commonly used in high energy physics experiments is the lead glass detector. It has been used by two groups [Grosse 86] and [Alamanos 86] to measure high energy gamma rays in nucleus-nucleus collisions at intermediate energies. The lead glass detector converts the incident photon into an e^+e^- pair either in the active volume of the detector or in an external converter. As the e^+e^- pairs traverse the detector, they emit photons by the Čerenkov mechanism. This is the well know emission of radiation observed when the velocity of a charged particle in a medium exceeds the speed of light in that medium [Jackson 75a]. The total Čerenkov light output from the many e^+e^- pairs produced is collected by a photomultiplier tube and the sum of all the photoelectrons is proportional to the energy of the incident

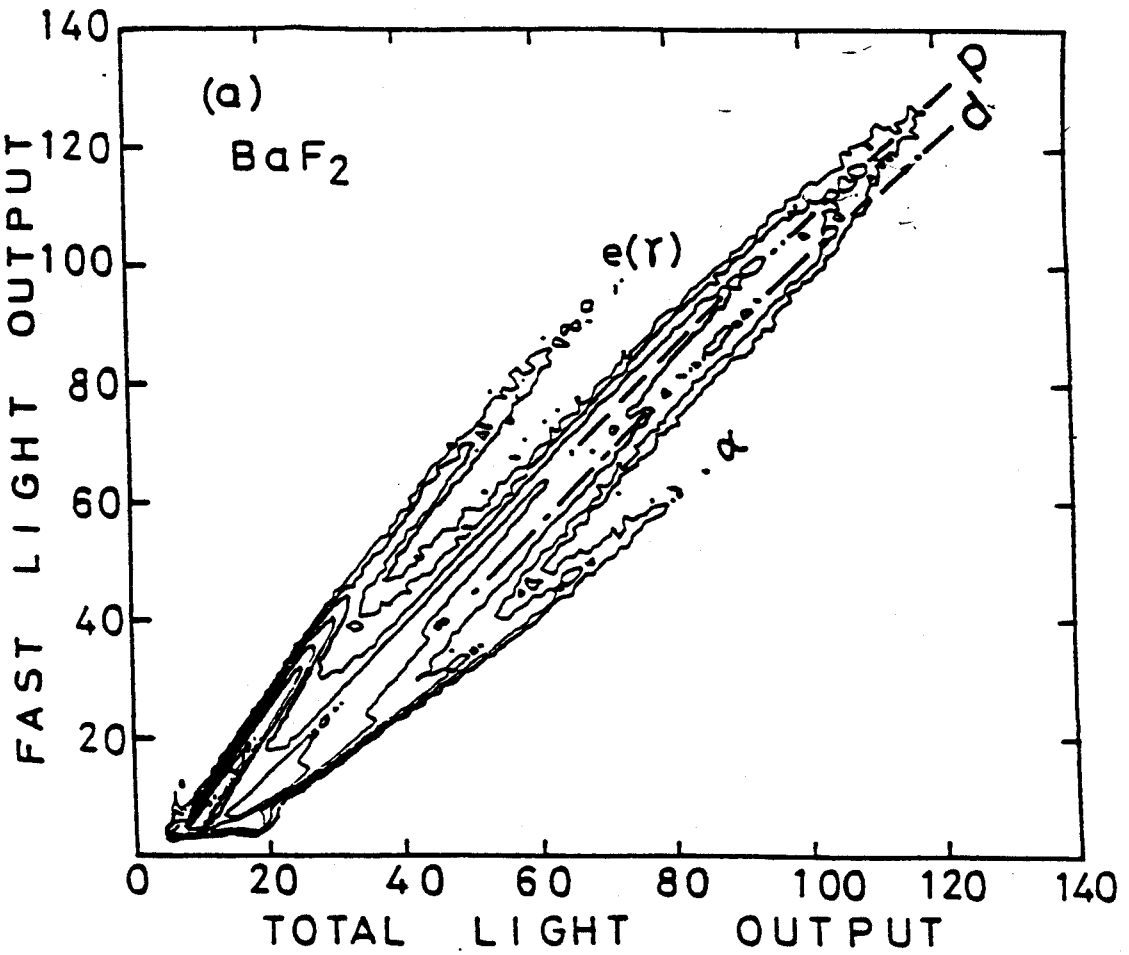

Figure 2.5: Two dimensional contour plot of the fast component versus the total light from a BaF_2 crystal [Kubota 89].

gamma ray. This is a major difference between lead glass detectors and the other detectors discussed previously which use the intrinsic scintillation light. Since these detectors use the Čerenkov mechanism in the active volume, the lead glass detectors exhibit a low sensitivity to neutrons and low energy charged particles.

The major drawback for the use of lead glass detector is the relatively poor energy resolution for photons below 100 MeV, when compared to crystal scintillators such as NaI(Tl) or BaF_2. There is another problem with the response of lead glass detectors to gamma rays with energies below 100 MeV and it is that the response function has a pronounced asymmetrical tail towards higher energies. This can cause serious problems in extracting both the slope parameter and yield of steeply falling exponential spectra. This was demonstrated in a measurement by Hermann *et al.* which is a direct comparison between the response of a single block lead glass detector and a BaF_2 crystal to monochromatic photons at the Mainz tagged photon facility [Hermann 86]. The response function of a lead glass detector at various incident tagged photon energies is shown in Figure 2.6. The energy resolution defined by FWHM/E_γ for the lead glass detector was found to be 13.2% /$\sqrt{E_\gamma}$ (E_γ is in GeV), and this is poor when compared to BaF_2.

G The MSU Plastic Čerenkov Detector

Another detector which makes use of the Čerenkov effect in the detector medium is the wavelength shifted plastic stack developed by the research group at Michigan State University [Stevenson 86,Lampis 88,Tam 88,Tam 89a,Clayton 89]. In the MSU Čerenkov detector a high energy photon is converted into an electron positron pair in an active BaF_2 converter placed in front of the plastic Čerenkov stack. Due to the low atomic number of the plastic (Lucite with a wavelength shifter), instead of an electromagnetic shower formation, the electron and positron lose their energy by a radiative loss mechanism.

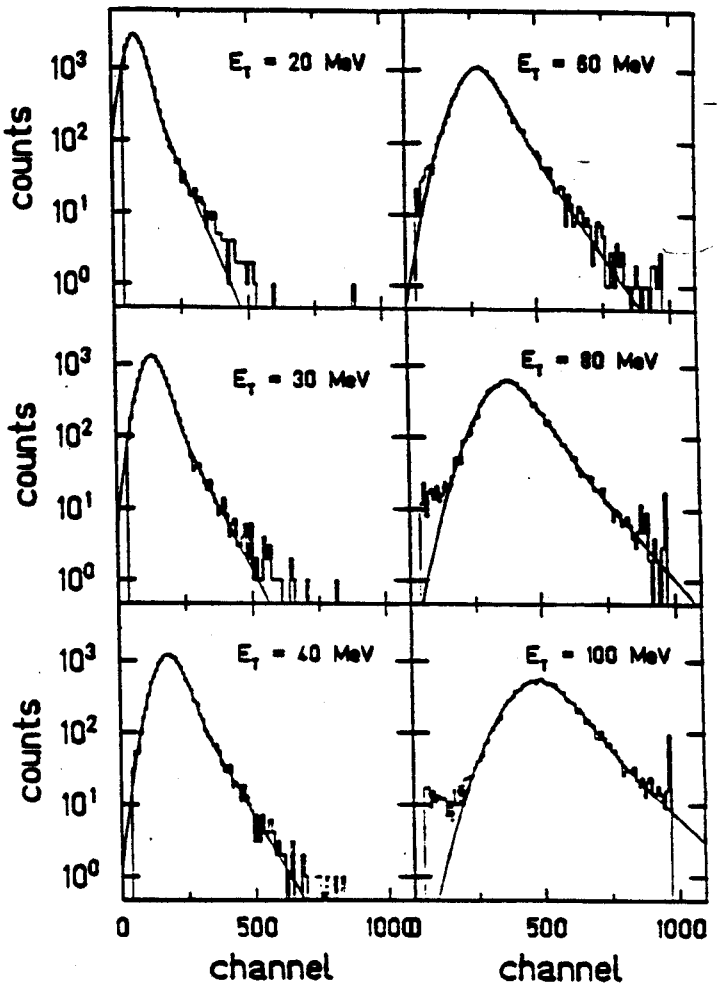

Figure 2.6: The response functions for lead glass detectors for incident gamma rays from 20 to 100 MeV [Hermann 86].

As the e^+e^- pair propagate through the plastic stack, they emit Čerenkov light. A wavelength shifter has been added to the plastic to absorb the focused Čerenkov radiation and re-emit the light isotropically. The waveshifter is needed not only to remove the directionality of the radiation but to also change the wavelength of Čerenkov photons from the UV to the blue region of the visible light spectrum where photomultiplier tubes are most sensitive, typically 400-450 nm. In this wavelength range the wave-shifted light is not attenuated by the lucite, therefore, large pieces of plastic can be constructed. The total energy of the incident photon is given by a position weighted sum of the light output from each element in the detector stack plus the energy lost in the converter. A schematic of the MSU plastic Čerenkov detector is shown in Figure 2.7.

As in the case with the lead glass detector, the Čerenkov detector has the advantage that it is insensitive to neutrons and low energy charged particles. A proton would have to have an incident energy of 320 MeV to leave the equivalent Čerenkov photon yield as a 175 keV electron. Another advantage of the Čerenkov detector is that the output signal is fast and reasonable timing can be done with this type of detector (typically 1ns FWHM). Finally, the detectors can be built to very large volumes and would seem to be very cost effective, \$ 0.02/cm^3 for the plastic detector as opposed to \$ 7.00/cm^3 for an inorganic scintillator such as BGO or BaF_2 . However, when the cost of each detector is compared in a more meaningful unit namely cost per cubic radiation length, the scale shifts to \$ 1280.00/L^3_{rad} for plastic and \$ 60.30/L^3_{rad} for BaF_2 . The most significant problem for this type of detector is its poor energy resolution compared with BaF_2. The MSU plastic detector is further handicapped by the complexity required for experimental set up and data analysis. The energy resolution for the MSU plastic Čerenkov detector is shown in Figure 2.8 along with that of the NaI(Tl) + BaF_2 converter telescope used by [Bertholet 87]. It can be seen

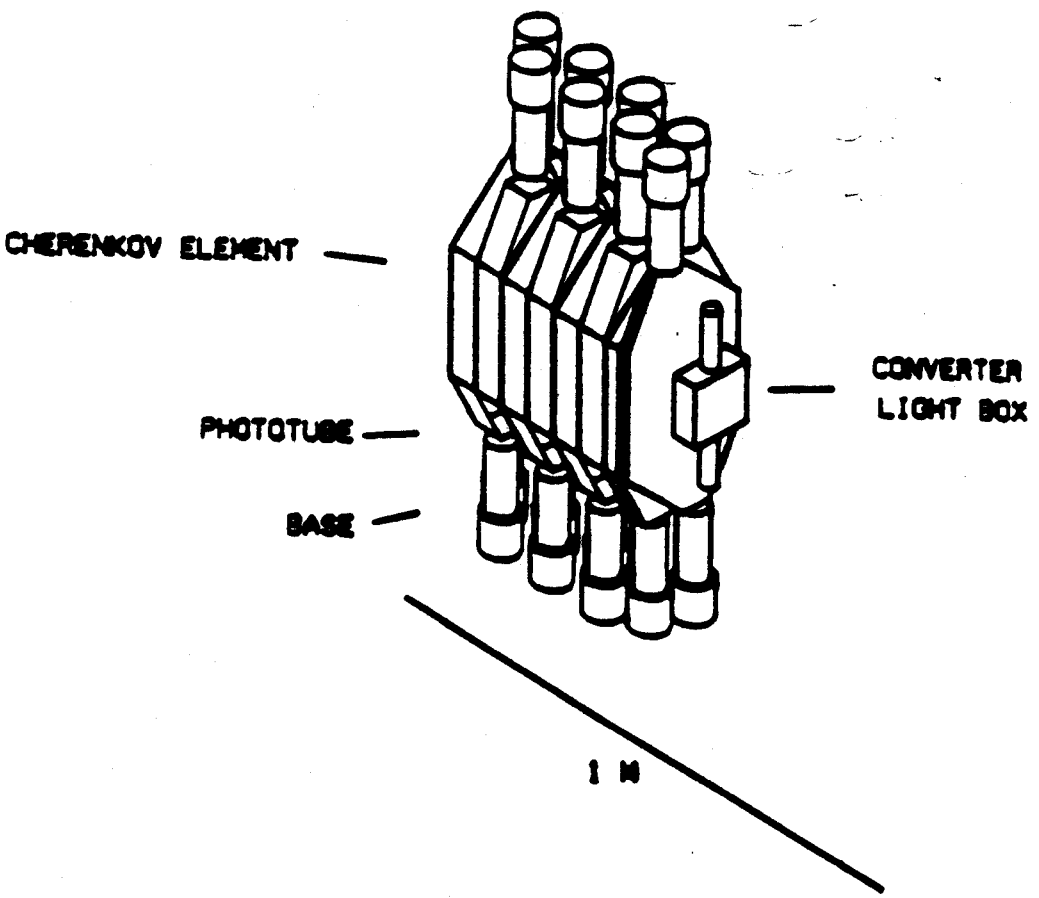

Figure 2.7: A schematic picture of the MSU plastic Čerenkov telescope.

that the response of the Čerenkov detector is not as good as the NaI(Tl) telescope with the difference the greatest at higher energies.

IV Summary

There have been several solutions to the problem of detection of high energy photons in nucleus-nucleus collisions. The majority of these detectors have been calorimeters made from an inorganic scintillator. This was done to take advantage of the good energy resolution and simplicity in use of this type of detector system. With the ability of crystal manufacturers to grow large volume BaF_2 crystals it has become the scintillator of choice for use in these gamma ray measurements. It has the energy resolution necessary for high energy gamma ray detection and its timing characteristics permit rejection of the background neutrons and charged particles that are present in these measurements. The poor energy resolution of the Čerenkov type detectors outweigh the advantage of their insensitivity to neutrons and charged particles that these detectors possess.

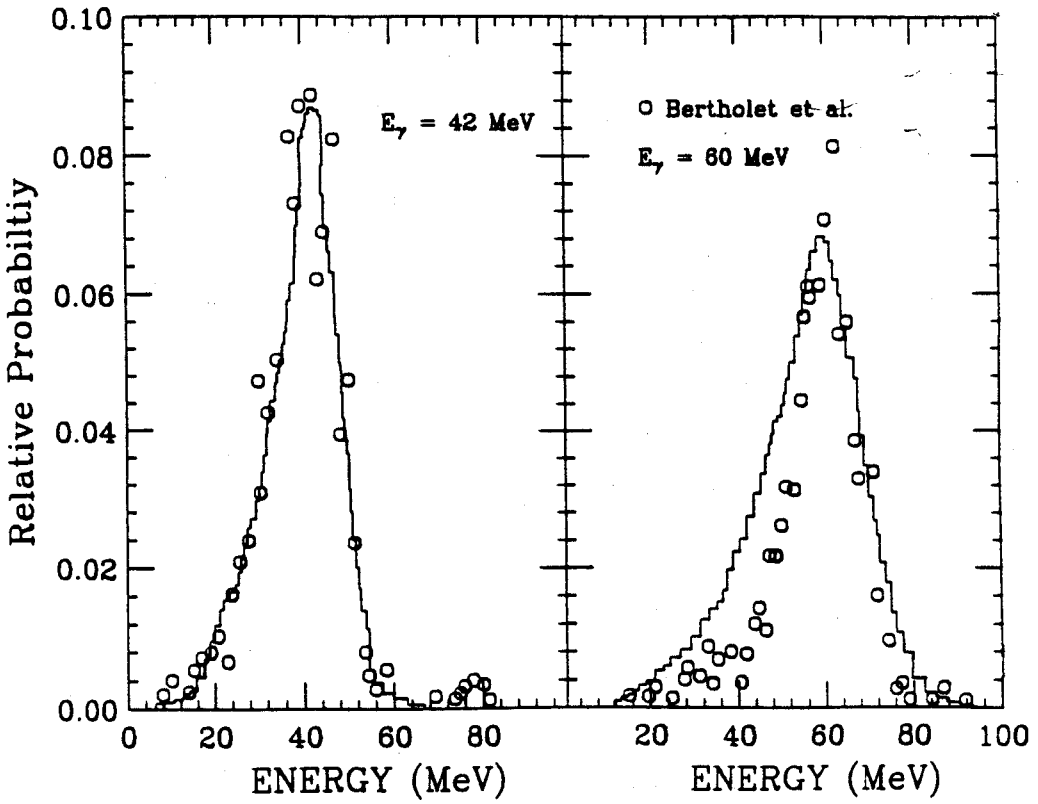

Figure 2.8: Response function for the MSU Čerenkov detector compared to the response function for the Grenoble NaI(Tl) telescope at incident energies of 42 (a) and 60 (b) MeV, respectively [Bertholet 87]. The histogram is the MSU detector and the circles are the NaI(Tl) + BaF_2 telescope.

Chapter 3

Design and Calibration of the BaF_2 Detector

I Introduction

As was discussed in Chapter 2, the demands placed on the detection system for high energy gamma rays lead to several solutions. The detectors that use large volume BaF_2 crystals have had the most success in the identification of high energy gamma rays. Briefly reiterating, some of most important facts regarding BaF_2 are:

1. BaF_2 has excellent time resolution, approaching 80 ps (FWHM) for small crystals [Laval 83] and 400 ps FWHM for large crystals [Wisshak 84].
2. The relatively high density of the scintillator (4.89 g/cm^3) and the high atomic number of Ba (56) give BaF_2 good detection efficiency for gamma rays (radiation length = 2.05 cm). Karle, Knoop and Speidel [Karle 88] report energy resolution of 9.1% FWHM and 6.3% FWHM for 662 keV and 1332 keV gamma rays, respectively.
3. The presence of two components in the scintillation light output give BaF_2 the advantage that charged particle events can be distinguished from gamma ray events [Wisshak 84,Agodi 88,Murakami 86,Kubota 86].

The research group at MSU studying high energy gamma ray production decided that the next generation detector used for this research would be a large volume BaF_2 crystal. This detector was to be the replacement for the large plastic Čerenkov detector used in previous measurements. The design and calibration of the large BaF_2 crystal will be the topic covered in this chapter. In this chapter it will be shown that realistic Monte-Carlo simulations of the electromagnetic shower can reproduce the measured response to tagged photons. In addition, an analytical energy dependent parameterization of the resulting line shape is given for photon energies in the range from 75-200 MeV. A method for establishing a transferable energy calibration with cosmic ray muons instead of monoenergetic photons is also described.

II Design of the BaF_2 Detector

The choice for the size of the BaF_2 detector was determined by two factors. The first is the energy resolution required for these measurements and the second was the ability of the manufacturer to supply the crystals. Since the energy resolution is a strong function of the geometry, it was necessary that the crystal be as large as possible. However, the most severe constraint was placed by the ability of the manufacturer to grow such large volume crystals. The maximum diameter available at the time was 15 cm, and the maximum length was roughly 13 cm. This was mainly due to the size of the furnace in which the crystals were grown. However, the crystals of this size did not have good energy resolution, and this was due, in part, to contamination of lead and other impurities in the boule. It was decided that the total detector volume would be 3.0 l and would be comprised of two right cylinders of 1.5 l in volume each, and this would avoid poor energy resolution associated with crystals of a much larger size. The specification on energy resolution was that it must be better than 13% FWHM at 662 keV. This is the energy of the gamma from the standard gamma

ray source ^{137}Cs. One other factor which can cause problems is the background due to radium contamination. Since the chemical properties of barium and radium are similar it is very difficult to completely remove this background. Background from naturally occurring radium was specified and the acceptable level at was set at 5.0 nCi/l.

The mechanical design for the support and protective housing for the crystal is shown in Figure 3.1. It can be seen form Figure 3.1 that the crystals are supported in an aluminum housing thus protecting them from damage due to stress or shock. The compression spring at the end of the crystal serves to keep the optical joint intact. The cables for the input high voltage and output signals are at the base plate flange and the aft end of the detector.

Inside the housing the BaF_2 detector consists of two right cylinders [Englehard Corp. 88] with a diameter of 12.7 cm (2.9 ρ_M -the Molière radius) and a length of 11.45 cm. The total crystal length is 22.9 cm which is approximately 11.2 radiation lengths deep. The two crystals were optically coupled together with 10^5 centipoise silicon oil [Mc Ghan] and then wrapped with Teflon tape (0.5 mm total thickness), aluminum foil (0.2 mm) and finally black electrical tape. The Teflon tape was used since polytetrafluoroethylene compounds (PTFE) exhibit excellent reflectivity in the ultraviolet region [Weidner 81]. Three 5.08 cm diameter Hamamatsu R2256 quartz window photomultiplier tubes were coupled to one end of the cylinder with an RTV silicon rubber compound which has excellent transmission of UV light [General Electric Corp]. The emission spectra of BaF_2 and the transmission properties are displayed in Figure 3.2. The use of quartz windowed photomultiplier tubes allows complete coverage of the emission spectrum of BaF_2. The transmission spectra for a quartz windowed photomultiplier is displayed in Figure 3.3

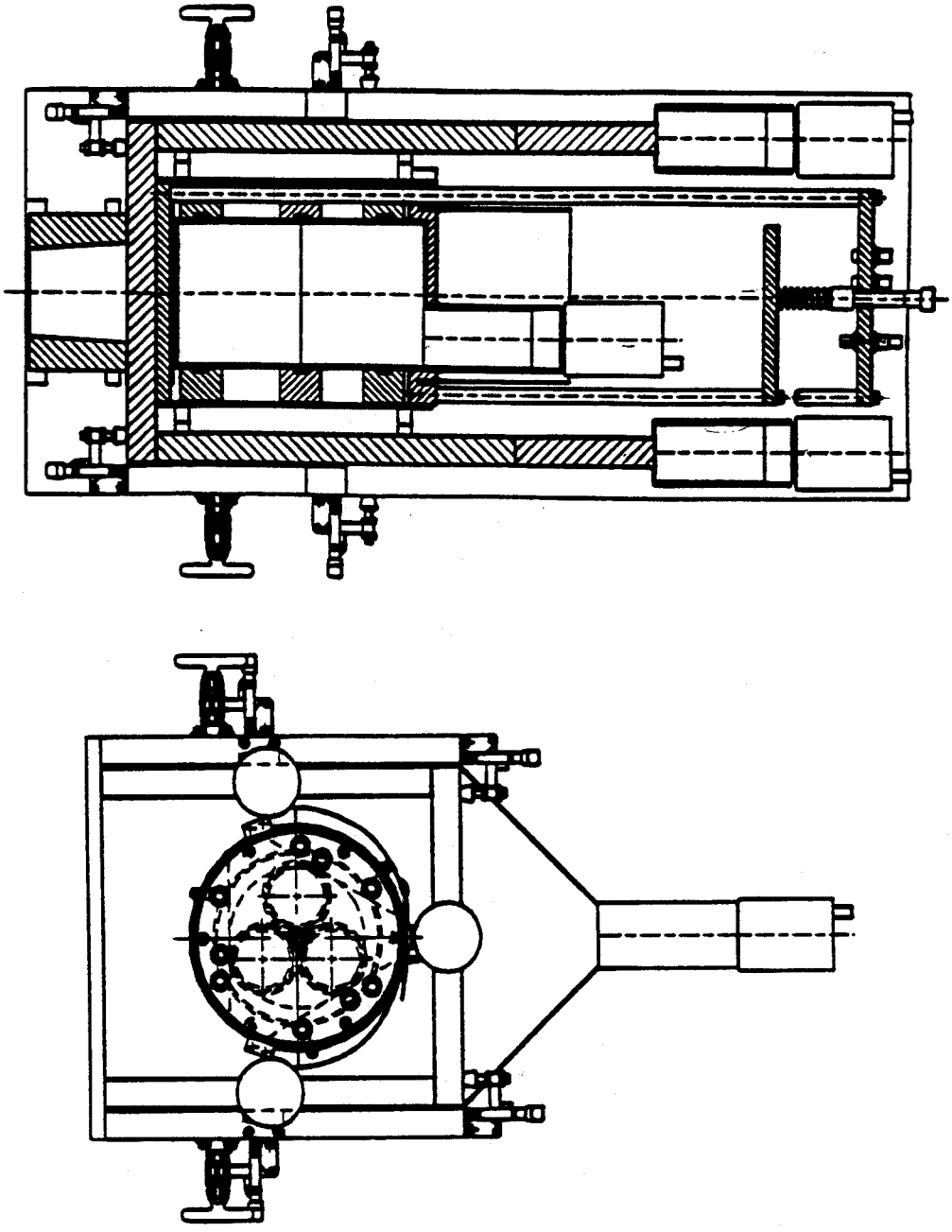

Figure 3.1: A sketch of the mechanical supports and housing for the BaF_2 crystal.

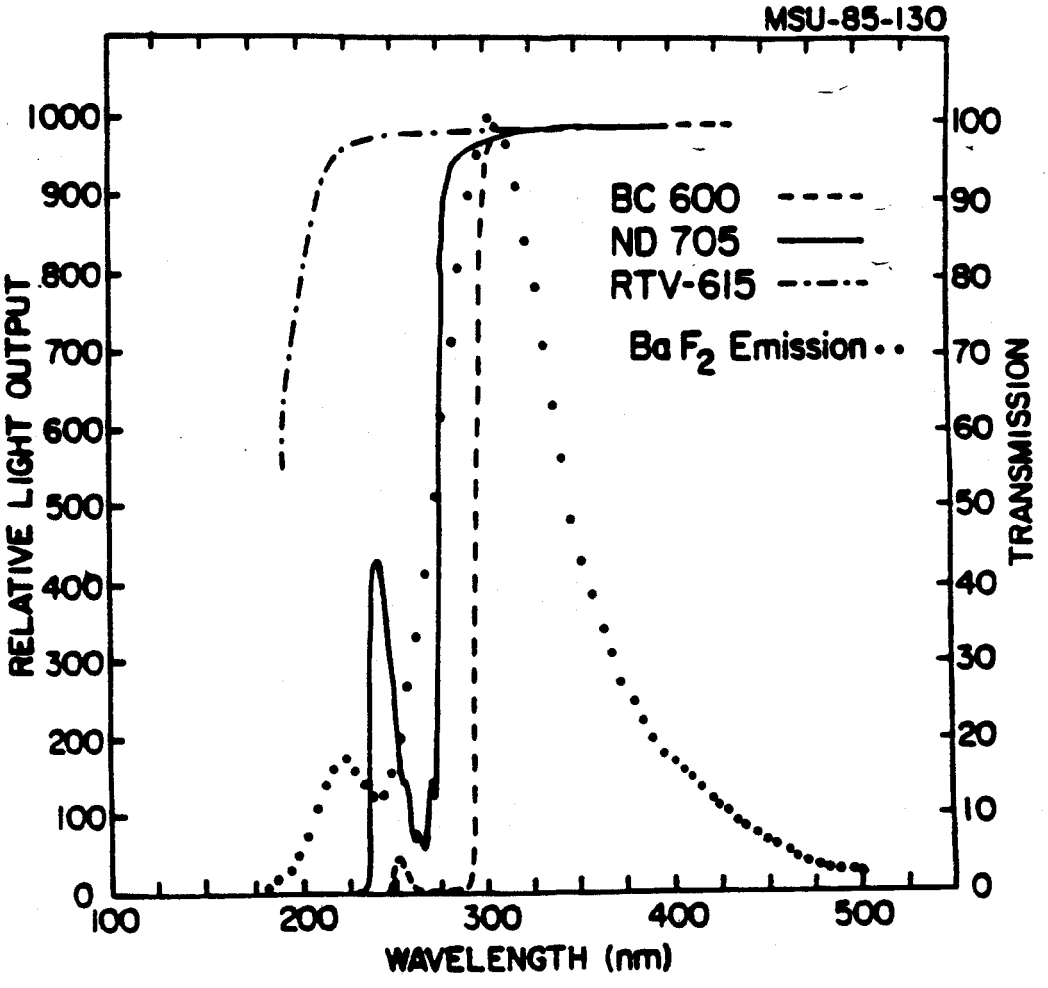

Figure 3.2: The emission spectra for the scintillator BaF_2 and the spectral transmission for GE RTV 615 [Yurkon 85].

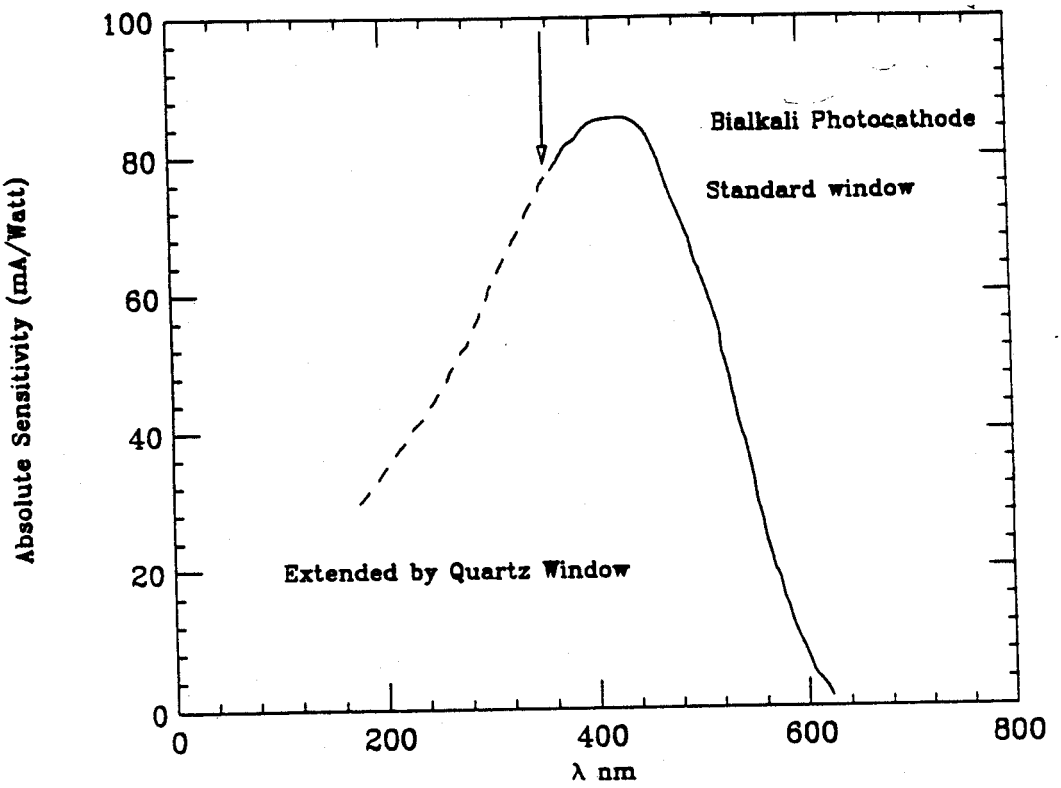

Figure 3.3: The spectral transmission for a Hamamatsu R2256 photomultiplier tube.

III Experiment

The results described in this thesis were obtained for a large volume BaF_2 crystal which was exposed to monochromatic photon beams in the energy range from 75 to 200 MeV at the tagged photon facility of the Saskatchewan Accelerator Laboratory at the University of Saskatchewan. The tagged photons were produced by bremsstrahlung radiation in a thin foil by an incident electron beam. The production rate of bremsstrahlung photons depends approximately on the photon energy, E_γ, as $1/E_\gamma$. In this measurement the electron beam had a kinetic energy of 264.5 MeV and was incident on an aluminum foil. The energy of the electron after scattering was measured in a magnetic spectrometer which, combined with the knowledge of the incident electron energy, defined the energy of the bremsstrahlung photon. The spectrometer detected electrons above 66 MeV in a focal plane detector consisting of 16 overlapping plastic scintillator paddles that tagged photons from 76.54 MeV to 143.13 MeV and from 162.33 MeV to 199.23 MeV. The energy range at each spectrometer setting was further subdivided into 16 almost equal and slightly overlapping bins, reflecting the structure of the focal plane detector. The experimental vault set-up is shown in Figure 3.4. The central photon energy and the energy range covered for each tagger paddle is exhibited in Table 3.1 for the low energy setting and in Table 3.2 for the high energy setting.

The detector was placed in the photon beam 5.48 m from the bremsstrahlung radiator. The size of the photon beam was reduced by a 20 mm diameter lead collimator placed 1.92 m from the radiator. This gave rise to a spot size of 5.7 cm at the face of the crystal. An 11.4 cm deep 95% tungsten collimator with an acceptance diameter of 7.8 cm was placed in front of the crystal to ensure that the detector was centrally illuminated by the tagged photons. The tungsten collimator

Table 3.1: Tagged photon energies for the high field setting used at the Saskatchewan Accelerator Laboratory. The incident electron beam momentum was 265 MeV/c and the magnetic field setting was 0.876 T.

Central Tagger Momentum P_0 = 140.15					
Paddle Number	Position (cm)	Central Momentum P/P_0 %	Central Momentum MeV/c	Photon Energy MeV	Photon Energy MeV
1	-22.41	-13.77	123.70	141.30	3.65
2	-18.07	-13.77	127.39	137.61	3.72
3	-13.73	-8.59	131.14	133.86	3.79
4	-9.39	-5.92	134.96	130.04	3.86
5	-5.05	-3.21	138.85	126.15	3.92
6	-0.70	-0.45	142.81	122.19	3.99
7	3.64	2.35	146.84	118.16	4.06
8	7.98	5.21	150.93	114.07	4.13
9	12.32	8.11	155.09	109.91	4.20
10	16.66	11.06	159.32	105.68	4.26
11	21.00	14.05	163.62	101.38	4.33
12	25.34	17.10	167.99	97.01	4.40
13	29.68	20.19	172.42	92.52	4.47
14	34.02	23.33	176.92	88.08	4.54
15	38.37	26.51	181.49	83.51	4.60
16	42.71	29.75	186.13	78.87	4.67

Table 3.2: Tagged photon energies for the low field setting used at the Saskatchewan Accelerator Laboratory. The incident electron beam momentum was 265 MeV/c and the magnetic field setting was 0.502 T.

Central Tagger Momentum P_0 = 80.30					
Paddle Number	Position (cm)	Central Momentum P/P_0 %	Central Momentum MeV/c	Photon Energy MeV	Photon Energy MeV
1	-31.09	-18.77	66.77	198.23	2.01
2	-26.75	-16.29	68.80	196.20	2.05
3	-22.41	-13.77	70.87	194.12	2.09
4	-18.07	-11.20	72.99	192.01	2.13
5	-13.73	-8.59	75.14	189.86	2.17
6	-9.39	-5.92	77.33	187.67	2.21
7	-5.05	-3.21	79.56	185.44	2.25
8	-0.70	-0.45	81.82	183.18	2.29
9	3.64	2.35	84.13	180.87	2.33
10	7.98	5.21	86.48	178.52	2.37
11	12.32	8.11	88.86	176.14	2.40
12	16.66	11.06	91.28	173.71	2.44
13	21.00	14.05	93.75	171.25	2.48
14	25.34	17.10	96.25	168.75	2.52
15	29.68	20.19	98.79	166.21	2.56
16	34.02	23.33	101.37	163.63	2.60

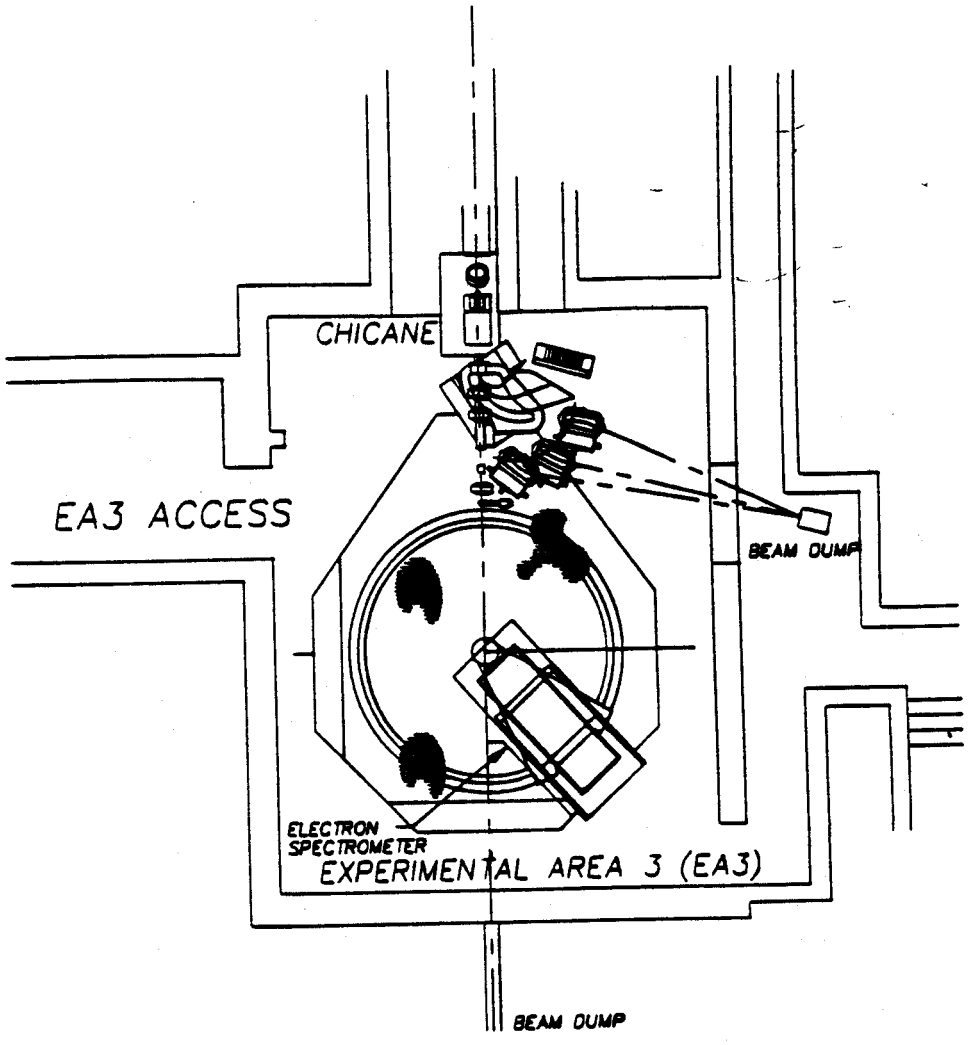

Figure 3.4: Diagram for the experimental vault set-up at the Saskatchewan Accelerator Laboratory.

was used in studies of high energy bremsstrahlung gamma rays (ie., [Clayton 90]), and its use in the calibration simulates experimental running conditions. The crystal was also surrounded by a 2.54 cm thick plastic scintillator anticoincidence shield. The anticoincidence shield was used to reject cosmic rays as well as to check on the extent of shower leakage from the crystal. A threshold energy of 2.5 MeV was placed on the constant fraction discriminator (CFD) for the anticoincidence shields. This is approximately one half of the energy deposition for a minimum ionizing particle in the plastic scintillator. Several runs were also made in which a 40 cm polyethylene absorber bar was placed between the detector and the photon source. This was done to estimate the effect of the polyethylene absorber bar on the attenuation of gamma rays and to investigate its effect on the response function. This was necessary since the absorber bar is used to attenuate fast light particles coming from the target in heavy ion experiments.

During the calibration, the signals from each photomultiplier tube were split into three equal parts. One part went to a constant fraction discriminator (CFD) which generated a time signal for each photomultiplier tube. The second part was fed to a Linear Fan-In module which summed the three analog signals and its output was sent to a CFD to generate the event trigger. The final portion of the signal was reduced by a factor of ten and was sent to a charge-sensitive analog-to-digital converter [Lecroy] (QDC) which was operated with a gate width of approximately 1.7μs. The electronics diagram for the calibration is shown in Figure 3.5.

IV Monte-Carlo Simulations (EGS4) and Comparison of the Line Shapes

The Monte-Carlo simulations of the resulting electromagnetic shower were performed with EGS4 [SLAC 85] (Electron Gamma Shower Code). The photons and electrons in

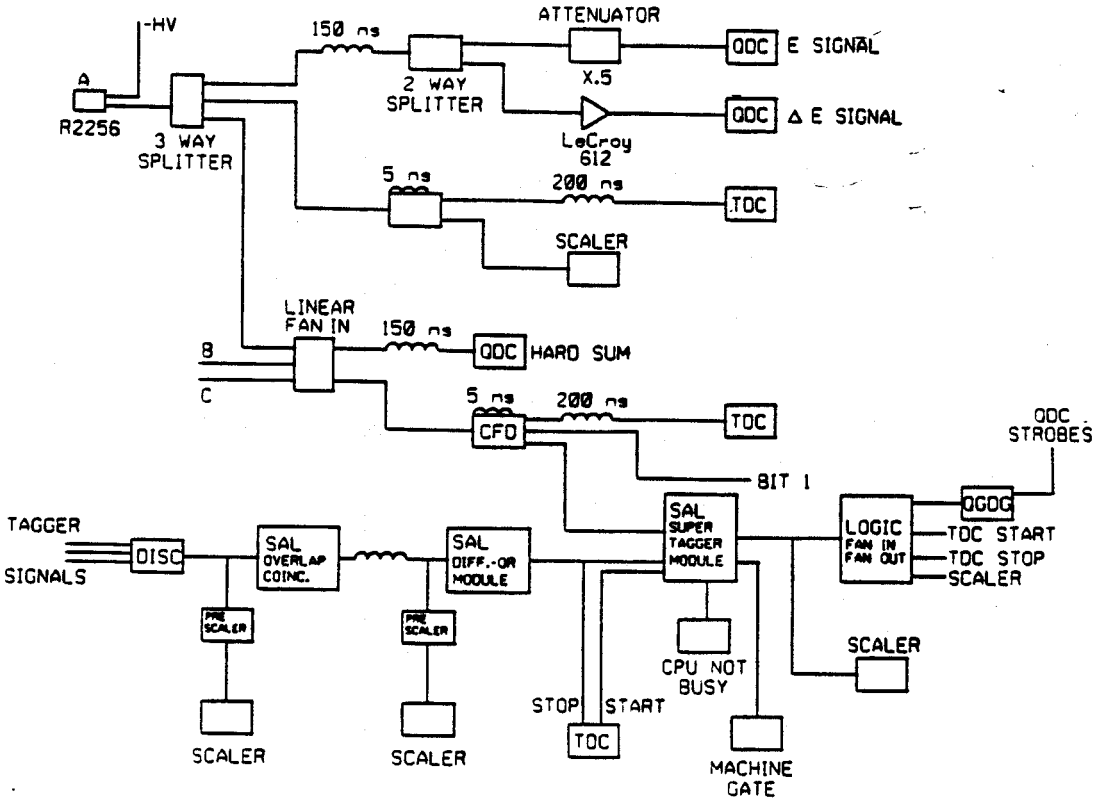

Figure 3.5: Electronics diagram for the experimental tagged photon experiment at the Saskatchewan Accelerator Laboratory.

the electromagnetic shower were followed down to 100 keV, once reaching this low energy cutoff the particles were considered to be stopped and to have deposited all of their kinetic energy in the active volume. The geometry of the detectors, the finite energy bin size of the tagger scintillator paddles and the photon spot size were accounted for in the simulations. The anticoincidence shields were also included in the Monte-Carlo simulation. As in the actual experiments, an energy cut of 2.5 MeV in the plastic anticoincidence shields was used in the simulation to reject events that showed significant lateral leakage of the electromagnetic shower or events that converted into e^+ e^- pairs before entering the BaF_2 crystal. The front anticoincidence shield is very important in rejecting these conversion events when the polyethylene absorber is used. The lateral leakage of the shower is roughly a constant 7% of the incident photon energy. The anticoincidence shields show very little energy deposition above the 2.5 MeV threshold which indicates that high energy electrons and positrons are not escaping the active volume of the detector. The longitudinal loss in the electromagnetic shower increases from 4% of the incident photon energy at 75 MeV to 7% at 200 MeV, and it is these losses that are the most detrimental to the energy resolution [Amaldi 87]. Figure 3.6 shows a comparison of the EGS4 simulation to the measured tagger data at 99.22 MeV to 103.54 MeV and 181.03 MeV to 184.33 MeV for both configurations. The EGS4 simulations are in good agreement with the measured data, and the effect of the absorber is to extend the low energy tail of the distributions. The dashed curves representing the EGS4 simulations are in such good agreement that for the most part they are obscured by the solid curves representing the measured data.

Since both the simulated and experimental detector response have an asymmetrical shape, a good test would be to compare the first four moments of the measured and calculated distributions respectively. The following quantities have been com-

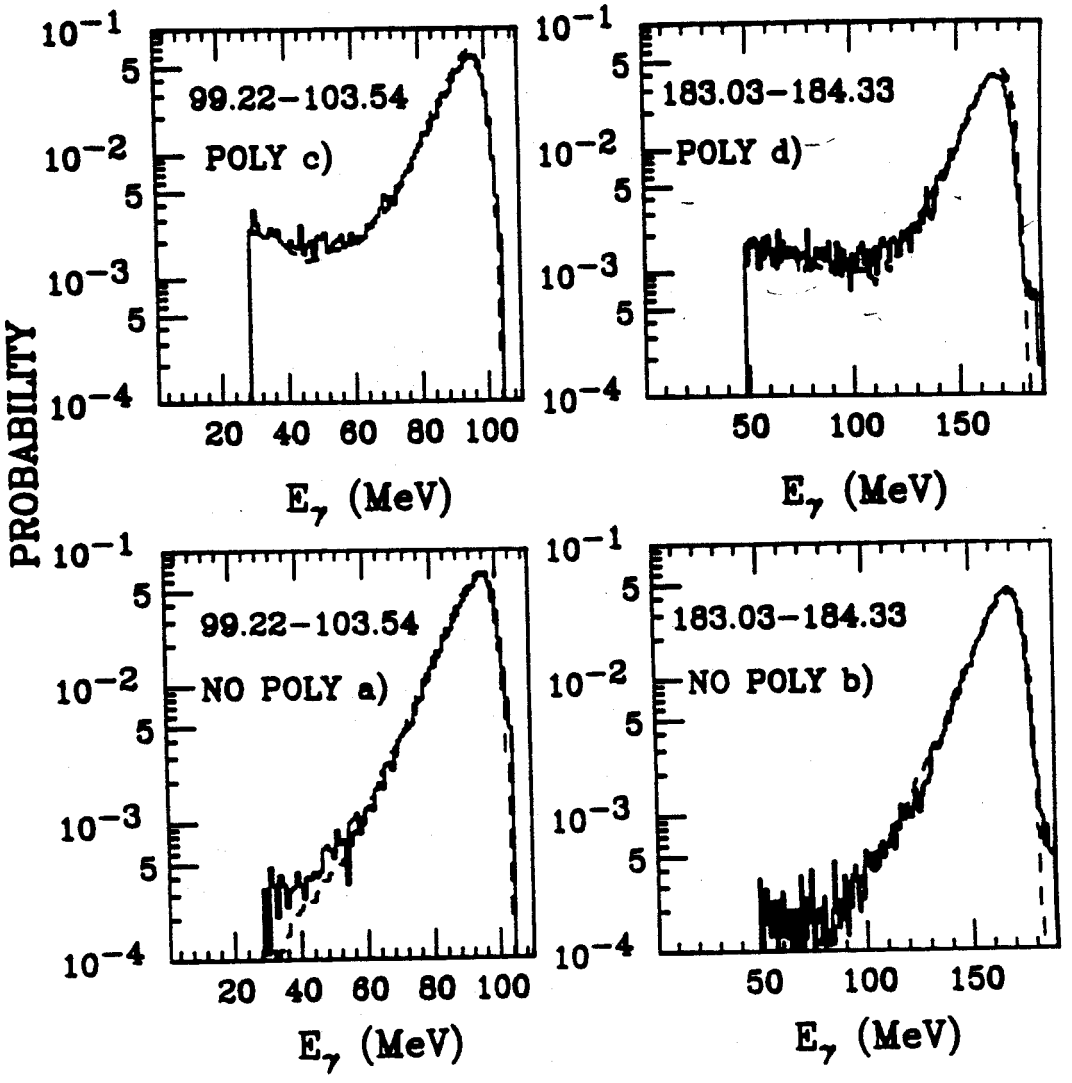

Figure 3.6: A comparison of the measured (solid) and calculated (dash) spectra for tagged photons in the energy range from 99.22 to 103.54 MeV and from 183.03 and 184.33 MeV respectively.

puted for each energy bin and each tagger setting: mean value ⟨E⟩, the standard deviation σ, skewness γ_1, and kurtosis γ_2. The equations for these quantities are:

$$< E >= \frac{\sum N_i \cdot E_i}{\sum N_i} \tag{3.1}$$

$$\sigma = \sqrt{\frac{\sum N_i \cdot (E_i - < E >)^2}{\sum N_i}} \tag{3.2}$$

$$\gamma_1 = \frac{\sum N_i \cdot (E_i - < E >)^3}{\sigma^3 \cdot \sum N_i} \tag{3.3}$$

$$\gamma_2 = \frac{\sum N_i \cdot (E_i - < E >)^4}{\sigma^4 \cdot \sum N_i} - 3 \tag{3.4}$$

where N_i is the number of counts in the energy interval E_i of the measured and calculated spectra. The simulation shows reasonable agreement with the tagger data for all of the calculated moments. Figure 3.7 and Figure 3.8 display the first two moments for the data set with and without the polyethylene absorber. The low energy cutoffs used in calculating all the moments are the same, namely 40% of the most probable energy deposition for the runs with and without the polyethylene absorber bar. As expected the extracted value of the experimental mean energy deposition is not a linear function of increasing energy; this is due to the fact that an increasing portion of the electromagnetic shower is escaping out of the detector.

The differences between the experimental and simulated mean energies are small, (1 ± 2)% as shown in Figure 3.9. Figure 3.7 and Figure 3.8 show the comparison of the standard deviations of measured and simulated spectra, again the agreement is reasonable. The difference between the standard deviations of the two spectra has a mean value of (-1 ± 4)% for the bare crystal and (5 ± 3)% for the crystal plus polyethylene data, and the results are displayed in Figure 3.10. The EGS4

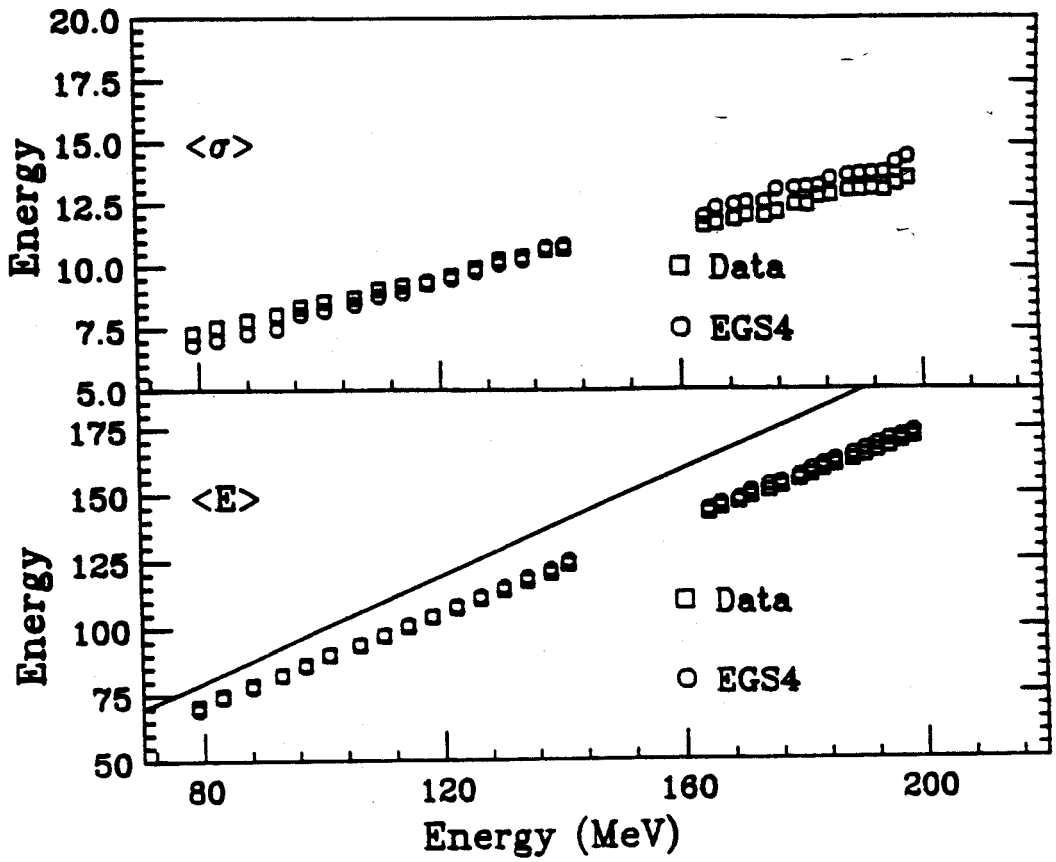

Figure 3.7: A comparison of the mean value ⟨E⟩ and the standard deviation σ for the experimental and EGS4 simulated response functions for tagged photons in the energy range from 75 to 200 MeV for a large volume BaF_2 crystal. The solid curve is the line Y=X and would represent complete containment of the electromagnetic shower.

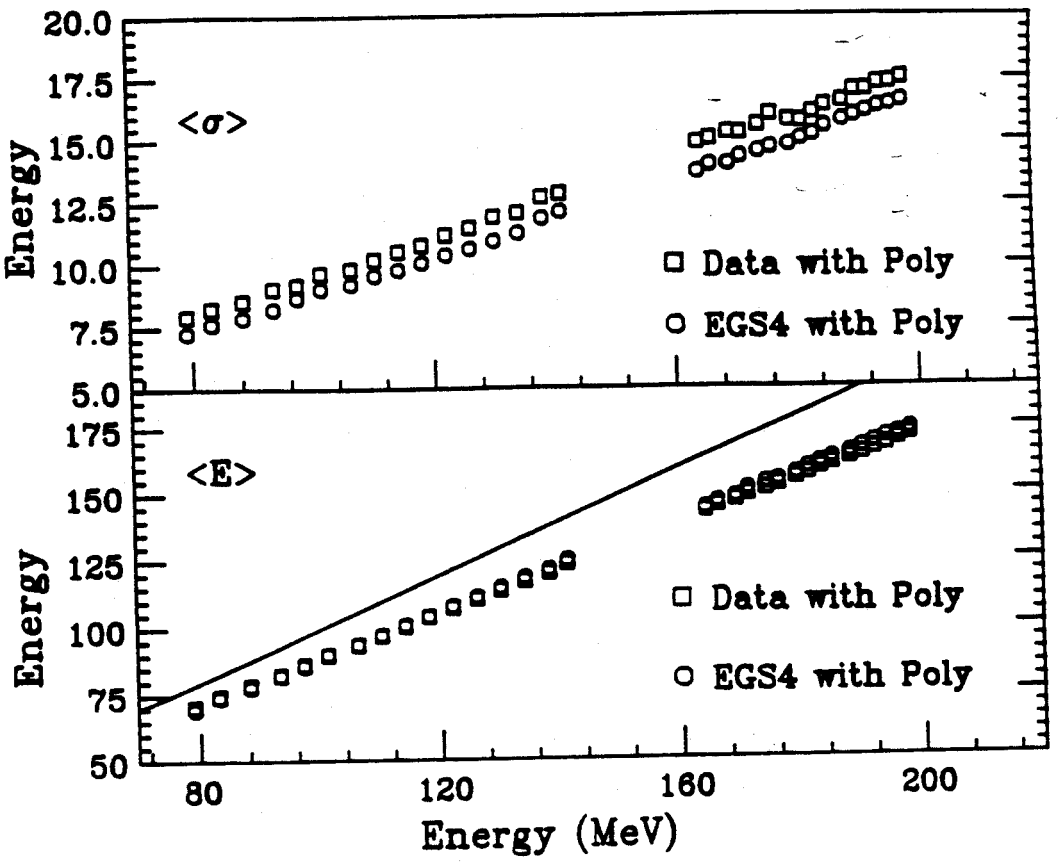

Figure 3.8: A comparison of the mean value ⟨E⟩ and the standard deviation σ for the experimental (squares) and *EGS4* simulated (circles) response functions for tagged photons in the energy range from 75 to 200 MeV for a large volume BaF_2 crystal with a 40 cm polyethylene bar inserted in front of the crystal. The solid curve is the line Y=X and would represent complete containment of the electromagnetic shower.

simulations include the beam spot size, the finite bin width of the tagger focal plane scintillator paddles and fluctuations in the leakage of the electromagnetic shower out of the detector. The differences in the widths of the experimental and calculated simulations may be attributed to:

1. The dependence of the production and the transmission of the scintillation light on location in the BaF_2 crystal.
2. Nonlinearities in the photomultiplier tube or the charge-sensitive analog-to-digital converter.

Effects arising from photoelectron statistics should be negligible in this energy range. The number of photons per MeV of deposited γ radiation in a detector of this volume is quite large. In the literature the following values have been reported for the sum of fast and slow components from BaF_2: 2500-2800 [Zhu 86], 800-1500 [Chang 87], 1430 $\pm$ 70 [Klamra 88]. These values were consistent with the results obtained for this detector which were based on the assumption that the energy resolution at low energies is limited by the photoelectron statistics. The contribution to the experimental FWHM from photoelectron statistics would be 1.0 MeV at 75 MeV and 1.7 MeV at 200 MeV respectively. The EGS4 spectra used in the comparison to the measured data have been convoluted with a Gaussian the width of which has been determined from the resolution at standard gamma ray source energies. The width of the Gaussian used in the convolution is given by:

$$R = 2.35 \cdot \frac{\sigma_{stat}}{E_\gamma} \tag{3.5}$$

where

$$\sigma_{stat} = \sqrt{A \cdot E_\gamma} \tag{3.6}$$

The constant A is determined from the 15% resolution of 662 KeV gamma ray from ^{137}Cs and its value is 0.003 MeV.

In Figure 3.11 and Figure 3.12 the third moment, γ_1, the Skewness, and fourth moment, γ_2, the Kurtosis (or Excess), are displayed for both measured and simulated distributions. The values extracted for the higher moments are in approximate agreement. This reflects the consistency between experimental and Monte-Carlo simulated data.

A Efficiency of the Crystal with Absorber

As was discussed earlier, a 40 cm polyethylene bar was inserted in front of the collimated BaF_2 crystal to observe the efficiency of the crystal with the absorber in place. This is necessary since the polyethylene bar was used to attenuate the flux of light charged particles and fast neutrons produced in the target in heavy-ion collisions. The ratio of detector counts in the peak divided by the number focal plane scintillator paddle counts with and without the polyethylene in place gives a measure of the attenuation coefficients for gamma rays in polyethylene at these incident energies. The attenuation coefficients are displayed in Figure 3.13 and are in good agreement with the values calculated from the EGS4 simulations.

V Energy Calibration

Calibration of photon detectors is a standard problem, and the usual procedure is to place a source of known γ-ray energy in front of the detector and observe the full-energy peak. This procedure is limited to detectors with sufficient volume to completely absorb the incident photon and is useful only when the region of interest is relatively close to the standard source energies. In measurements that require

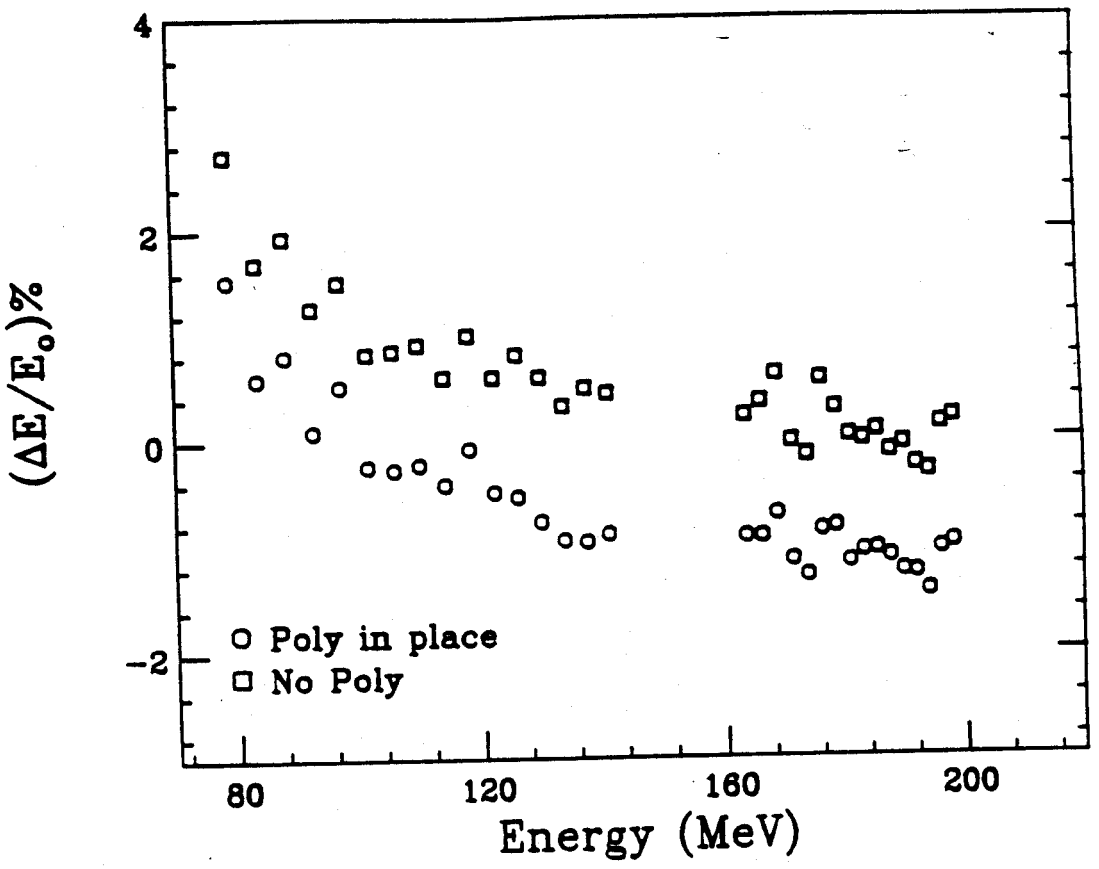

Figure 3.9: The difference between the measured mean value (squares), $\langle E \rangle_{meas}$, and the mean value from the *EGS4* simulations (circles), $\langle E \rangle_{calc}$, for photons in the energy range from 75 to 200 MeV.

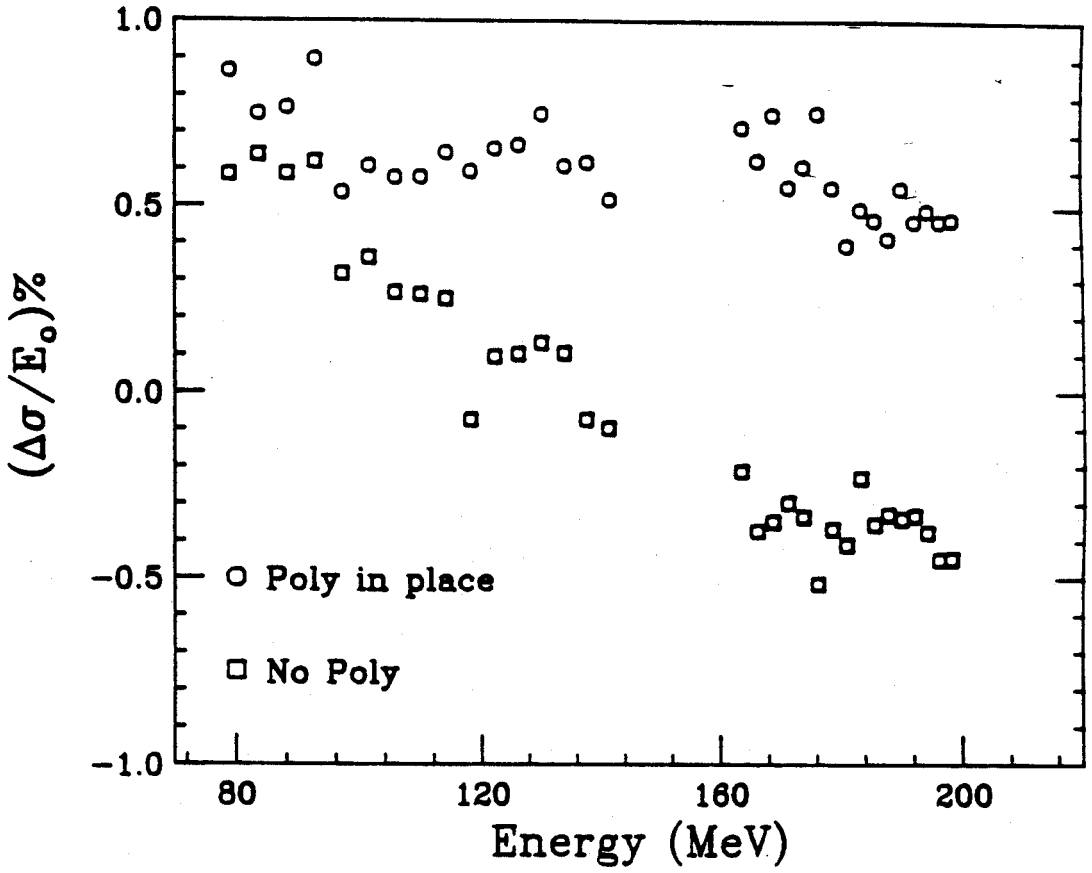

Figure 3.10: The difference between the measured standard deviations (squares), σ_{meas}, and the standard deviations from the *EGS4* simulations (circles), σ_{calc}, for photons in the energy range from 75 to 200 MeV.

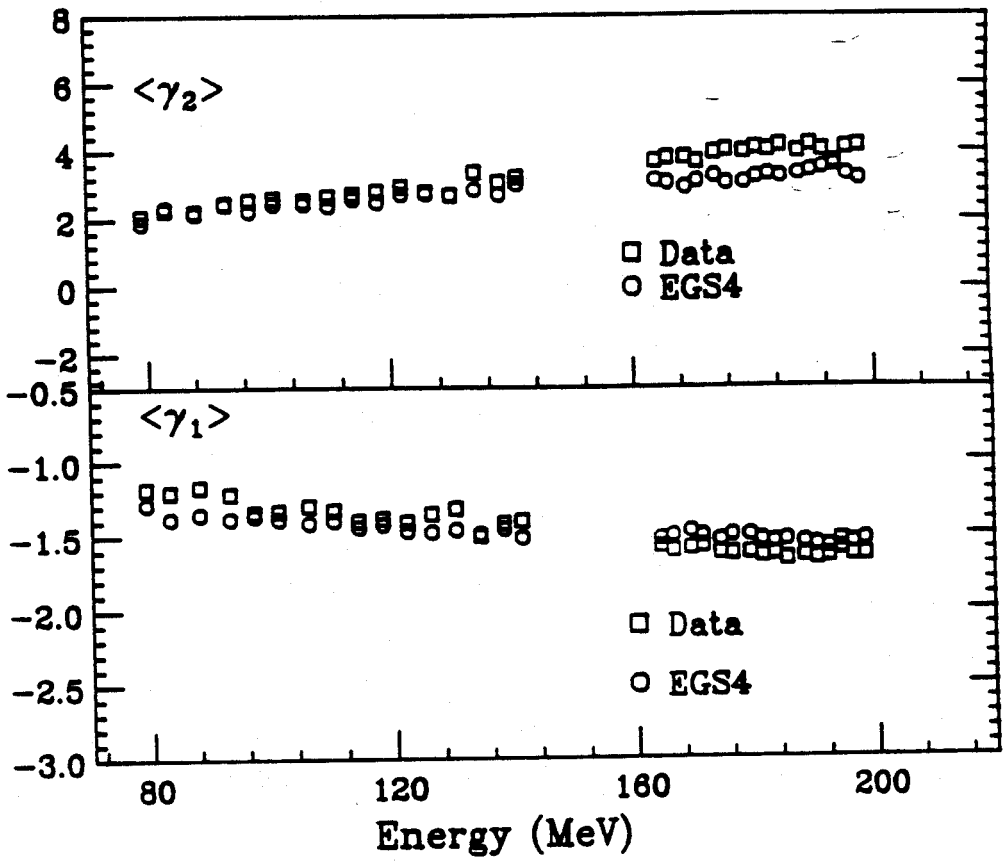

Figure 3.11: A comparison of the third moment, γ_1 Skewness, and the fourth moment, γ_2 Kurtosis or Excess, for the experimental (squares) and *EGS4* simulated distributions (circles) for tagged photons in the energy range from 75 to 200 MeV for a large volume BaF_2 crystal.

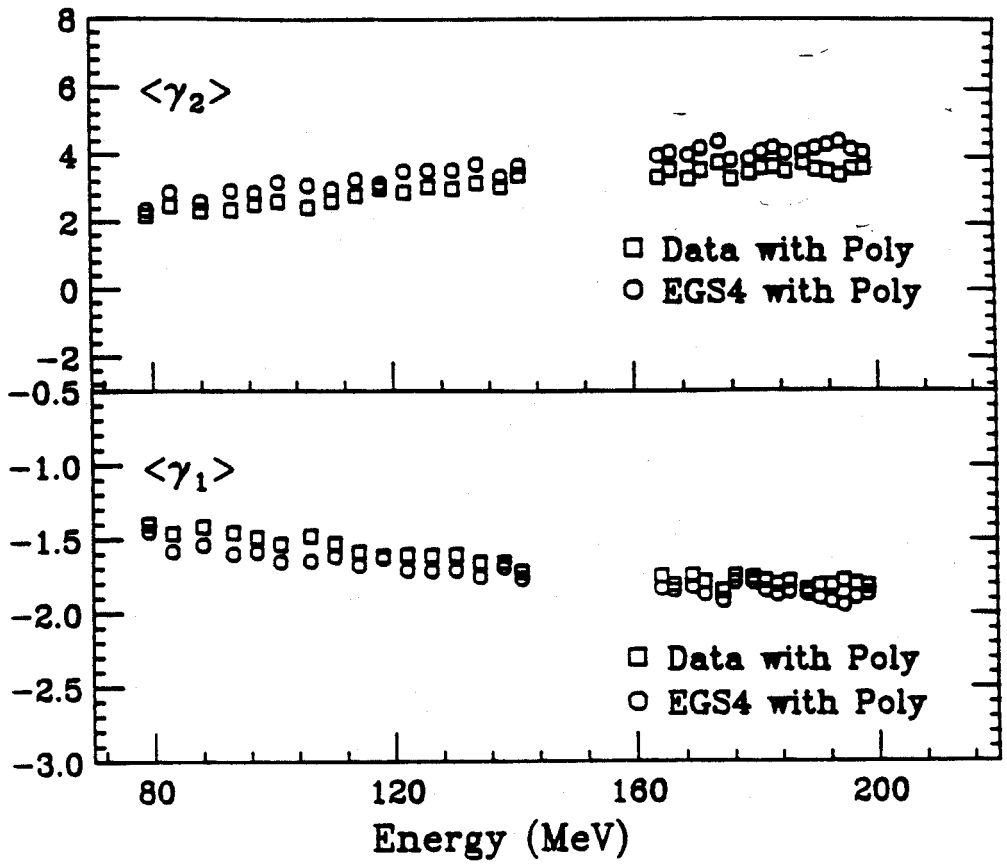

Figure 3.12: A comparison of the third moment, γ_1 Skewness, and the fourth moment, γ_2 Kurtosis or Excess, for the experimental and *EGS4* simulated distributions for tagged photons in the energy range from 75 MeV to 200 MeV for a large volume BaF_2 crystal with a 40 cm polyethylene bar inserted in front of the crystal.

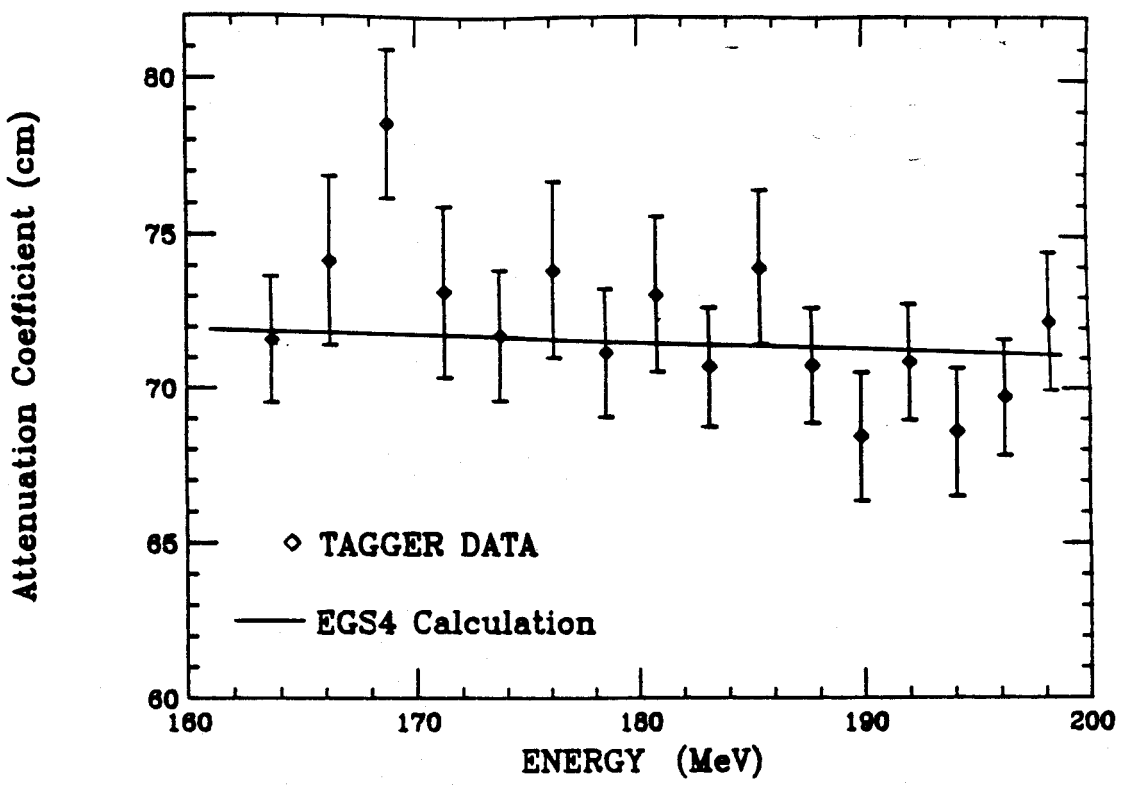

Figure 3.13: The attenuation coefficients for polyethylene from the measured (squares) and simulated data (solid line) in the energy range from 160 MeV to 200 MeV.

high full scale energies, large extrapolations from the standard source energies are necessary, and this can lead to errors. For high energy photons and detectors with moderate volume a significant fraction of the incident photon energy may leak out of the detector. The resulting peak corresponds to the most probable energy deposited in the active volume, and this shift to lower energies can be significant.

The method of calibration chosen was to compare the most probable energy deposition for the measured tagged photon data and the EGS4 simulations. The procedure for extracting the most probable energy deposition will be described in more detail in the section on the line shape analysis. A least squares fit to the line shape was made, and then the best-fit parameters were found. Using the best-fit value for the most probable energy deposition, a linear fit to a plot of channel number versus the EGS4 energy was computed. The slope of this line yielded the conversion coefficient from channel number to energy. As a cross check of this method the mean value $\langle E \rangle$ for the simulated data was compared to the measured data. The difference between the measured value, $\langle E \rangle_{meas}$, and the calculated EGS4 value,$\langle E \rangle_{calc}$, was found to have a mean value of 600 keV $\pm$ 600 keV for the data without the polyethylene absorber bar and -1.1 MeV $\pm$ 1.0 MeV for the data with the absorber in place.

With the problems of energy calibration of the detector at high full scale energies in mind, a decision was made to examine the energy deposition in the BaF_2 crystal from cosmic ray muons and compare their energy deposition to that of tagged photons. This was based on the fact that a portable and reproducible energy calibration was required for the bremsstrahlung measurements. Calibration with cosmic ray muons avoids the following problems which are all associated with extrapolating the relatively low energy gamma ray sources. For inorganic scintillators with long decay times such as BaF_2 the necessary gates on QDC modules need to be 1.5 - 2.0 μs, and this can lead to large pedestals which hamper peak identification. A method that

employs amplification of the photomultiplier tube output of low energy gamma rays suffers from problems with pedestals in the QDC as well. Since additional amplification of the signal is required, DC offsets can be introduced which effect the measured QDC pedestals. This method also suffers from the fact that for large volume crystals the production and transmission of the scintillation light is not the same at high energies as it is at low energies. The use of cosmic ray muons as a calibration does not suffer from large extrapolations in energy since the energy of the cosmic ray muon is approximately at half the maximum full scale energy used for this detector. Since there is no need to amplify the signal, the electronics set up is not changed, and the effect of the pedestal is not significant.

The procedure for the muon calibration was to observe the triple coincidence of the BaF_2 crystal and two 160 cm^2 plastic scintillators placed above and below the crystal. The paddles were placed at the end of the crystal furthest from the photomultiplier tubes to yield a more uniform light transmission to the photomultiplier tubes. A Monte-Carlo simulation of the detector response to cosmic ray muons using GEANT3 (version 3.10/3.11) [GEANT 86] was carried out. In these calculations dN/dE, the number of muons per unit energy bin, was generated using the data measured by Rossi [Rossi 48], and the angular distribution used was taken to be proportional to $\cos^2(\theta)$ [Particle Data Group 88]. As in the experimental measurement the requirement for a valid event was the triple coincidence of the BaF_2 detector and the two plastic scintillators. The position of the scintillator paddles above and below the crystal in the experimental set up were accounted for in the Monte-Carlo simulation. Figure 3.14 shows the energy deposited by cosmic ray muons measured at the Saskatchewan Accelerator Laboratory and the GEANT3 simulation. The shape of the measured spectra is reproduced by the simulation. However, the energy scales are slightly different. The centroid for the GEANT3 simulation is 85 MeV and is slightly

higher than the energy calibration based on the EGS4 simulations. The energy scale based on EGS4 calculations yields an equivalent energy deposition of 81 MeV. The discrepancy may be related to the reduced light collection in the experimental measurement. The muon energy deposition will serve as a means of calibrating the full scale energy in applications such as studying high energy gamma ray production in heavy-ion collisions at incident energies E/A= 50–150 MeV.

VI Analysis of the Line Shapes

Although the main goal of this study was to compare the tagger data to the EGS4 simulations, an analytical energy dependent fit to the measured line shape was also made. This was done in order to have an analytic expression to study the effect of the response function on the measured gamma ray spectra in heavy-ion collisions. In the detector study two functions were found to give a reasonably good description of the shape of the response to the incident gamma rays. The first function attempted was comprised of a Gaussian modified by an exponential tail on the low energy side. The exact expression for this function is given by:

$$y \sim G + exp\left(\frac{(E - E_p)}{\lambda}\right) \cdot (1 - G) \cdot \theta(E_p - E) \tag{3.7}$$

where

$$G = exp\left\{-4ln2 \cdot \frac{(E - E_p)^2}{FWHM_G^2}\right\} \tag{3.8}$$

This function was used by T. Matulewicz *et al.* in the study of the response of BaF_2 to photons from 3-50 MeV [Matulewicz 90]. The step function $\theta(x)$ is defined by:

$$\theta(x) = \begin{cases} 1, & \text{if x} \geq 0; \\ 0, & \text{otherwise.} \end{cases} \tag{3.9}$$

The shape described by Equation 3.7 has three free parameters, the peak position E_p, the width $FWHM_G$ of the Gaussian function and the parameter λ which describes the

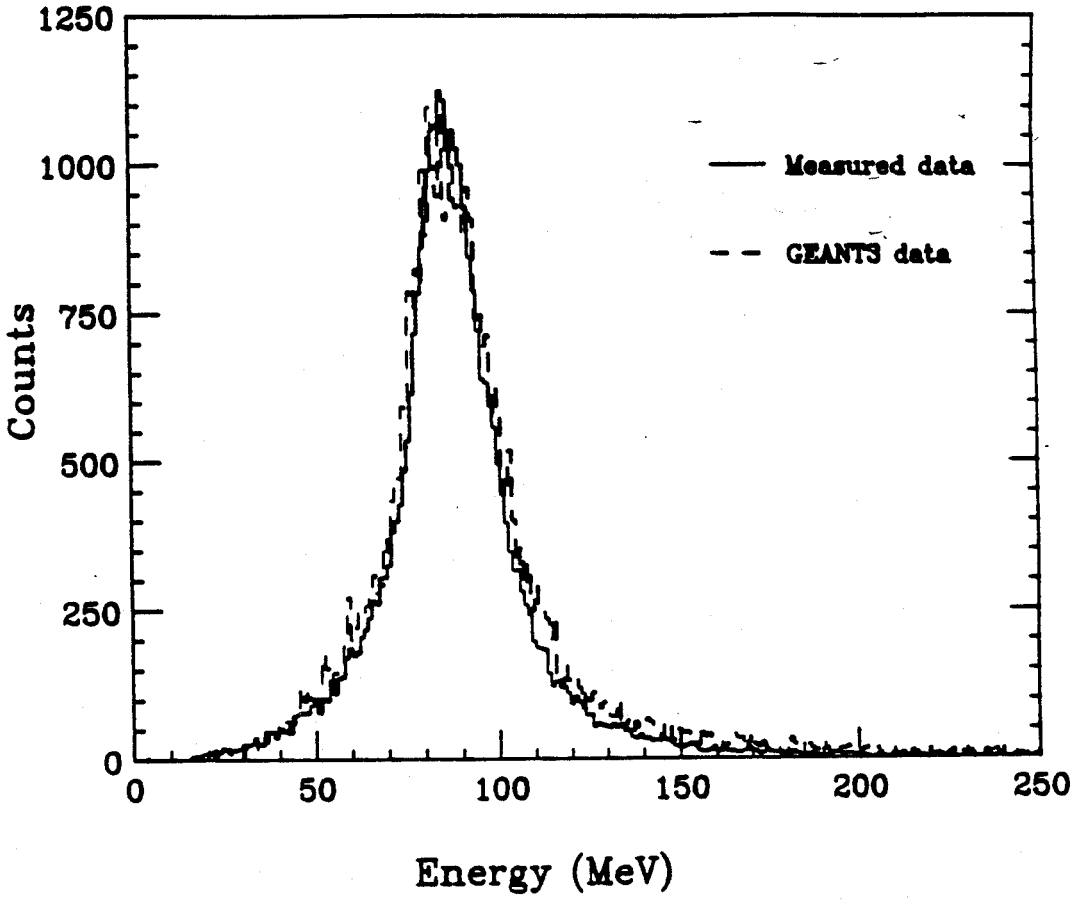

Figure 3.14: Energy deposition of cosmic ray muons in a large BaF_2 crystal. The measured spectra (solid) is compared to a Monte-Carlo simulation GEANT3 [GEANT 86] (dash). The energy scale of the measured spectra has been scaled by constant factor to compare the shapes of the energy response to cosmic ray muons. (see text)

asymmetry of the peak. The second function explored was the Extreme Value Distribution [Eadie 71] this function has one less free parameter than the previous function and has the following form:

$$y \sim exp\left\{\left(\frac{(E-E_p)}{\sigma}\right) - exp\left(\frac{(E-E_p)}{\sigma}\right)\right\} \tag{3.10}$$

In this parameterization the free variables are the peak position E_p and the width parameter σ. The best-fit parameters were found for both functions using a least squares minimization procedure with the minimization program MINUIT [Minuit]. An example of the quality of the fits for both functions is displayed in Figure 3.15. The Gaussian with low energy exponential tail yields a globally lower value for the χ^2, but the Extreme Value distribution has one less free parameter than the function Gaussian + low energy Exponential tail. Both functions have parameters that have a smoothly varying dependence on the incident photon energy, which can be fit with a polynomial of second order. The coefficients for the least squares fit of a polynomial of second order to the extracted parameters are listed in Table 3.3 and Table 3.4. The extracted widths for the fits to the data and simulations when the polyethylene absorber bar is in place are slightly different from the bare crystal measurements if the front anticoincidence shield is not used. However, the value of the most probable energy deposition does not change, and this is due to the nature of the energy loss process for gamma rays. When the polyethylene absorber is in front of the detector the incident gamma ray intensity is reduced by conversion to e^+e^- pairs. It should be stressed that the addition of a damping parameter to either the exponential tail in the Gaussian + Exponential function or the exponential in the exponent of the Extreme Value Distribution has no significant effect on the quality of the fits and would be rejected by the F-Test.

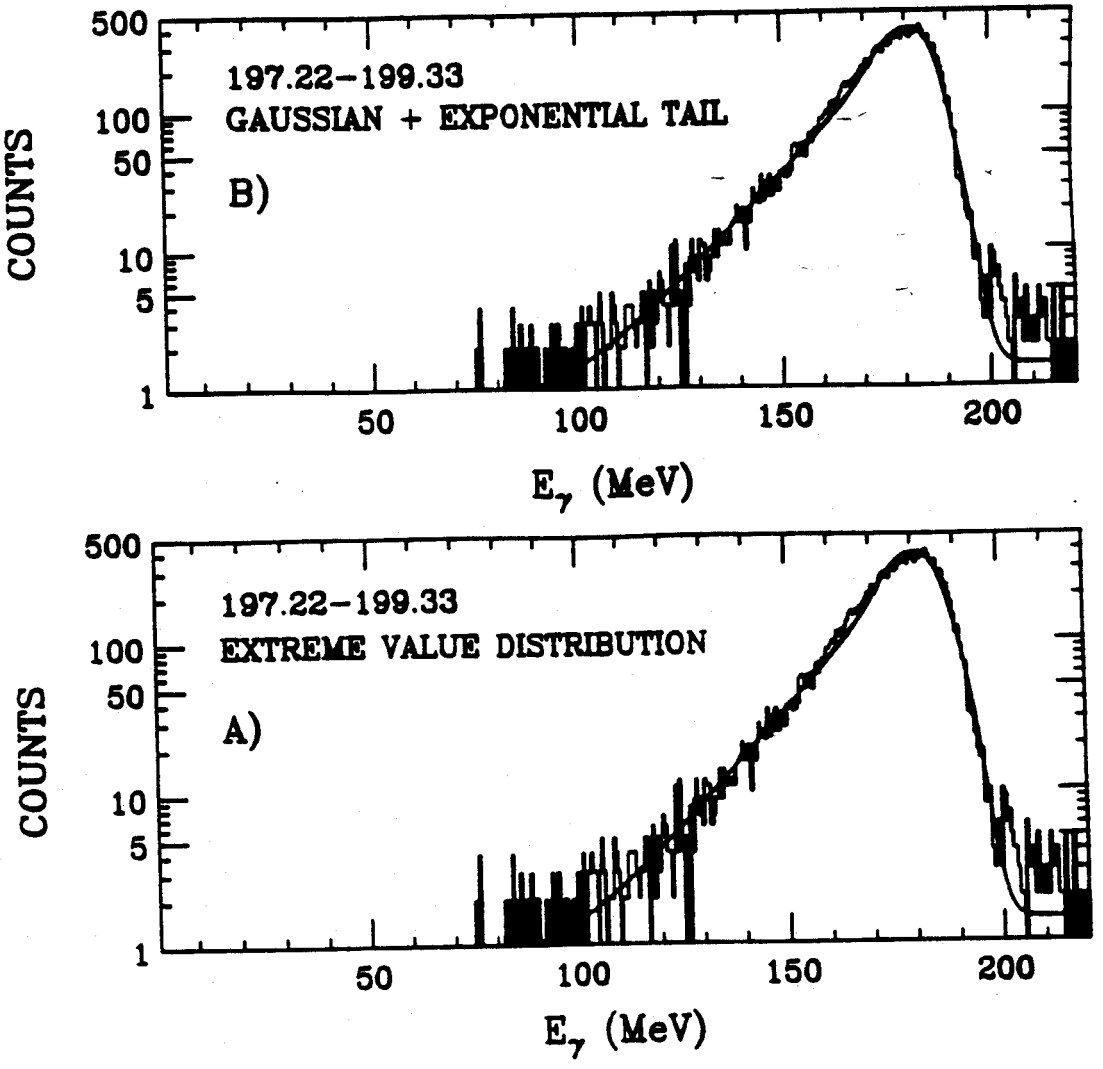

Figure 3.15: The experimental (histogram) and the analytical fits (solid) to the data using the function according (a) Equation 3.10 and (b) Equation 3.7.

Table 3.3: Coefficients of the polynomial $a_0 + a_1 \cdot E_\gamma + a_2 \cdot E_\gamma^2$ which describes the energy dependence of the parameters in Equation 3.7 over the energy range from 75 to 200 MeV.

Parameter (MeV)	a_0 (MeV)	a_1	a_2 (MeV^{-1})
E_p	4.4	0.90	-4.4×10^{-4}
$FWHM_G$	0.05	0.10	2.0×10^{-4}
λ	5.5	4.8×10^{-2}	1.2×10^{-5}

Table 3.4: Coefficients of the polynomial $a_0 + a_1 \cdot E_\gamma + a_2 \cdot E_\gamma^2$ which describes the energy dependence of the parameters in Equation 3.10 over the energy range from 75 to 200 MeV.

Parameter (MeV)	a_0 (MeV)	a_1	a_2 (MeV^{-1})
E_p	3.2	0.90	-5.3×10^{-5}
σ	1.4	0.04	-4.5×10^{-5}

VII The Systematics of the Energy Resolution

Of principle importance in describing the performance of any scintillator used in gamma ray measurement is its energy resolution over a large energy range. Figure 3.16 displays the ratio of the standard deviation over the incident photon energy versus the incident photon energy measured for our tests and from the literature [Matulewicz 90,Giehl 88,Lorenz 86]. Also displayed in Figure 3.16 is the contribution to the resolution from the finite size of the spectrometer focal scintillator paddles. The effect of the paddles on the measured energy resolution is insignificant. The crystals used by Matulewicz were 20 cm long right cylinders (10 radiation lengths) with a hexagonal cross section. The other detectors were BaF_2 calorimeters having a total lengths of 30 and 40 (14.6 and 19.5 L_{rad}) cm and a diameter of 13.5 cm. The diameters of the calorimeters used by Giehl *et al.* [Giehl 88] and Lorenz, Mageras and

Vogel [Lorenz 86] were slightly larger than the diameter of the crystal used in this work. However, their detector was significantly longer than the present detector. Since the resolution depends strongly on geometry of the crystal, there is a slight difference in the resolution as shown in Figure 3.16.

Since the use the ratio σ/E_γ as a measure of the resolution implies a Gaussian type response function, and the response of this BaF_2 detector is not Gaussian. The definition for the experimental resolution used was given by:

$$R = \frac{FWHM}{E_p} \tag{3.11}$$

The results are displayed in Figure 3.17, which is a plot of the resolution versus $1/\sqrt{E_p}$, also displayed in Figure 3.17 is a least squares fit to the resolution. The function used describes the detector resolution to leading order in powers of $1/\sqrt{E}$ as$(4.4\% \pm 0.3\%)/\sqrt{E_p}$ where E_p is in GeV. The exact expression used for the fitted response function is [Knoll 79] :

$$R = \frac{\sqrt{(\alpha + \beta \cdot E_p)}}{E_p} \tag{3.12}$$

The term $\propto \alpha/E_p^{3/2}$ indicates that there are nonstatistical sources of peak broadening. However, the contribution of this term to the resolution is small. The ratio of FWHM/σ differs dramatically from the constant value 2.354 which is expected for a Gaussian line shape. The average value over all of the measured energy bins for the ratio FWHM/σ was 2.9 ± 1.0.

The intrinsic resolution of BaF_2 has been reported by Giehl *et al.* [Giehl 88]. Their measurements were performed at energies from 60 MeV to 7 GeV. The intrinsic resolution was defined as:

$$\sigma_i = \sqrt{\sigma_{exp}^2 - \sigma_{EGS4}^2} \tag{3.13}$$

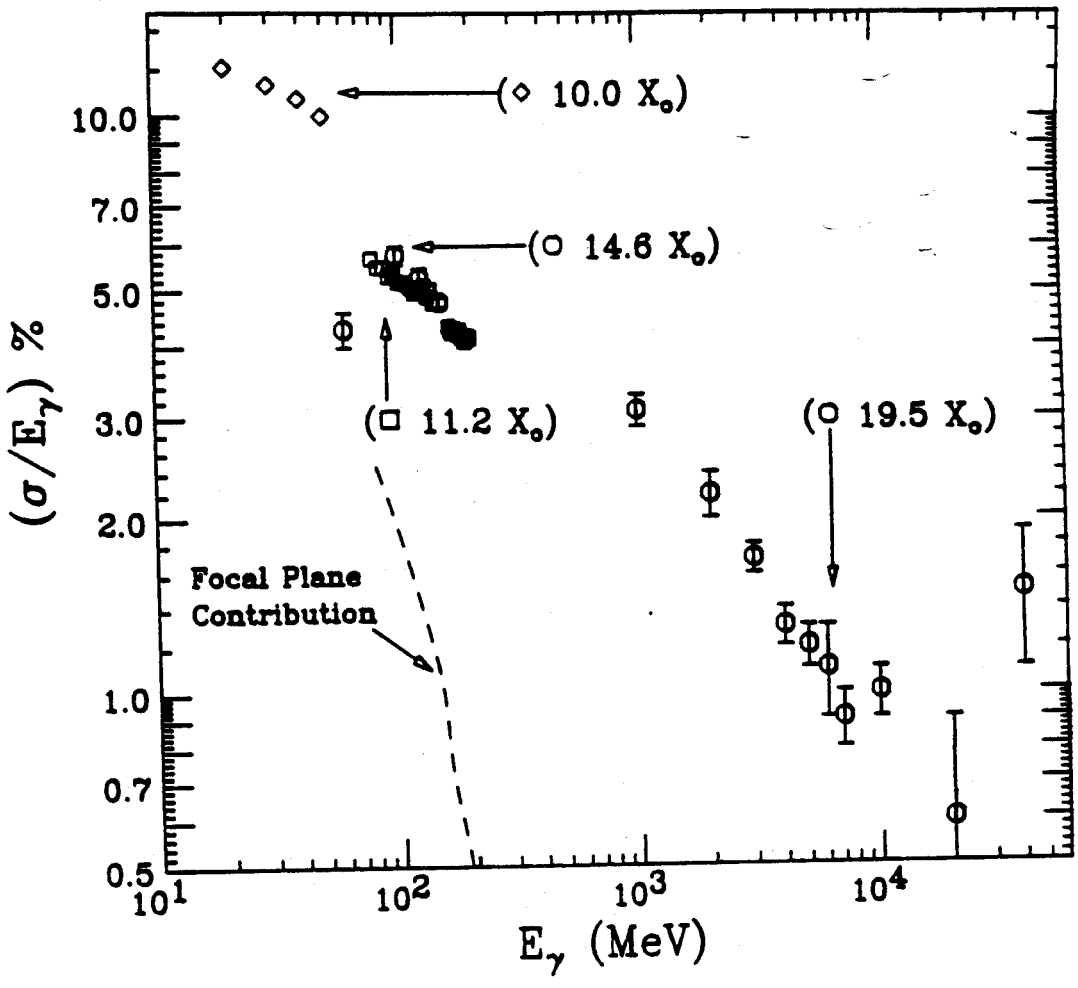

Figure 3.16: Ratio of the standard deviation over the incident photon energy as a function of photon energy for various BaF_2 detectors. The diamonds are from [Matulewicz 90] the circles are from [Giehl 88] and [Lorenz 86].

where σ_{EGS4} includes the beam spread, leakage fluctuations and the photoelectron statistics. The value of σ_i should describe the intrinsic properties of the scintillating material. In the present data the differences between the experimental and calculated standard deviations were found to be small. The difference between the standard deviations of the two spectra has a mean value of -0.2 MeV ± 0.5 MeV for the bare crystal and 0.9 MeV ± 0.2 MeV for the crystal plus polyethylene rúns. As previously discussed, light collection efficiency and nonlinearity in the electronics can influence the differences between the measured data and the simulations. As was pointed out in the work of Matulewicz *et al.* [Matulewicz 90], a quadratic formula for the intrinsic resolution assumes a Gaussian shape which is not the case for these measurements. Therefore, the conclusion was that within the accuracy of the measurements, no contribution to the intrinsic resolution of BaF_2 was observed that is not already accounted for in the EGS4 simulations.

VIII Summary and Conclusions

The response of a BaF_2 detector, 12.5 cm diameter and 22.9 cm long has been measured with photons in the energy range 75-200 MeV. The experimental spectra are in reasonable agreement with predictions for the resulting electromagnetic shower using the Monte-Carlo code EGS4. The energy calibration of the BaF_2 crystal was carried out by comparing the measured and simulated spectra. At higher incident energies the observation was made that a significant fraction of the electromagnetic shower is leaking out of the BaF_2 detector both experimentally and in the Monte-Carlo simulations. This leakage has a detrimental effect on the resolution of the detector and causes a shift of the most probable energy deposited in the active volume of the BaF_2 crystal to lower energies. A method for reestablishing the calibration described above uses cosmic rays passing through the detector in a defined geometry. The

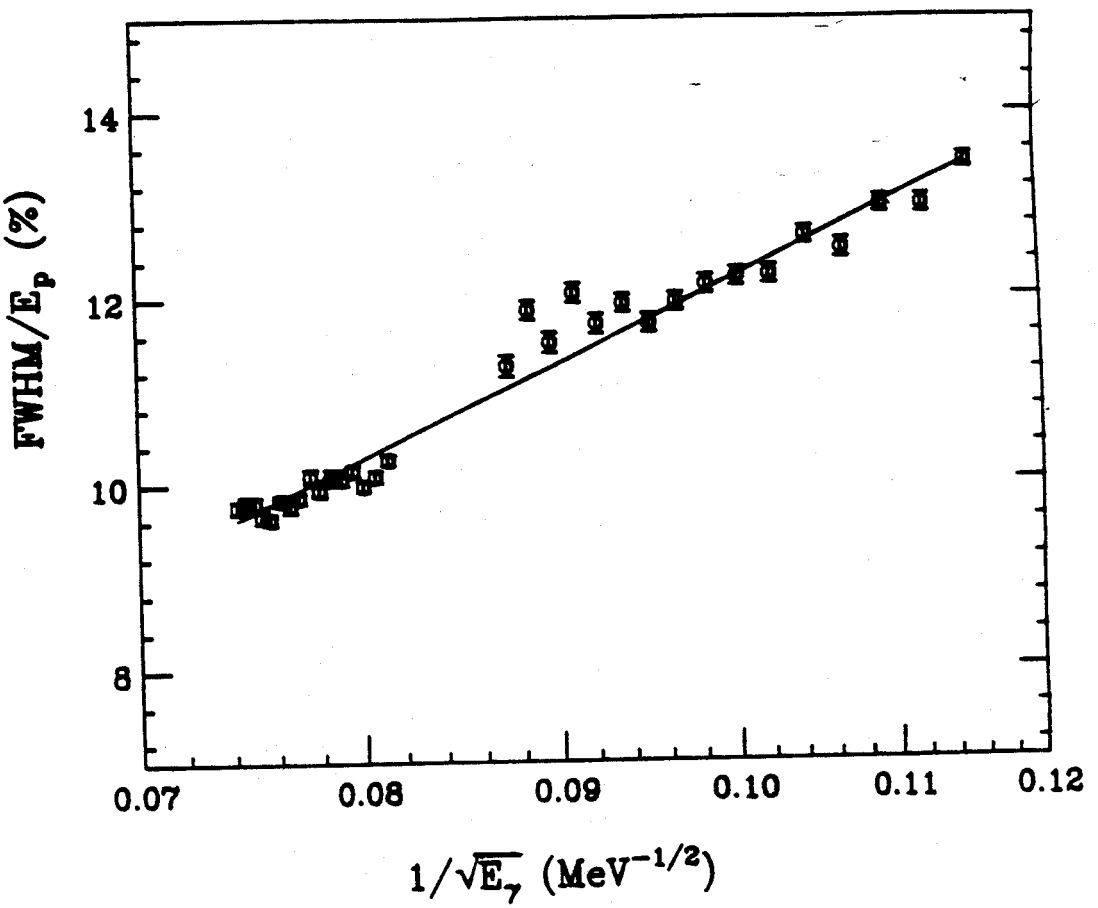

Figure 3.17: A plot of the resolution for the BaF_2 crystal described in this work versus the function $1/\sqrt{E}$. The solid line is a least squares fit to the experimental data by the function given in Equation 3.12.

method is portable and reproducible.

In addition to the comparison of the measured spectra to the Monte-Carlo simulations, a least squares fit to the data with an analytical function was performed. The smooth energy dependence of the extracted fit-parameters can be approximated by polynomials up to second order.

Chapter 4

The Proton-Nucleus Bremsstrahlung Experiment

I Introduction

The possibility of bremsstrahlung in a nucleus–nucleus collision was first noted in a paper by Ashkin and Marshak [Ashkin 49]. In a more refined calculation by Simon [Simon 50], the cross section was predicted to be on the order of the elastic scattering cross section multiplied by the square of the fine structure constant. In the heavy-ion branch of nuclear physics, high energy gamma rays were first suggested by Eisberg *et al.* [Eisberg 60] as a method to distinguish between compound nucleus reactions and direct reactions. The predicted gamma ray spectrum was expected to be sensitive to the time delay between cessation of the current associated with the incident particle and the initiation of the current associated with the outgoing particle. The theoretical predictions were made only for photons in the approximation that the wavelength of the emitted photon is long compared to nuclear radii and hence for energies much lower than the photons of interest in this work. The field was relatively dormant until the early 1980's when several groups detected high energy gamma rays in various experiments.

A Experimental Overview

In an experiment performed at Lawrence Berkeley Laboratories Budiansky *et al.* [Budiansky 82] studied gamma ray production between 40–500 MeV emitted in collisions at E/A = 2 GeV. The production of the gamma rays by nucleus-nucleus bremsstrahlung was suggested to explain the excess yield in the measured spectra from studies on the decays of particles such as π^0, η, and Δ. However, no evidence of the process was observed because it was obscured by the large π^0 background.

High energy gamma rays in intermediate energy heavy-ion collisions were observed for the first time by two independent experimental research groups. Grosse *et al.* [Grosse 85] at GSI observed higher than expected yields of single photons while studying π^0 production with an array of lead glass detectors. In a measurement performed at MSU, Beard *et al.* [Beard 85] found a large background of positrons and electrons present in a charged pion experiment. They found that the leptonic background was associated with the conversion of high energy photons in the collimator of the pion spectrometer.

Since the discovery of high energy gamma rays in intermediate heavy-ion reactions by Grosse *et al.* and Beard *et al.*, the thrust of the experimental work has concentrated on understanding the production mechanism. The measurements on the inclusive photon production cross section have explored the periodic table from light systems such as $^2H + ^{12}C$ [Tam 89a] to heavy systems such as $^{136}Xe + Sn$ [Clayton 89]. The energy dependence of high energy photon production has been studied from the range of compound nucleus formation roughly E/A = 10 MeV [Murakami 89] up to an incident energy of E/A=125 MeV [Clayton 89]. The general features of the measured spectra can be summarized as follows:

1. The measured energy spectra are a decreasing exponential with a slope

parameter that only weakly depends on the the target and projectile size.

2. In the laboratory frame the angular distribution is forward peaked and can be readily transformed to a rest frame where the emission is nearly isotropic or isotropic plus dipole components. The rest frame is the nucleon-nucleon center-of-mass frame which is roughly one half the beam velocity.

3. The strength of the dipole component decreases for heavier systems [Tam 88] and also for higher incident energies [Clayton 89].

There have been a few exclusive measurements to obtain a more detailed understanding of the production mechanism. Hingmann *et al.* [Hingmann 87] studied high energy gamma rays the reaction $^{40}Ar + ^{158}Gd$ at E/A=44 MeV in coincidence with reaction products that provided information on the impact parameter of the collision. In a measurement performed at MSU by Lampis *et al.* [Lampis 88], the high energy gamma ray production was studied in coincidence with light charged particles in the reaction of E/A= 30 MeV $^{14}N + Pb$. It was found that the ratio of the gamma ray–proton coincidence cross section to the product of the singles cross sections was only slightly greater that 1.0, which indicated a very weak dependence on the impact parameter. There have been other coincidence measurements that study the relationship of the observed particle multiplicity and the measured gamma ray energy spectra [Kwato 88b,Hermann 87].

There have been several studies of high energy gamma ray production for light-ion induced reactions [Edgington 66,Koehler 67,Kwato 88a,Pinston 89,Pinston 90,Tam 89a]. The first major study of high energy gamma ray production in proton induced reactions was undertaken in 1966 by Edgington and Rose [Edgington 66]. In this measurement Edgington and Rose extended the bremsstrahlung cross section measurements over a wide range of targets and angles. A measurement was also performed by Koehler

et al. [Koehler 67] who studied neutron–proton bremsstrahlung with 197 MeV protons bombarding a liquid deuterium target. There was disagreement between these two measurements, but no other confirmation measurement was attempted. The work of Edgington and Rose was to go unchallenged until 1988 when the measurements by Kwato *et al.* and by Pinston *et al.*, who were studying high energy gamma ray production performed a series of proton induced bremsstrahlung measurements at 72 [Kwato 88a], 168 and 200 MeV [Pinston 89]. The results of the measurements share some of the same basic features as the heavy-ion induced reactions, however, there are some differences. In heavy-ion data, although it is possible to observe photons up to 2 to 3 times the incident beam energy/nucleon, the observed photon energy accounts for only a small fraction of the total available energy. However, in proton induced reactions, gamma rays can be observed up to the maximum energy available. This difference has been attributed to the absence of Fermi motion in the projectile. The results of the data from the measurements of Pinston *et al.* and Kwato *et al.* indicated that the total cross section data of Edgington and Rose were incorrect by a factor of 2.3–3.0. Since many of the theoretical models used the data of Edgington and Rose as a gauge of the accuracy of their gamma ray production mechanism this discrepancy is important. The measurement performed by the MSU research group on proton induced reactions would be another check on the validity of the Edgington and Rose data. It was also felt that with the good resolution and detection characteristics of the BaF_2 detector a better measurement regarding the endpoint energy and angular distribution could be made. This was based on the fact that the data of Kwato *et al.* and Pinston *et al.* used a BaF_2 converter plus a large NaI(Tl) crystal detector system that has moderate resolution [Bertholet 87] and possible background problems at forward angles due to the large component of fast neutrons and protons.

II Theoretical Overview

There have been several theoretical models proposed for the high energy gamma ray production mechanism. These models can be classified into three basic categories:

1. Nucleus–Nucleus Bremsstrahlung.
2. Nucleon–Nucleon Bremsstrahlung.
3. Statistical Emission.

In the discussion below, the main features of each classification will be addressed.

A Nucleus–Nucleus Bremsstrahlung

In a paper published in 1977, J. I. Kapusta [Kapusta 77] suggested that the nucleus-nucleus bremsstrahlung model would explain the experimental data for high energy gamma rays below 10 MeV. It was also suggested that the study of gamma rays in the energy range from 10 to 140 MeV would also yield information on the nucleus–nucleus bremsstrahlung model. This was followed by a paper in 1985 by Vasak, Mueller and Greiner [Vasak 85] who studied gamma ray production above 10 MeV in a collective nucleus–nucleus bremsstrahlung model. In this model the photons were thought to be produced in the early stages of the collision by coherent bremsstrahlung of the projectile and target nuclei. The model predicted a quadrupole angular distribution in the nucleus–nucleus center–of–mass frame, and a Z^2 dependence of the photon emission cross section. It was predicted the information on the yield of high energy gamma rays offered the possibility of measuring the nuclear "stopping time" as well as on the compressibility of nuclear matter. It should be noted that the quadrupole angular distribution with a minimum at 90° would be predicted for symmetric systems as well as for systems with the projectile and target having the same A/Z ratio. A

comparison to the data on the symmetric systems such as $^{12}C + C$ [Grosse 86] and for the similar A/Z ratio system $^{14}N + C$ [Stevenson 86] clearly rule out the nucleus–nucleus bremsstrahlung as the main component in the measured gamma ray spectrum.

Ko, Bertsch and Aichelin [Ko 85] calculated bremsstrahlung within the intranuclear cascade model (INC) [Bertsch 81] which allowed them to make predictions about the relative strengths of the incoherent and coherent photon production. For systems with both target and projectile masses $(A_t, A_p) < 20$ they found that the dominant process was incoherent neutron–proton bremsstrahlung. However, for systems with $(A_t, A_p) \geq 40$, they showed that the coherent component at $E_\gamma \leq 40$ MeV might be observed. The signature of coherent bremsstrahlung would be the change in the angular distribution in the emitting frame from isotropic plus dipole components to a distribution with a quadrupole shape. In a measurement performed with a very heavy system $^{136}Xe + Sn$ at incident energies of E/A= 89 and 124 MeV, the MSU research group found no significant anisotropy [Clayton 89]. In fact the data could be explained within the framework of incoherent nucleon–nucleon bremsstrahlung.

The nucleus–nucleus bremsstrahlung contribution to the gamma ray yield has been studied by Bauer *et al.* [Bauer 86a] in the framework of the time dependent Hartree–Fock (TDHF) theory and was found to be at least an order of magnitude too small to explain the experimental data.

Nucleon-Nucleus Bremsstrahlung

An approach which used the infinite nuclear matter approximation to study the contribution to the bremsstrahlung yield from collisional processes within the nuclear mean field were carried out by Nakayama and Bertsch [Nakayama 86]. They found that the contribution to the gamma yield from this source was negligible for heavy-ion

collisions. However they made some predictions regarding the shape of the gamma energy spectra in proton induced reactions these predictions have been used to describe the measured energy spectra in this work, and the details of that calculation will be discussed when comparisons to the data are displayed.

B Nucleon–Nucleon Bremsstrahlung

In nucleon–nucleon bremsstrahlung it is the individual nucleon–nucleon collisions that are responsible for the bremsstrahlung photons. Here there are two types of bremsstrahlung, neutron–proton and proton–proton. The former is the dominant component since it has a non zero dipole component in the expansion of the magnetic vector potential $\vec{A}$. In Equation 4.1 the total photon production cross-section is expressed in terms of the radiated intensity and is given by [Jackson 75b]:

$$\frac{d^2\sigma(E,\theta)}{dEd\Omega} = \frac{\sigma_r}{E} \cdot \frac{d^2I(\omega,\theta)}{\hbar d\omega d\Omega} \tag{4.1}$$

where E = $\hbar\omega$ and σ_r are the scattering cross section and $d^2I/d\omega d\Omega$ is the energy radiated by the accelerated charges per unit frequency interval and unit solid angle. The radiated intensity is expressed in terms of the vector potential $\vec{A}$:

$$\frac{d^2I}{d\omega d\Omega} = \frac{e^2}{4\pi^2 c}\left(\sum_i \vec{A}(\omega,\theta)\right)^2 \tag{4.2}$$

and $\vec{A}$ is given by:

$$\vec{A}(\omega,\theta) = Z_1 \int_{-\infty}^{\infty} \exp^{i\omega\left(t-\frac{\vec{n}\cdot\vec{r}_i(t)}{c}\right)} \cdot \frac{d}{dt}\left(\frac{\vec{n}\times(\vec{n}\times\vec{\beta}_i)}{1-\vec{\beta}_i\cdot\vec{n}}\right) dt \tag{4.3}$$

$\vec{n}$ is the direction of observation, $\vec{r}_i$ and $\vec{\beta}_i$ are the position and velocity vectors of the i_{th} particle. In the soft photon approximation, which is that the wavelength of the emitted photon is long compared to the size of the nucleus, the details of the motion can be ignored, and the scattering event can be characterized into a double

and simultaneous acceleration sequence in which the velocity decreases from β_i to 0 in the initial direction and increases from 0 to β_i in the final direction. For hard sphere scattering, the equation reduces to the following simple expression:

$$\frac{d^2\sigma}{dEd\Omega} = \frac{e^2\sigma_r\Delta\vec{\beta}^2}{4\pi^2\hbar c}\left(\frac{2}{3} + sin^2(\theta)\right) \tag{4.4}$$

The same expression can be derived for neutron–proton scattering as well [Nifenecker 85,Cassing 86]. The proton–proton bremsstrahlung case was derived by Nifenecker and Bondorf [Nifenecker 85] and they find it to be reduced relative to the neutron–proton bremsstrahlung by a factor of the order $\beta^2 + (\frac{E}{197.3})^2\Delta R^2$. For a gamma ray of 100 MeV and typical values of β this yields a reduction of about a factor of ten. Magnetic dipole radiation could also be considered due to the spin flips if the nucleons during the scattering process. However, it can be shown [Jackson 75c] that the strength of the magnetic dipole radiation is reduced with respect to the electric dipole radiation by a factor $\omega^2\mu^2/4 \simeq E^2/4$ which is less than 0.001 for gamma rays at 100 MeV.

Most of the recent theoretical models of high energy gamma ray production are based on the microscopic production mechanism being incoherent neutron–proton bremsstrahlung from the individual neutron–proton collisions within the colliding nuclei [Bauer 86a,Bauer 86b,Biro 87,Cassing 86,Nifenecker 85,Remington 87]. In all of the calculations mentioned, the production cross section used is of the form of Equation 4.3 which employs the long wavelength approximation. Within these models the gamma rays are attributed to the first chance neutron–proton collisions early in the reaction and it this fact that make these gamma rays an interesting probe of the dynamics of the collision process because once these photons are created they have a high probability to escape without another interaction.

C Statistical Emission

These models can be classified into two categories which depend primarily on the treatment of the time evolution of the hot system. The first of the two types of models that have been used are phase space models [Grosse 85,Shyam 86]. In these models, a freeze out configuration is selected under the assumption that thermodynamical equilibrium exists. The relative production of particles is then governed by the chemical potential. This approach has not been extensively used for photon production.

The other type of thermal models used in studies of gamma ray production have been based on the more traditional evaporation theory which is then applied to a hot participant zone. The participant zone has been defined in several different ways, Nifenecker and Bondorf [Nifenecker 85] assumed an equal number of participants from both the target and projectile. In similar work by Prakash *et al.* [Prakash 88] a clean cut geometrical participant model is invoked. In calculations by Bonasera *et al.* [Bonasera 88] this approach was modified in order to take into account the interactions between the participants and the spectators which is expected important at intermediate energies. The major difference between the models of Nifenecker and Bondorf [Nifenecker 85] and the work by Prakash *et al.* [Prakash 88] stems from the treatment of the photon production cross section. Nifenecker and Bondorf assumed that the photons are produced in individual nucleon–nucleon collisions, with each collision being treated semi-classically as previously described. Prakash *et al.* uses detailed balance to obtain the photon production rate from the inverse process, photo-absorption. Both of these treatments lead to a similar expression for gamma ray production which is that the rates are proportional to the total mass of the participant zone. In the model of Nifenecker and Bondorf it was found that the calculated temperatures were systematically too low ($\approx$ 65%). However, later work by Neuhauser and Koonin

[Neuhauser 87] showed that if proper treatment of the Fermi motion and Pauli blocking, as well as a realistic treatment of the elementary N-P-γ cross section were done, this could have a significant improvement on the comparison between data and the theoretical calculations. Thermal models have a great deal of difficulty explaining two experimental features:

1. The similarities between proton-nucleus and nucleus-nucleus reactions.
2. The existence of an anisotropic component in the angular distribution.

The former is due to the dilemma of imagining an equilibrated hot zone made of only two or three nucleons. While the latter feature might tempt one to resort to angular momentum effects to help explain this effect, but this would not help since the experimental data exhibits a stronger anisotropy for smaller systems [Tam 88].

III Experiment

The experiment to study high energy photon production from proton induced reactions using BaF_2 detectors was carried out at the Indiana University Cyclotron Facility. Self supporting targets of CD_2, carbon, zinc and lead were bombarded with a proton beam at incident with energies of 145 and 195 MeV. Data was also measured at an incident proton energy of 104 MeV with the same targets with the exclusion of the CD_2 target. The use of the CD_2 target allowed the measurement of the high energy photon production cross section of deuterium. The deuterium measurement is important due to the fact that the two nucleons are not tightly bound and, therefore, may serve as an approximation to the free neutron–proton bremsstrahlung cross section.

A Experimental Vault Layout

The BaF_2 detectors were placed on the two movable platforms formerly used for the decommissioned QDDM Spectrometer at IUCF. The BaF_2 detectors were then easily rotated about the target to cover the angular range from 45 to 135 in the laboratory frame. This also allowed extensive cross checking of the detectors at the same angle. The detectors were placed 75 cm from the target, and at this distance, each detector subtends a solid angle of 11 msr. This is determined by the heavy metal collimator (95% tungsten) placed in front of the detector. The detector was surrounded by a 2.54 cm thick plastic scintillator anticoincedence shield, and was used to reject cosmic ray muons as well as prompt charged particles from the target. To attenuate the background from prompt particles from the target, a high density polyethylene bar was placed between the target and the front of the crystal. The length of absorber used was angle dependent with a 40 cm bar for angles less than 90° and a 20 cm bar for angles of greater than or equal to 90° in the laboratory. Typical beam currents used during the run were in the range from 5 to 10 nA and were dependent on the position of the BaF_2 detectors. Since the yields of charged particles and neutrons are strongly forward peaked in the laboratory frame, the background from these particles is greatly reduced at angles greater than 90° in the laboratory.

In an attempt to monitor the room background as well as a reasonable cross check of the incident beam current, four BGO detectors were placed at symmetric locations in the vault. Two were placed below the horizontal plane containing the beam and target and the other two were placed above this horizontal plane at forward angles. These positions were chosen to assist in tuning the transport beamline for minimum room background, since their placement allowed the checking of left-right count rates as well as forward to backward rates. The experimental vault layout is shown in

Figure 4.1.

A calibration of the beam current was attempted utilizing the following reaction $^{27}Al(p,3pn)^{24}Na$ which has a known cross section of 10.9 $\pm$ 0.4 mb [Yule 60]. The total number of protons detected by the Faraday cup during the irradiation was 6.064 x 10^{13}, and from the activation measurement gave a a value of 8.75 x 10^{13} for the number of protons. This corresponds to a difference of about 45%. Such a large difference might be due to the uncertainty of the Ge(Li) detector used by the detector laboratory personnel at IUCF. The group was unable to determine accurately the detection efficiency of the Ge(Li) detector used to count the gamma rays from the ^{24}Na. Although the results for the two methods are different, the current measured by the Faraday cup was considered to be the more accurate and was used exclusively in the results presented below.

B Electronics Set-up and Data Acquisition

Figure 4.2 shows the electronics block diagram for the various detectors used in this experiment. To fire the master gate, an analog signal from the sum of the three quartz photomultiplier tubes had to be higher than the level set on a Constant Fraction Discriminator (CFD). A accepted event arises when one of the BaF_2 detectors fires in coincidence with the computer "Not Busy" signal generated in the CAMAC crate by the data acquisition computer. When these conditions were met the signals from the specific BaF_2 detector were read and then packed in a buffer which was stored on magnetic tape or shipped to the on–line histogramming package SARA. The on–line data were sampled in a rate dependent manner.

The data acquisition system consisted of two MC68020 processors running a commercial real time kernel (pSOS) and implemented in a high level language (C). Also included in each CPU board is one MC68881 coprocessor which can do several func-

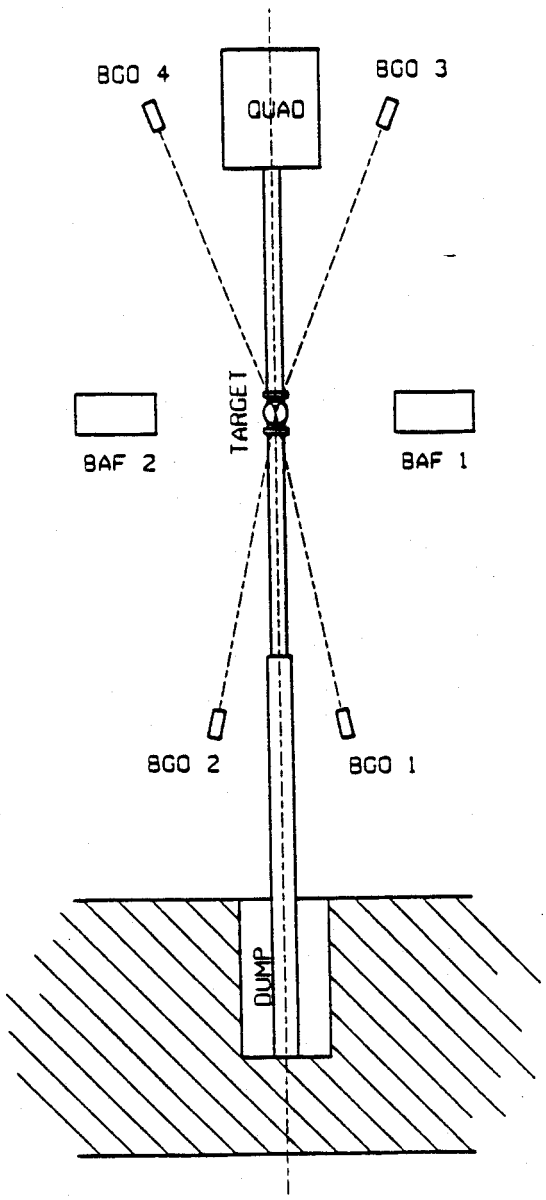

Figure 4.1: A schematic showing the experimental vault set up at the Indiana University Cyclotron Facility

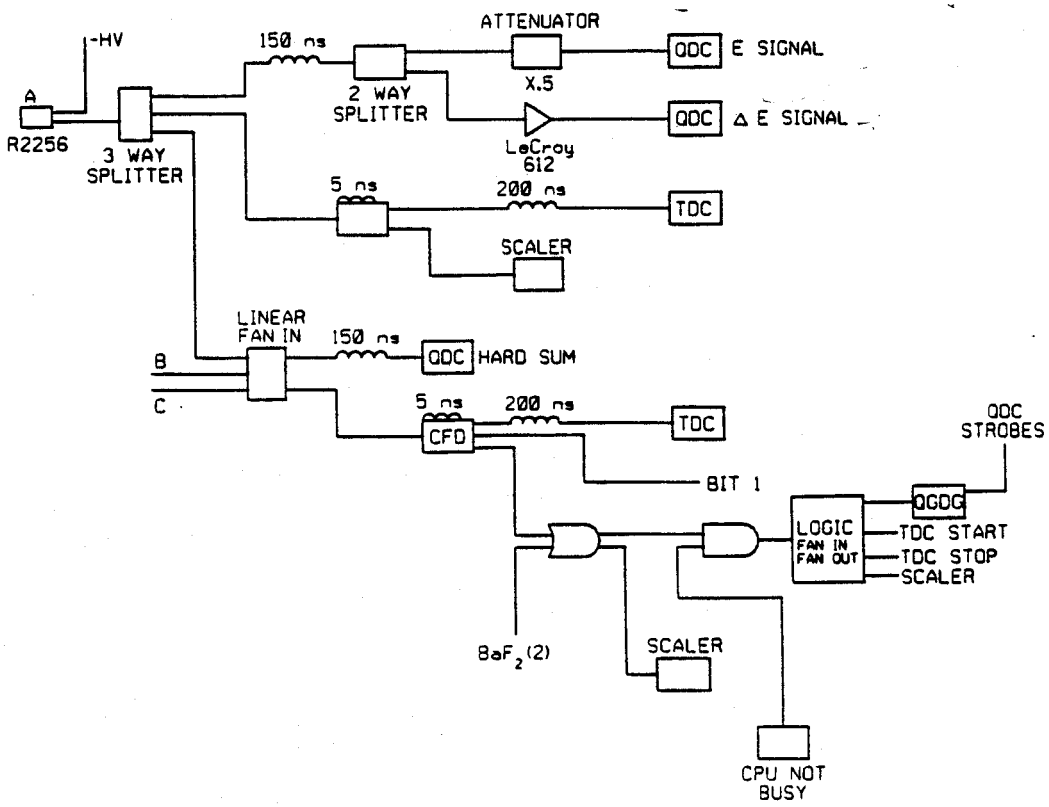

Figure 4.2: An electronics block diagram for the proton induced bremsstrahlung experiment performed at the Indiana University Cyclotron Facility

tions such as floating point calculations. The system was attached to the on-line computing system at NSCL via a high performance ETHERNET protocol. The CPU boards used were Ironics IV3220 in a mode as Master and Slave computer, and data buffers were sent to the various interested consumer processes, such as a scaler display program, via NSCL ETHERNET by an intelligent Ethernet board, the ENP 10. The **MASH**, which is an acronym for Mobile Acquisition System Hardware, was developed by Ron Fox *et al.* [Fox 89] from the Cyclotron Laboratory at MSU. The use of this system allowed the user to write and debug the acquisition programs before leaving MSU, and once arriving at the laboratory where the measurement is to be performed the user is able to run independently of the host institution's computer system. With this system there is no need to complicate the experiment by having to learn all the commands and nuances of other types of data acquisition systems and analysis programs at the remote experimental site. A simple schematic presenting the flow of data for the MASH is shown in Figure 4.3. Another important feature of the MASH system is the ability to implement a preprocessor program or filter program. With assistance in the coding by Ron Fox a filter program was installed in the master CPU program to reject gamma ray events which were below a given threshold $\approx$ 8 MeV for carbon and CD_2 and 12 MeV for zinc and lead respectively. The program was structured in such a manner that each detector had individual thresholds, and the rejection could be turned on/off for each detector. This simple cut on low energy gamma rays could have been completed by just raising the threshold on the CFD, but since the resulting spectrum can be distorted near the threshold, it was decided that the CFD threshold would be set lower than the intended cut and the front end computer would make the clean cut on gamma ray energy. This amounted to a reduction of $\approx$ 50% in the events on the data tape. This saves on magnetic tape as well as in CPU time later since these events would be rejected by software cuts during

playback. It should be noted that these are the only cuts on the gamma ray energy used in the data analysis.

IV Background Suppression

Even with the front end rejection of low energy events there were still background events from charged particles and neutrons as well as cosmic ray muons. The rejection of these events will be addressed in the following sections.

A Rejection of Neutrons and Charged Particles

A major source of background in high energy gamma ray measurements comes from energetic neutrons. Neutrons are produced at a rate roughly 10^4–10^6 times the rate of high energy gamma rays, and, unlike charged particles, they can not be rejected by an active plastic anticoincidenece shield. The main method used to discriminate neutron events from high energy gamma rays was discrimination by time–of–flight (TOF). A two dimensional plot is generated of the measured gamma ray energy versus the RF timing signal. If a projection along the time axis is done as in Figure 4.4, neutrons which have velocities less than the speed of light show up as a broad "bump" at later times than the very sharp time of the constant velocity gamma rays. It should be noted that for gamma rays above 10 MeV the time resolution of the BaF_2 detector is 850 ps FWHM, which is still limited by the width of the RF pulse. By placing a gate on this sharp peak, the background of slow moving neutrons was reduced by about 85%. A similar width gate was also placed in a region of the time spectrum which has a constant background, and this allows the subtraction of the random events from the true gamma ray events. The secondary method of rejecting neutrons is by the use of the pulse shape information in the BaF_2 scintillation light output. High energy neutrons which can not be rejected by TOF methods can be rejected by placing a cut

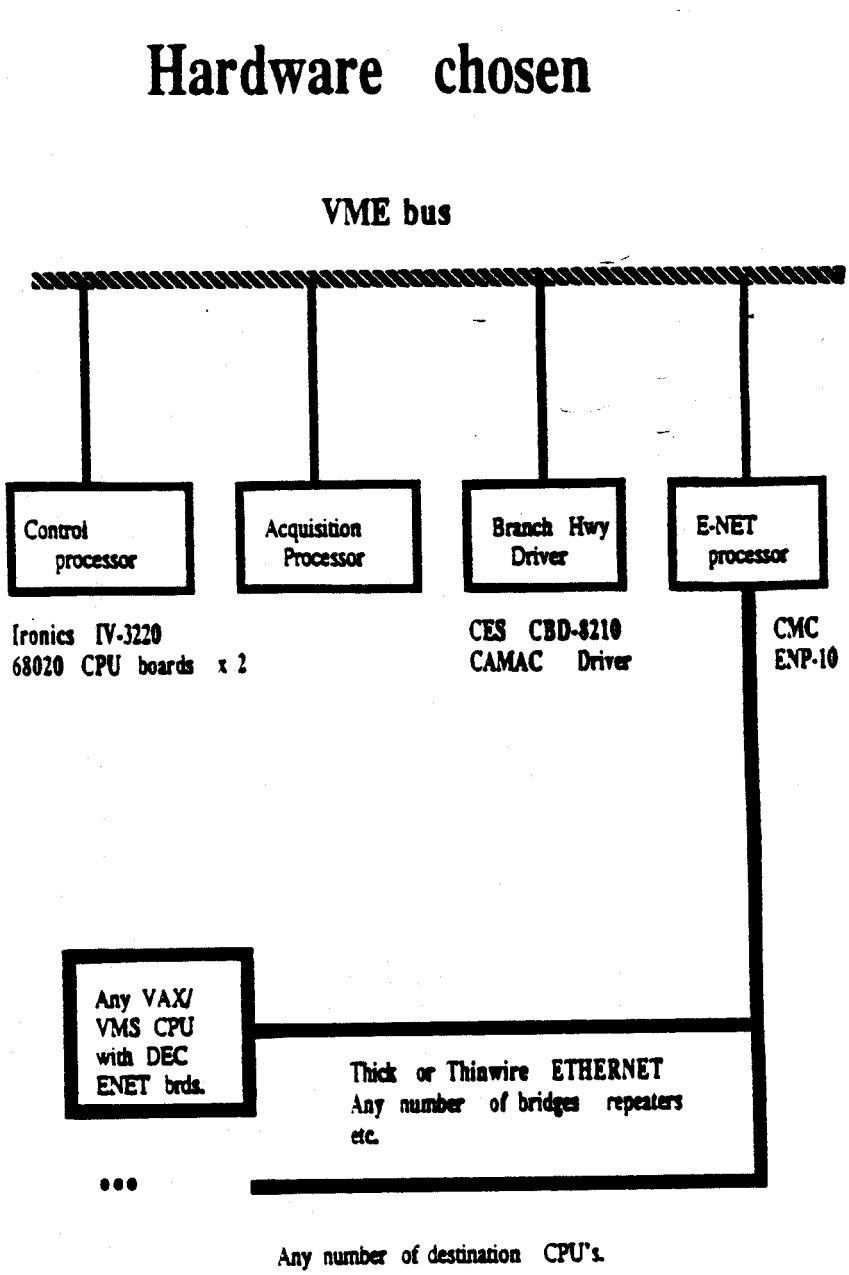

Figure 4.3: A schematic diagram of the Mobile Acquisition System Hardware (MASH) used at the Indiana University Cyclotron Facility

on the two dimensional spectrum of the fast component of the light output versus the total light output. A typical pulse shape discrimination (PSD) signal is displayed in Figure 4.5. The relativistic particles such as e^+e^- pairs and muons lie in the upper band, and neutron and charged particle events lie in the lower band. It has been shown by Matulewicz *et al.* [Matulewicz 89] that for neutrons with incident energies greater than 25 MeV the reaction mechanism in BaF_2 changes from Ba(n,γ)Ba* to reactions of the type Ba(n,p)Cs or Ba(n,α)Xe which can be distinguished in a way based on the light output in the crystal.

Charged particles are rejected using the TOF method as well as two other methods which will be described here. The first method is the use a the polyethylene absorber bar which will stop protons up to 100 MeV for the 40 cm bar. Unlike the neutrons, which do not interact with the plastic scintillator around the detector, the charged particles do and, therefore, an energy cut on the scintillator signal can be made which rejects these events. As in the case with neutrons, the final restriction is the rejection based on the pulse shape information.

B Rejection of Cosmic Rays

Another important background for these measurements is that of cosmic ray muons. The total cosmic ray flux crossing a horizontal area from above is roughly 180 events/(m^2-sec), which for a detector the size of the BaF_2, yields a rate of approximately 5 events/sec. To reduce this background an anticoincidence shield was employed to reduce the rate. The suppression of this background was done during the off–line analysis. An event is accepted when there is no signal above 2.5 MeV in any of the scintillator paddles. The rejection for muons with the anticoincidence shield is greater than 99% and this is most important for the higher energies. Since pileup of a gamma ray with a cosmic ray muon, or a muon on a trajectory which follows a path

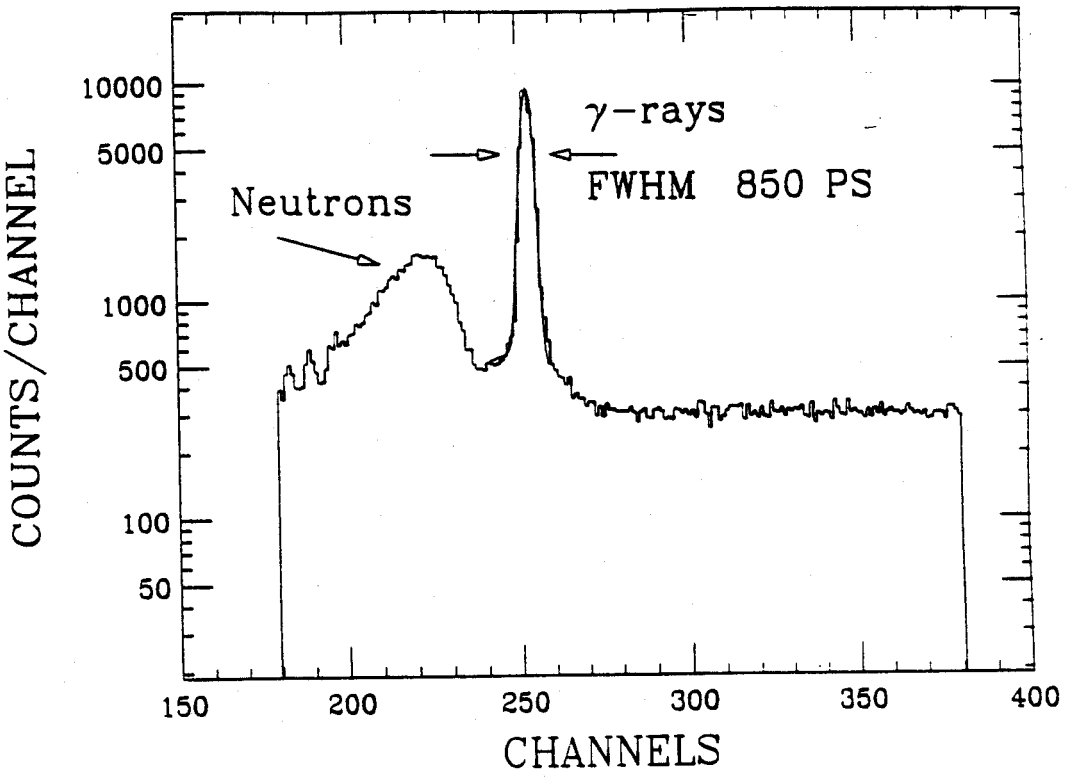

Figure 4.4: Typical one dimensional TOF spectrum obtained with the BaF_2 crystal. The solid curve is a fit of a Gaussian function to the gamma ray peak.

along the axis of the crystal can lead to distortion of the true energy spectrum, they must be eliminated. Figure 4.6 shows the effect the various gates used to suppress the background encountered in these measurements. The final photon spectra were then obtained by combining all of these techniques to eliminate the background from all the known sources:

1. Charged Particles.
2. Fast and Slow Neutrons.
3. Cosmic Ray Muons.

C π^0 Background

Even with implementation of all rejection gates on the gamma ray spectrum, there was still a background which evades the gates. The decay of the neutral pion via the decay, $\pi^0 \rightarrow 2\gamma$ (branching ratio 98%) can be a significant background for incident energies above production threshold. The types of reactions that need to be addressed for neutral pion production were of the following form:

1. p + X(n,p) $\rightarrow$ p + X(n,p) + π^0 or
2. p + X $\rightarrow$ X(n,p+1) + π^0

Ignoring the Fermi momentum in the target nucleus and collective effects. The minimum kinetic energy necessary for the proton to make a pion with a collision of a target with mass M_2 is given by:

$$T = M_{\pi^0}[\frac{2(M_2 + M_p) + M_{\pi^0}}{2M_2}] \tag{4.5}$$

While the incident energies of 145 and 195 MeV protons are above the threshold for all targets, with the exception of deuterium, which has the lowest threshold at 198.7

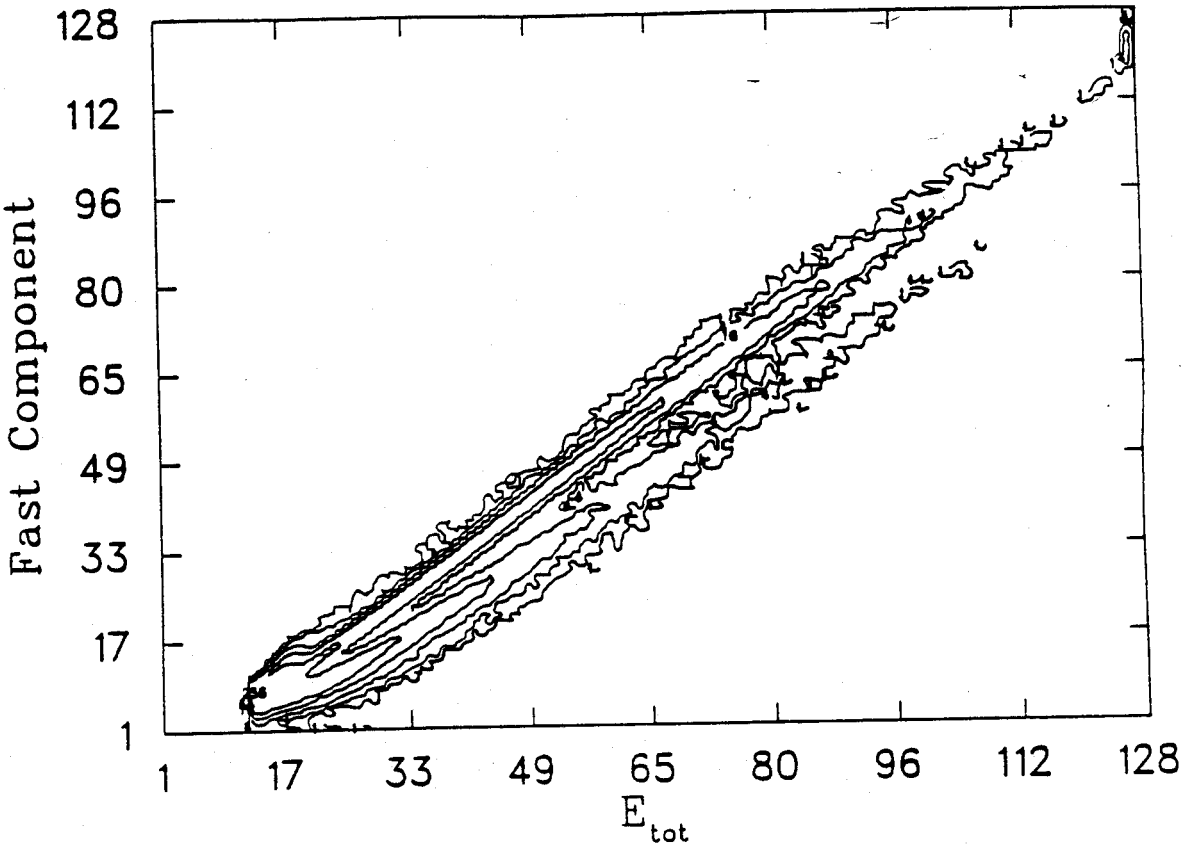

Figure 4.5: Typical PSD spectrum obtained with the BaF_2 crystal. The fast gate is 25 ns while the total energy gate is 1.6 μs.

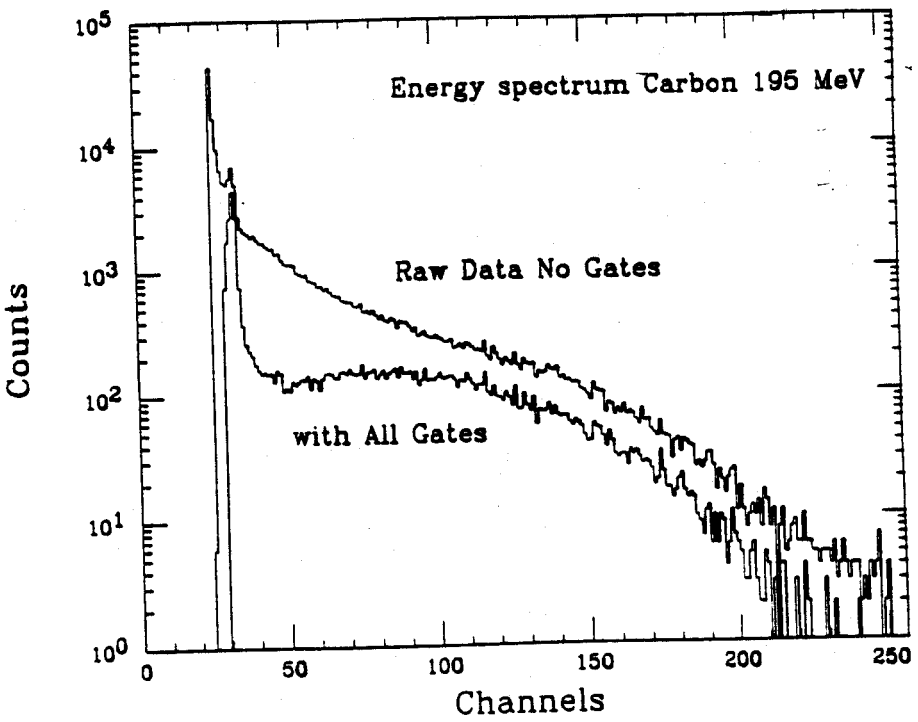

Figure 4.6: A comparison of the measured gamma ray spectra with and without the background suppression gates.

Table 4.1: Tabulated values for π^0 production in proton induced reactions at 200 MeV [Bellini 89].

Target	σ_{π^0} μb
^{12}C	70
^{27}Al	188
^{58}Ni	282
^{89}Y	475
^{118}Sn	533
^{124}Sn	608
^{nat}Pb	769
^{238}U	935

MeV for the reaction p + d $\rightarrow$ ^{3}He + π^0, this channel is only significant for the 195 MeV data for the heavier targets. The data at 195 MeV show an enhancement at half the π^0 mass in the gamma ray spectra. Such an enhancement can clearly be seen in Figure 4.7. An estimate of the background can be made by using the data of X(p,π^0)X from Bellini *et al.* at 200 MeV [Bellini 89]. In Table 4.1 the values reported by Bellini *et al.* are shown, and correspond to approximately a 50% contribution to the total gamma ray cross section for photons above 40 MeV in the nucleon–nucleon center-of-mass frame. The value for the total cross section for gamma rays above 40 MeV was calculated by integrating the energy spectrum at 90° in the laboratory frame and transforming the cross section dσ/dΩ to the nucleon-nucleon center-of-mass frame and multiplying by 4π. Since the angular distribution of the neutral pions is approximately isotropic over the angular range covered in this measurement the bremsstrahlung photon cross section is the difference between the measured gamma ray cross section and the value obtained by Bellini *et al.* [Bellini 89].

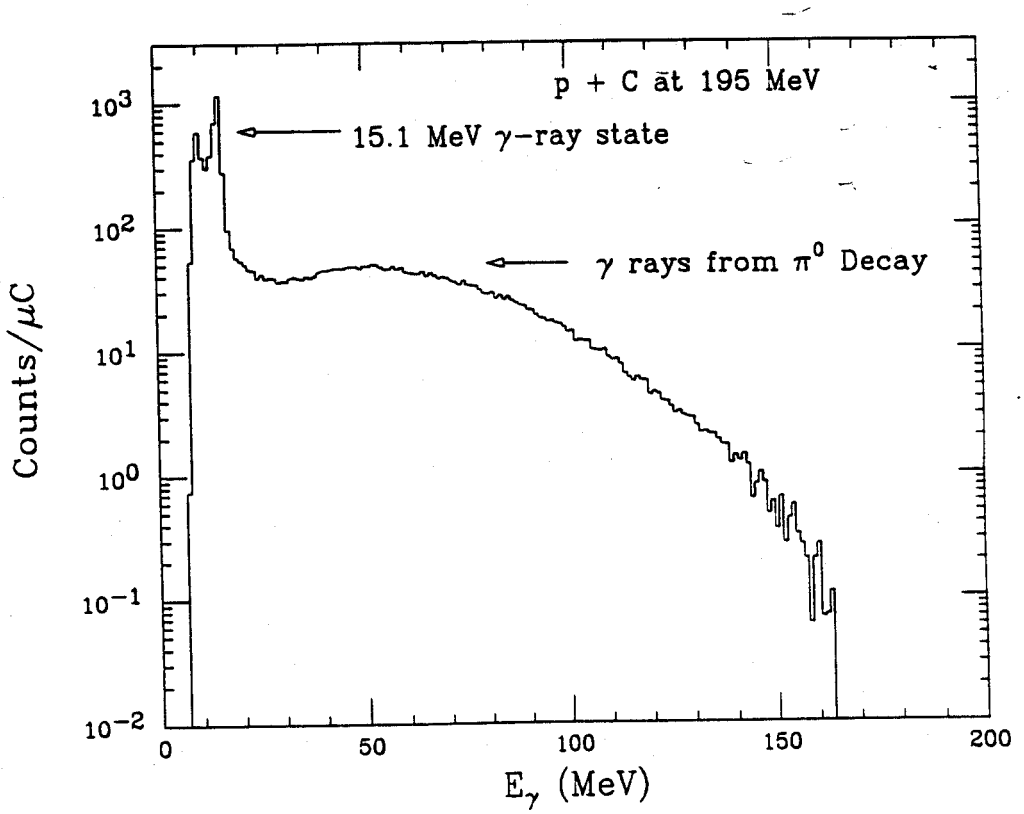

Figure 4.7: A gamma ray energy spectrum at an incident proton energy of 195 MeV. The enhancement at $\approx$ 70 MeV is due to the decay of the π^0.

V Data Analysis and Experimental Results.

With the background suppression gates as previously discussed, the data analysis became a rather simple task. To monitor the fluctuations from run-to-run, every spectrum was checked by integrating the spectrum in several specific energy ranges normalized by the incident beam current. An extra check was also made for the carbon runs and the CD_2 runs by comparing the yield of the 15.1 MeV state normalized by the incident beam current against other runs with the same detector or the other detector which was on the opposite side of the beam. This proved especially useful in finding runs in which the RF time signal shifted by several channels. It also allowed the direct comparison of the two detectors performances, and at 90°, for example, the differences in the 145 MeV data was found to be less than 8% for all targets. The full scale energy was determined by employing the 15.1 MeV gamma ray state from the carbon target, and the 81 MeV peak location for cosmic ray muons passing along the diameter of the crystal. With the energy scale conversion factor determined for both detectors the spectra can now be rescaled and then added or subtracted, as in the case of the CD_2 target.

A Photon Energy Spectra

As can be seen in Figure 4.8 and Figure 4.9, the energy spectra observed at different laboratory angles show a tendency to be "harder" for smaller angles in laboratory. The angular distributions in the laboratory frame for photons above 40 MeV are typically forward peaked. The ratio of the energy integrated cross section at $\sigma(60°)/\sigma(120°)$ at 145 MeV for carbon, zinc and lead are 2.3, 1.6 and 1.7 respectively. This type of behavior can be an indication of photon emission from a moving source. The relationship between a spectrum at an angle θ' in a moving source with a velocity β

relative to the laboratory frame is given by the following expressions:

$$\begin{aligned} E'_\gamma &= E_\gamma^{lab} \cdot \gamma[1 - \beta\cos(\theta_{lab})] \\ \text{where } \gamma &= \frac{1}{(1-\beta^2)^{\frac{1}{2}}} \end{aligned} \tag{4.6}$$

$$\sin(\theta') = \sin(\theta_{lab}) \cdot \frac{1}{\gamma(1 - \beta\cos(\theta_{lab}))}$$

Quantities that do not vary when transformed from one reference frame to another frame under a Lorentz transformation are called invariants and are quite useful when calculating quantities of interest in nuclear reactions. One such quantity is the invariant cross section which is given by:

$$\frac{1}{E'_\gamma}\frac{d^2\sigma}{dE'_\gamma d\Omega'} = \frac{1}{E_\gamma}\frac{d^2\sigma}{dE_\gamma d\Omega} \tag{4.7}$$

where the relationship between E'_γ at angle θ, in the moving source frame and E_γ^{lab} at angle θ_{lab} are given by the Lorentz transformations defined in Equation 4.7 The velocity of the moving source can be extracted from a two dimensional contour plot of the invariant cross section as a function of a quantity called rapidity and the transverse momentum. The rapidity is a quantity which is often used in high energy physics experiments and is now gaining popularity in nuclear physics as well. The definition for the rapidity is:

$$y = \frac{1}{2}\ln\left(\frac{E + P\cos(\theta)}{E - P\cos(\theta)}\right) \tag{4.8}$$

In the laboratory frame if a particle has a velocity β'' and rapidity y'', when viewed in a frame moving with a velocity β with respect to the laboratory frame, the same particle will have a different velocity β' and rapidity y' which are the velocity and rapidity in this new frame respectively. Rapidity is a preferred quantity because of its additive property. The transformation for the parallel components of the velocity from one frame to another is given by:

$$\beta'' = \frac{\beta + \beta'}{1 + \beta\beta'} \tag{4.9}$$

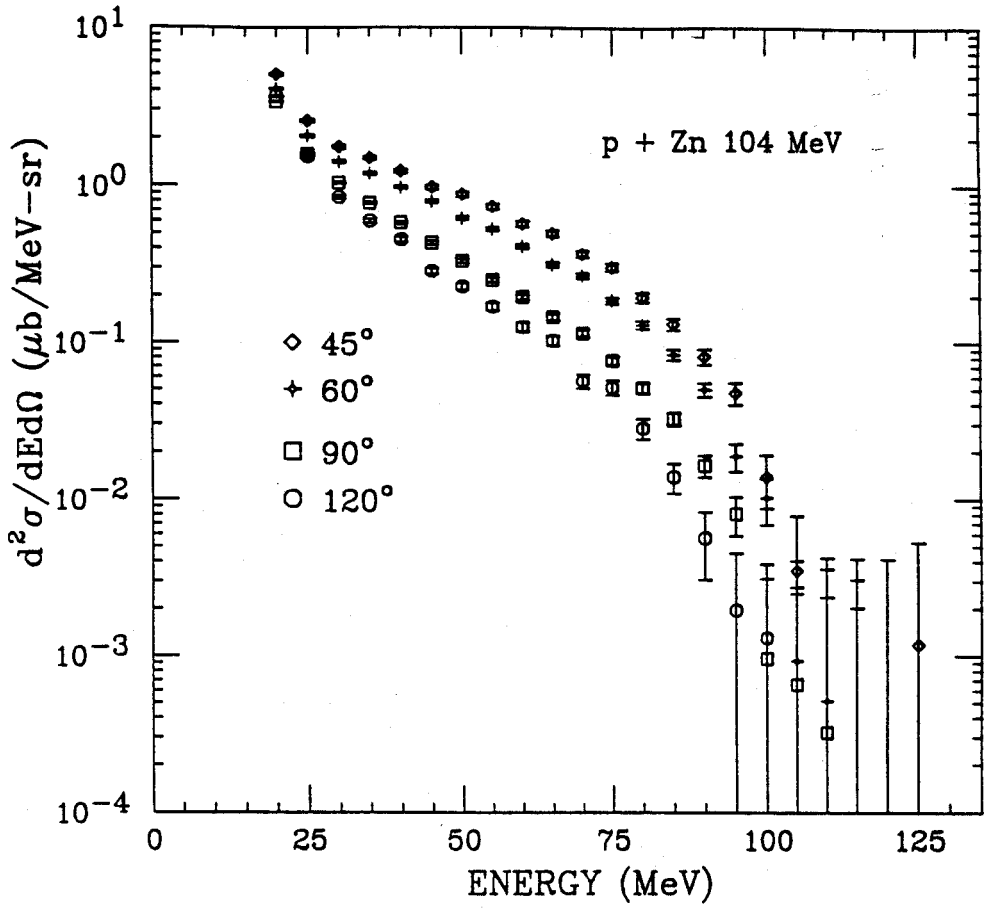

Figure 4.8: Gamma ray energy spectra in the laboratory frame for 104 MeV protons on a zinc target at all of the laboratory angles measured.

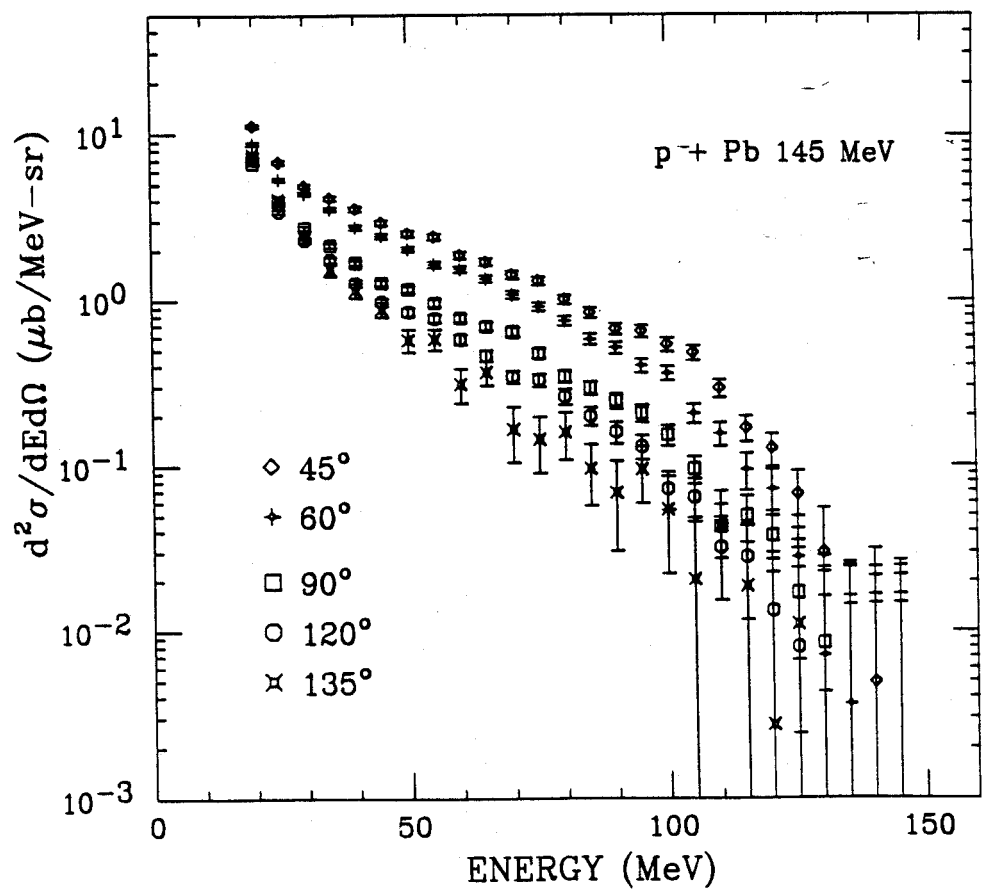

Figure 4.9: Gamma ray energy spectra in the laboratory frame for 145 MeV protons on a lead target at all of the laboratory angles measured.

The proof of the additive property of the rapidity is shown below.

$$y'' = \frac{1}{2}\ln\left(\frac{1+\beta''}{1-\beta''}\right) \tag{4.10}$$

$$y'' = \frac{1}{2}\ln\left(\frac{1+((\beta+\beta')/(1+\beta\beta'))}{1-(\beta+\beta')/(1+\beta\beta'))}\right)$$

$$y'' = \frac{1}{2}\ln\left(\frac{(1+\beta)}{(1-\beta)}\cdot\frac{(1+\beta')}{(1-\beta')}\right)$$

$$\text{therefore } y'' = y + y' \tag{4.11}$$

Figure 4.10 is a typical example of a contour plot of the photon invariant cross section versus the rapidity and the transverse momentum ($P_\perp = E_\gamma \sin(\theta)$) for the reaction p + Pb at 104 and 145 MeV, which is one of the systems studied. The distribution is nearly symmetric about a point centered at the nucleon-nucleon rapidity. In the case of isotropic emission from the source frame, the curves would be circles centered on the the source rapidity. However, if one looks carefully at the higher energy cuts, the centroid becomes lower than the nucleon-nucleon rapidity, which indicates emission from a source moving slower than the nucleon-nucleon center-of-mass. This can be explained by the fact that the highest energy gamma rays come from collisions of the incident proton with a target neutron which has its Fermi momentum pointing in an orientation opposite to the beam direction. In such a collision the source velocity is no longer the nucleon-nucleon center-of-mass velocity, but something less. Table 4.2 presents the best fit source velocity from the rapidity plot, and all the data points show the same trend that at the highest energy the gamma ray source is slower than the nucleon-nucleon frame. A second order polynomial was used to fit the rapidity distribution and the centroid is determined from the first derivative of the best-fit polynomial. If the photon emission were isotropic in the moving frame the predicted shape of the rapidity distribution would be circles centered on the moving source rapidity.

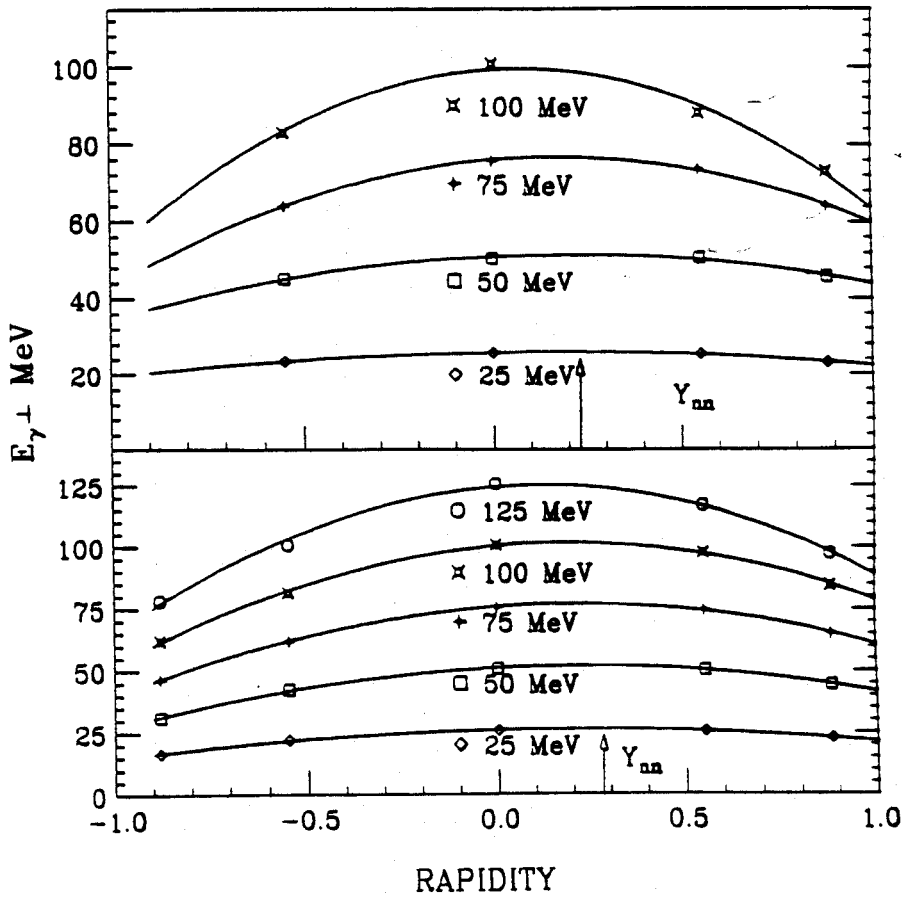

Figure 4.10: Rapidity distributions for 145 (lower frame) and 104 MeV (upper frame) protons incident on a lead target.

Table 4.2: Source velocities extracted from the rapidity distribution plots

E_p = 104 MeV β_{nn} = 0.23				
Target	E_γ=25 MeV β	E_γ=50 MeV β	E_γ=75 MeV β	
Carbon	0.15	0.18	0.15	
Zinc	0.15	0.20	0.18	
Lead	0.14	0.19	0.17	
Mean Value	0.15	0.19	0.17	
E_p = 104 MeV β_{nn} = 0.27				
Target	E_γ=25 MeV	E_γ=50 MeV	E_γ=75 MeV	E_γ=100 MeV
Carbon	0.22	0.21	0.21	0.19
Zinc	0.14	0.23	0.22	0.22
Lead	0.21	0.25	0.25	0.23
Mean Value	0.19	0.23	0.23	0.21

B Extraction of the Deuterium Cross Section

The extraction of the bremsstrahlung cross section from the CD_2 target was made quite simple by the fact that carbon has an excited state at 15.1 MeV which decays to the ground state by gamma ray emission. This discrete gamma ray state can be easily identified in the measured gamma ray spectra. This fact is clearly evident in Figure 4.11 for the carbon target in the lower frame and in the upper frame for the CD_2 target. The procedure is then to find the proper normalization between the two runs at each of the measured angles and then subtract the properly normalized carbon spectra from the CD_2 spectra. Since the yield of 15.1 MeV gamma rays from carbon is given by:

$$Y = \sigma_{15.1} \cdot N_p \cdot (\frac{N_A \rho t \Delta\Omega}{A}) \tag{4.12}$$

where σ is the cross section for the 15.1 MeV state, N_p and N_A are the number of protons incident on the target and A is Avagadro's number, ρt is the target thickness in units of mg/cm^2, and $\Delta\Omega$ is the solid angle covered by the detector. Therefore, the normalization factor is given by the ratio of the yield the 15.1 MeV gamma rays

Table 4.3: Ratio of the number of carbon nuclei in the CD_2 target to that in the carbon foil. The value has been calculated by fitting the yield of 15.1 MeV gamma rays from ^{12}C. A comparison is also made to an empirical value based on the beam current and the relative target thicknesses.

145 MeV			
θ deg	R_{data}	R_{emp}	Difference %
45	0.66	0.78	18
60	2.1	1.60	30
90	1.53	1.30	18
120	1.74	1.61	8
135	1.30	1.20	8
195 MeV			
θ deg	R_{data}	R_{emp}	Difference %
45	0.75	0.96	-28
60	1.01	0.97	4
90	1.35	1.45	-7
120	1.74	1.61	8
135	1.19	1.28	-8

with the CD_2 target to that with the carbon target. Empirically, this ratio R is given by:

$$R = \frac{N_{p_1}\rho_1 t_1 A_2}{N_{p_2}\rho_2 t_2 A_1} \tag{4.13}$$

and experimentally the value is derived from fits to the 15.1 MeV peak for both the CD_2 target spectra and the carbon spectra. A smooth polynomial background was assumed for both spectra. The results for the ratio of the yields found by both the empirical and experimental methods are displayed in Table 4.3. In Figure 4.12 the properly normalized spectra for p + (C,CD_2) 145 MeV are displayed, and it can be clearly seen that the excess in the CD_2 target after the normalization is due to the deuterium in the target. After the subtraction of the spectra, what is left is the bremsstrahlung gamma rays from deuterium. The gamma ray spectrum for p + d at 145 MeV is shown in Figure 4.13, and if one looks carefully at the spectrum near the

end point, a small peak can be identified. This peak is the radiative capture process p + d $\rightarrow {}^3He + \gamma$. The magnitude of this cross section and its location in the spectrum have been verified by comparing the measured data in this work to previous work by M. A. Pikar *et al.* at 150 and 200 MeV [Pikar 87]. In that experiment Pikar *et al.* measured both the ^{3}He and the gamma ray in coincidence. A large lead glass array was used to detect the radiated photon, and a plastic scintillator hodoscope was used for detection of the ^{3}He. The construction of the spectrum of p + d $\rightarrow {}^3He + \gamma$ at 145 MeV was carried out with the reported cross section of Pikar *et al.* at 102.5° in the center-of-mass (90° laboratory) which was then scaled by the ratio of the incident beam energies (to follow the trend that it is decreasing with increasing beam energy). The value of the cross section is then fitted to a Gaussian function in the laboratory frame with the area and centroid determined by the Jacobian of the transformation between the center-of-mass and the laboratory frame for the cross section, and the location of the centroid is given by the Lorentz transformation between the two frames. The Gaussian is then folded with the response function for the BaF_2 detector. The results from this involved procedure are exhibited in Figure 4.13 and the results are quite good. This fact shows the validity of the method of normalization. The full results are tabulated in Table 4.4. The data at 195 MeV do not show the distinct peak at the end point, but the capture cross section is much reduced at this energy. The spectra are then corrected for the capture cross section employing the values from Pikar *et al.* and the procedure described above.

C Dependence on Bombarding Energy

As expected the photon cross section increases with increasing bombarding energy. In Figure 4.14 the energy dependence for this experiment at all bombarding energies is displayed. The data show a smooth increase in the cross section as the incident

Table 4.4: Tabulated values for the radiative capture cross section for the reaction, $p + d \rightarrow {}^3He + \gamma$ at 150 and 200 MeV [Pikar 87].

E_p = 150.3 MeV			
E_γ = 102.1 MeV			
θ_{cm} (deg)	θ_{lab} (deg)	$d\sigma_{cm}/d\Omega$ (nb/sr)	$d\sigma_{cm}/d\Omega$ (nb/sr)
19.9	16.53	132.9 ± 6.6	190.1 ± 9.5
41.8	35.1	183.0 ± 9.2	245.9 ± 12.4
63.2	54.0	185.0 ± 20.0	225.2 ± 24.4
83.4	72.9	100.0 ± 7.0	108.1 ± 7.6
102.5	91.8	82.5 ± 4.1	78.81 ± 3.9
120.4	110.7	63.2 ± 3.2	53.7 ± 2.7
137.4	129.6	45.6 ± 2.3	35.2 ± 1.8
153.7	148.5	33.3 ± 1.7	23.9 ± 1.2
E_p = 200.7 MeV			
E_γ = 133.1 MeV			
θ_{cm} (deg)	θ_{lab} (deg)	$d\sigma_{cm}/d\Omega$ (nb/sr)	$d\sigma_{cm}/d\Omega$ (nb/sr)
20.1	16.53	110.4 ± 5.5	166.8 ± 8.3
42.9	35.1	130.0 ± 26.0	182.4 ± 36.5
64.7	54.0	114.6 ± 10.6	143.1 ± 13.2
85.1	72.9	84.1 ± 4.2	91.4 ± 4.6
104.1	91.8	50.3 ± 2.5	47.4 ± 2.4
121.8	110.7	38.6 ± 1.9	31.8 ± 1.6
138.5	129.6	26.1 ± 1.3	19.3 ± 1.0
154.5	148.5	17.6 ± 0.9	12.0 ± 0.6

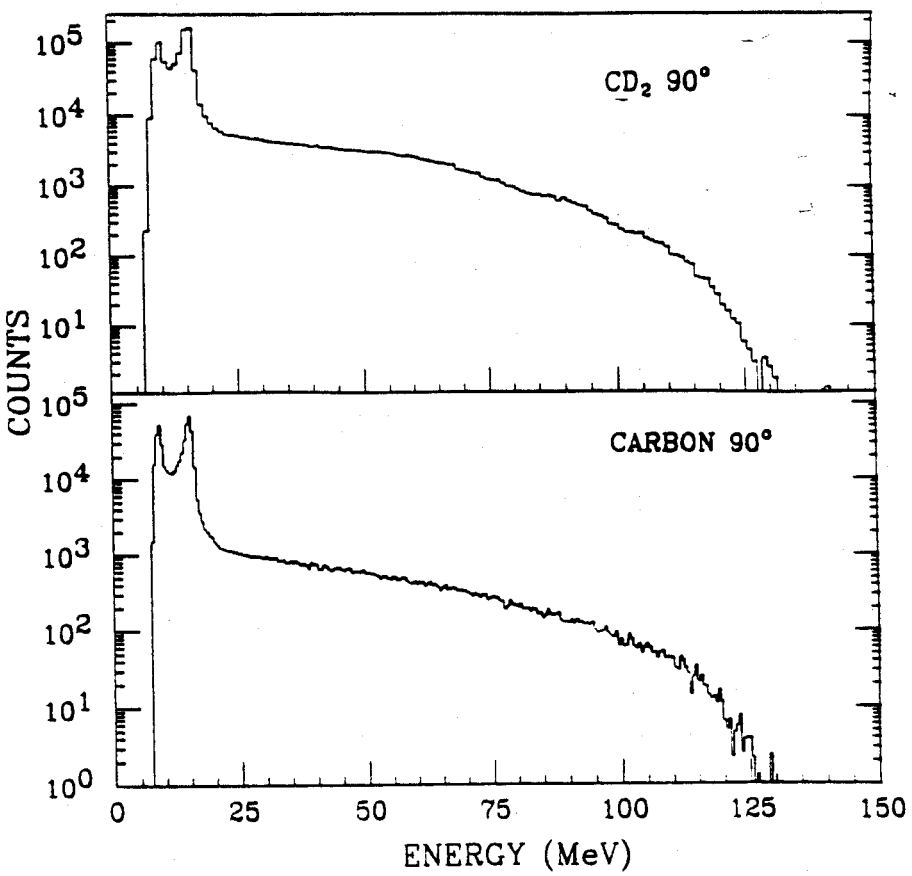

Figure 4.11: Gamma ray energy spectra in the laboratory frame for 145 MeV protons on a carbon target and a CD_2 target at 90 ° in the laboratory. The upper frame is the spectra for the CD_2 target and the lower frame is for the carbon target.

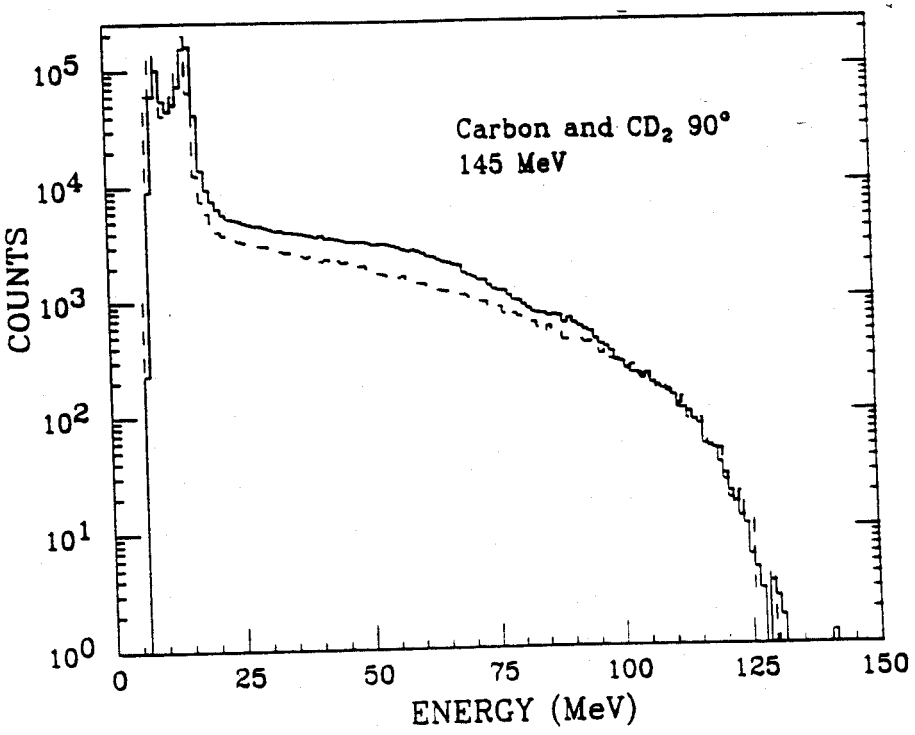

Figure 4.12: A comparison of the normalized carbon and CD_2 gamma ray energy spectra at 90 ° in the laboratory frame. The solid histogram is the CD_2 spectrum and the dashed histogram is the carbon spectrum.

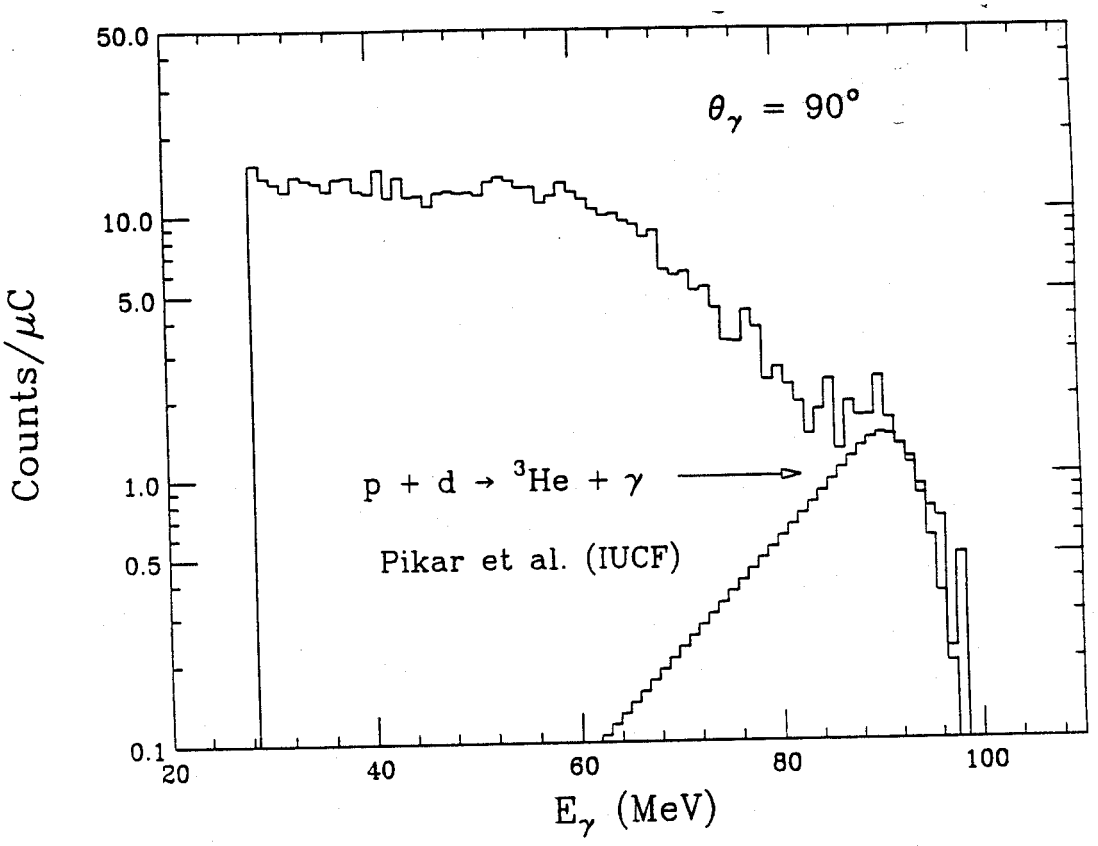

Figure 4.13: A comparison of the measured gamma ray energy spectra at 90 ° in the laboratory frame for the radiative capture process p + d $\rightarrow^3 He + \gamma$ to the folded data from Pikar *et al.* [Pikar 87].

energy is elevated. This can be explained quite simply in the framework of incoherent neutron–proton bremsstrahlung as arising from the increase in the total energy deposited in the colliding system. This is supported by the data, since the energy spectra show an increase in the yield at a specific energy bin for the higher bombarding energies as well as a higher endpoint energy. A simple way to compare the energy spectra for different incident proton energies can be made by plotting the double differential cross section versus the ratio, E_γ/E_p, which is the measured gamma ray energy divided by the incident proton energy. A comparison of the energy spectra at 104 and 145 MeV for the targets of carbon, zinc, and lead at 90° in the laboratory. are displayed in Figure 4.15. It can be seen from Figure 4.15 that there is reasonable agreement between the various data sets, but that there are slight differences near the endpoint. In Figure 4.16 the cross section for deuterium at 145 and 195 MeV are also presented. The most striking feature of the p + d spectra at 145 and 195 is the fact that the spectra are flat until the end point energy is reached where there is a sharp fall off. This may be attributed to energy conservation and the lack of final state phase space available for the scattered nucleons after the collision due to Pauli blocking. The flattening of the gamma ray spectra was predicted by the npγ calculations of Brown and Franklin [Brown 73]. It was predicted in that work that meson-exchange contributions would increase the cross section by roughly a factor of 2 and dramatically alter the angular distribution of the emitted photons. Although these predictions on npγ have never been verified experimentally, calculations that have followed the methods of Brown and Franklin have done a reasonable job at predicting heavy-ion results [Neuhauser 87,Nakayama 89b].

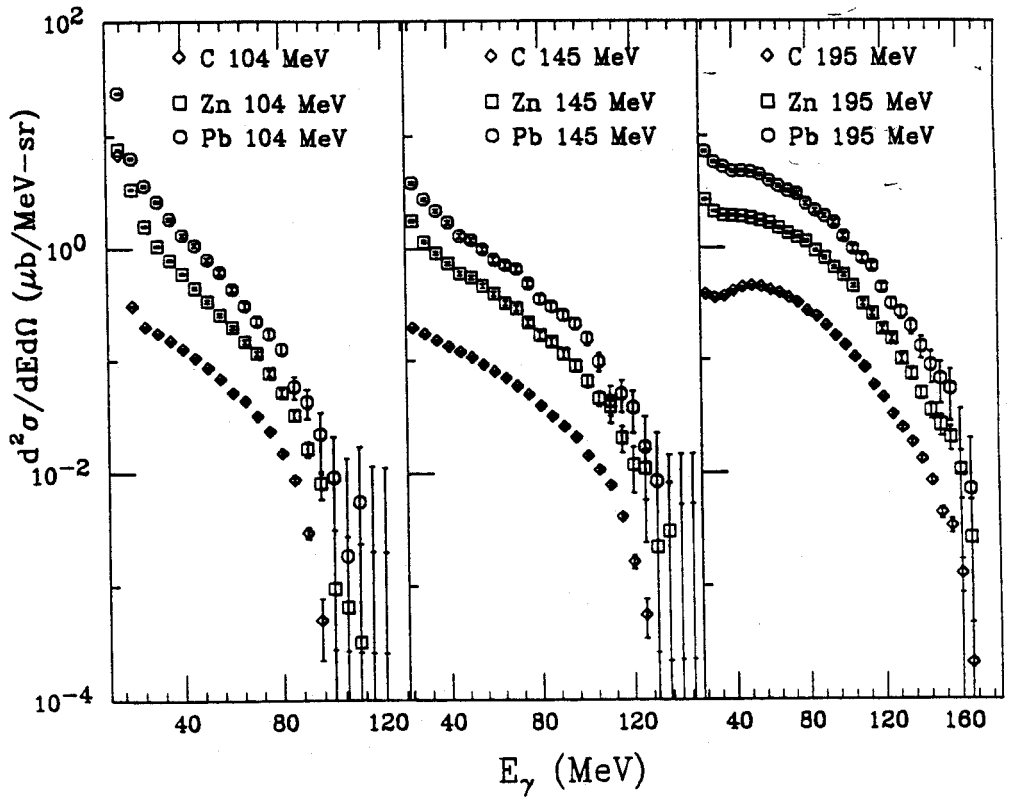

Figure 4.14: Energy spectra for the carbon, zinc and lead targets at 90° in the laboratory, for incident beam energies 104, 145 and 195 MeV.

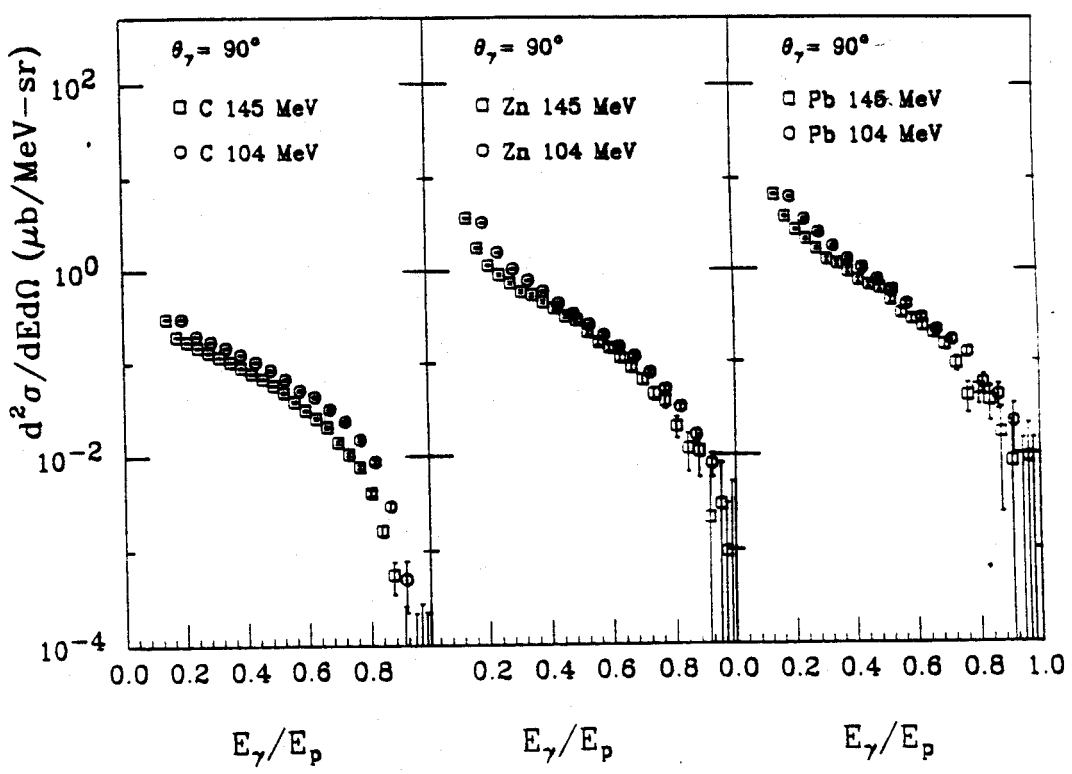

Figure 4.15: A comparison of the energy spectra for carbon, zinc and lead targets at at 104 and 145 MeV versus a reduced variable, E_γ/E_p, which is the measured gamma ray energy divided by the incident proton energy.

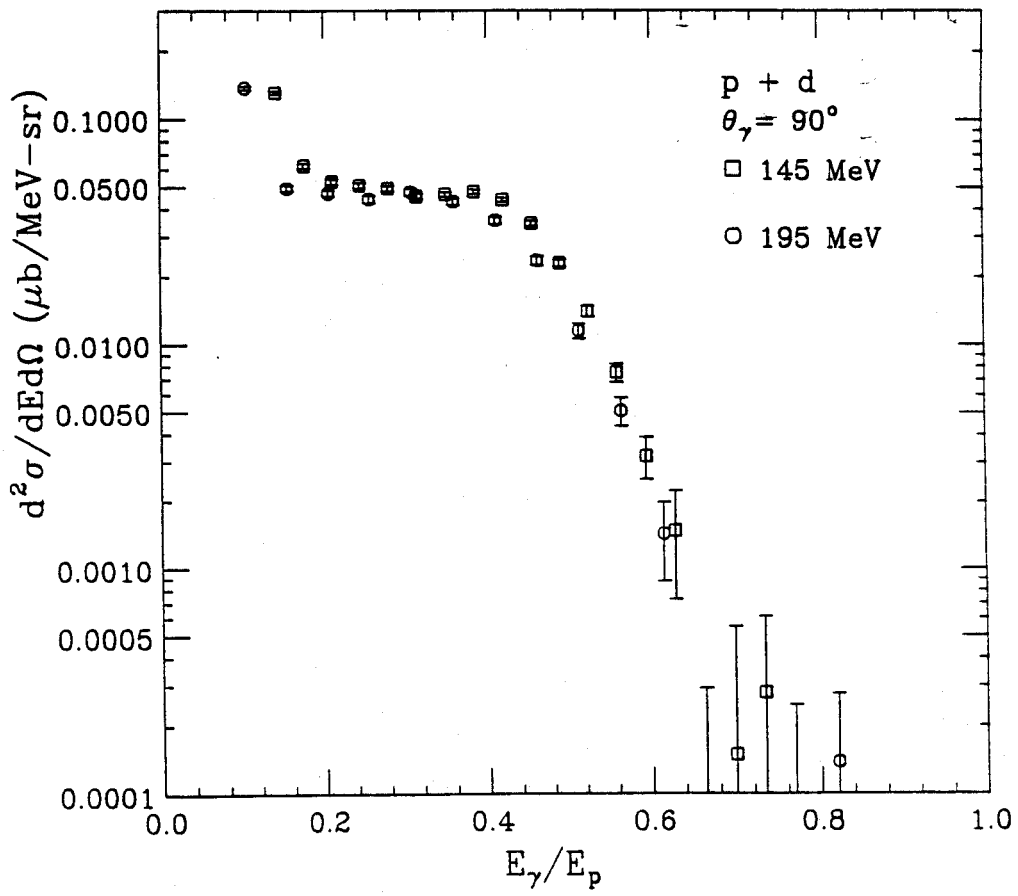

Figure 4.16: A comparison of the energy spectra for gamma rays from the reaction p + d at incident energies of 145 and 195 MeV. The plot is the double differential cross section versus a reduced variable, E_γ/E_p, which is the measured gamma ray energy divided by the incident proton energy.

D Mass Dependence of the Gamma Ray Intensity

The increase in the yield of high energy gamma rays with increasing target mass is expected since there is an increase in the number of neutron-proton collisions. A simple empirical scaling $(A_p A_t)^{2/3}$ has been used for high energy gamma ray data from heavy-ion collisions. If this simple expression is modified to reflect the ratio of the number of neutrons to the total number of nucleons in the target, the scaling factor becomes $(A - Z)/A^{1/3}$. In Figure 4.17 the data for the three incident proton energies and various targets are displayed, and there is a smooth increase in the cross section as a function of the variable $(A - Z)/A^{1/3}$.

E First Collision Neutron–Proton Bremsstrahlung Model

Since the energy spectra are not the simple exponential form encountered with high energy gamma ray data from heavy-ion reactions, a new treatment is required. The function that is to be used must also have a cutoff above the maximum allowed gamma ray energy. One treatment of this problem is discussed in a paper by Nakayama and Bertsch [Nakayama 86]. This paper was previously mentioned in connection with heavy-ion bremsstrahlung gamma ray data. Although Nakayama and Bertsch were not able to fit the absolute magnitude of the heavy-ion data, they did a reasonable job of predicting the shape. A section of this paper dealt with collisional bremsstrahlung in proton induced reactions. Only collisions between neutrons and protons were considered and the approximation that the incident proton was moving through infinite nuclear matter was also made. Energy conservation and Pauli Blocking effects were taken into account in the calculation. The elementary cross section for photon production is assumed to be the semi–classical cross section. The bremsstrahlung rate is

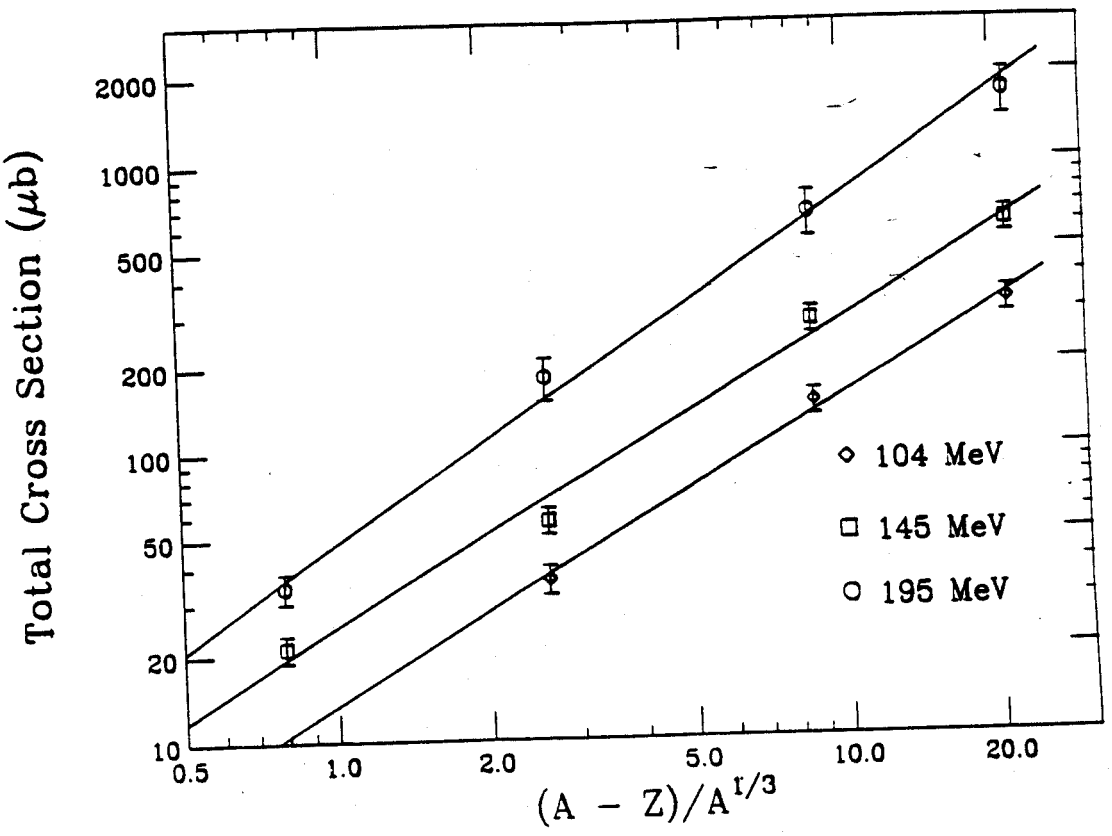

Figure 4.17: A comparison of the total cross sections for all the targets used in this measurements at the three incident beam energies 104, 145 and 195 MeV.

given by the second order formula of perturbation theory [Nakayama 86]:

$$dW_{np\gamma} = 2\pi \left| \langle \Psi_{ij} o \mid \vec{j} \cdot \vec{A} \frac{1}{E_i - H_0} V + V \frac{1}{E_i - H_0} \vec{j} \cdot \vec{A} \mid \Psi_{fj} q \rangle \right|^2 \left(\frac{dn_f dn_q}{dE} \right) \qquad (4.14)$$

The residual interaction between two particles is contained in the potential V. Here Ψ_i and Ψ_f are many-particle states composed of plane wave single-particle wavefunctions. The current density operator is $\vec{j}$ and $\vec{A}$ is the magnetic vector potential. The interaction was assumed to be only a function of the spatial separation between the neutron and proton, independent of the energy and momentum transfer. The residual interaction used was:

$$V = V_0 \, \delta^3(r_p - r_n) \text{ where } V_0 = 50 \text{ MeV} \qquad (4.15)$$

Momentum conservation reduced the sum over the intermediate states j to a single term in the plane wave representation. Denoting the subscripts 1 and 2 to be the energy, ϵ, (or momentum, $\vec{p}$) of the initial proton and neutron and subscripts 3 and 4 to be that of the final proton and neutron, the following equation is derived:

$$\frac{d^2W}{d\omega d\Omega} = \frac{\alpha V_0^2}{2\pi\omega} g \int_{<k_F} \frac{d^3p_2}{(2\pi)^3} \cdot I \qquad (4.16)$$

$$I = \int \frac{d^3p_3}{(2\pi)^3} Q \, \delta(\epsilon_1 + \epsilon_2 - \epsilon_3 - \epsilon_4 - \omega) \cdot S$$

$$S = \sum \left| \frac{\hat{\epsilon} \cdot \vec{v_3}}{1 - \vec{k} \cdot \vec{v_3}} - \frac{\hat{\epsilon} \cdot \vec{v_1}}{1 - \vec{k} \cdot \vec{v_1}} \right|^2$$

$$\text{Pauli Operator } Q = \Theta(p_3 - p_F)\Theta(p_4 - p_F)$$

The photon has an energy of $\hbar\omega$ and its direction is given by the wavevector $\vec{k}$. The total neutron–proton collision rate is given by:

$$W_{np} = 2\pi \left| \langle \Psi_i \mid V \mid \Psi_f \rangle \right|^2 \frac{dn_f}{dE} \qquad (4.17)$$

$$= 2\pi V_0^2 \int_{k_F} \frac{d^3P_2}{(2\pi)^3} \int \frac{d^3P_3}{(2\pi)^3} Q \, \delta(\epsilon_1 + \epsilon_2 - \epsilon_3 - \epsilon_4)$$

If the assumption is made that proton–proton collisions are just as likely as neutron–proton collision, the differential cross section for neutron-proton bremsstrahlung is then the ratio of the gamma ray rate to the total collision rate and is:

$$\frac{d^2P_{np\gamma}}{d\omega d\Omega} = \frac{1}{2W_{np}} \cdot \frac{d^2W_{np\gamma}}{d\omega\, d\Omega} \tag{4.18}$$

Since the ratio of the rates is the quantity of interest, the choice of the potential used in the calculation need not be sensitive to the absolute strength of the residual interaction. The predicted angular distribution for these high energy photons was given by:

$$G(\theta) = 0.6\sin^2(\theta) + 0.4 \tag{4.19}$$

This type of normalization was chosen such that the angular distribution would be normalized to 1 at 90°. In an attempt to arrive at some of the more qualitative features of the predicted spectral shape of these high energy gamma rays, Nakayama and Bertsch formulated a simple phenomenological model based on the behavior of the spectra at the extremes of the gamma ray energy. This simple formulation should be the asymptotic behavior for the much more complicated expressions given in Equation 4.17 and Equation 4.18. For low photon energies, the energy dependence is the usual classical bremsstrahlung result namely, $1/E_\gamma$. Near the maximum photon energy, the rate is proportional to the final state phase space available. In the Fermi gas model, the density of states of given particle-hole character varies as the power of the excitation energy. In the case of neutron-proton collisions the final state has a 2-particle 1-hole character, which has a quadratically varying density of states near the Fermi level [Fetter 71]. Therefore, near the endpoint the bremsstrahlung rate will have an energy dependence on E_γ, as $(E_{max} - E)^2$. Nakayama and Bertsch combined the limiting cases of the bremsstrahlung behavior into one function which is given by:

$$\frac{d^2\sigma}{dEd\Omega} \propto G(\theta) \cdot \frac{(E_{max} - E)^2}{E_{max}E} \tag{4.20}$$

This is the general form of function which was used to fit the proton induced data studied in this work. The angular distribution in Equation 4.20 was modified by using Legendre polynomials of both the second and fourth order. This was done to see if there was any quadrupole component in the angular distribution. The modified expression is of the form:

$$\frac{d^2\sigma}{dEd\Omega} = N \times \left(\frac{(E_{max} - E)^{\lambda}}{E_{max}E} \cdot [1 + a_2 P_2(\cos(\theta)) + a_4 P_4(\cos(\theta))] \right) \qquad (4.21)$$

where P_2 and P_4 are Legendre polynomials of the second and fourth order with the strength coefficients a_2 and a_4 respectively. In both Equation 4.20 and Equation 4.21, the maximum energy for the gamma ray was a quantity that needed a careful treatment. It was found that if only the kinematics of the collision were included, the maximum gamma ray energy was not large enough to fit the backward angle data. Therefore, a modification for the calculation of the maximum gamma ray energy was required. This modification necessitated that the Fermi momentum for the target nucleons be accounted for. This addition gave a higher value for the maximum gamma ray energy in the nucleon- nucleon center-of-mass frame. The exact expressions used in this calculation for the maximum gamma ray energy are:

$$\begin{aligned} E_{\gamma\, max} &= \frac{S - (m_p + m_x)^2}{2[(E_1 + E_2) - (P_1 - P_2)\cos(\theta)]} \qquad (4.22) \\ \text{where } S &= (\hat{P}_1 + \hat{P}_2)^2 \\ E_1 &= (T + m_p),\ \vec{P}_1 = \sqrt{T^2 + 2m_n T}\,\hat{z} \\ \text{and } E_2 &= \sqrt{P_2^2 + m_n^2}\ ,\ \vec{P}_2 = -\frac{|\,\vec{P}_1\,| - |\,\vec{P}_F\,|}{2}\,\hat{z} \end{aligned}$$

Included in the expression of the target momentum $\vec{P}_2$ in the nucleon-nucleon center-of-mass frame is the restriction from Pauli blocking which requires that both nucleons be outside of the target Fermi sphere after the scattering occurs.

The Internal Momentum Distribution of the Deuteron

The infinite nuclear matter approximation used for the heavy nuclei studied are not appropriate for such a light system as ^{2}H. Another approach to calculate the internal momentum distribution was required. A simple analytical form of the ^{2}H wave function in coordinate space is given by the Hulthen wave function [DeBenedetti 67]:

$$\Psi(\vec{r}) = \frac{1}{\sqrt{N(r)}}\left(\frac{\exp^{-r/R} - \exp^{-r/\rho}}{r}\right) \tag{4.23}$$

$$\text{where } N(r) = 2\pi\left(R + \rho - (\frac{4R\rho}{R+\rho})\right)$$

The quantity N(r) is the normalization factor and R (4.31) fm is the "radius" of the deuteron, and the experimentally derived quantity ρ is approximately R/7. The wave function goes to zero exponentially for large r. Since it is the momentum space distribution that is the quantity of interest, a Fourier transform of the wave function is made [Tam 89b].

$$\Psi(\vec{k}) = \frac{1}{(2\pi)^{3/2}}\int d^3r\, \psi(\vec{r}) \exp^{-i\vec{k}\cdot\vec{r}} \tag{4.24}$$

$$= \frac{2}{\sqrt{2\pi N(r)}}\left(\frac{1}{k^2 + 1/R^2} - \frac{1}{k^2 + 1/\rho^2}\right)$$

The internal momentum distribution for the deuteron described by Equation 4.25 is shown in Figure 4.18. The mean value of the the momentum distribution was used in the calculation of the maximum gamma ray energy for the deuterium targets. The mean value for $\vec{k}$ found was to be 0.14 fm^{-1} which corresponds to a Fermi momentum of $\approx$ 25 MeV/c.

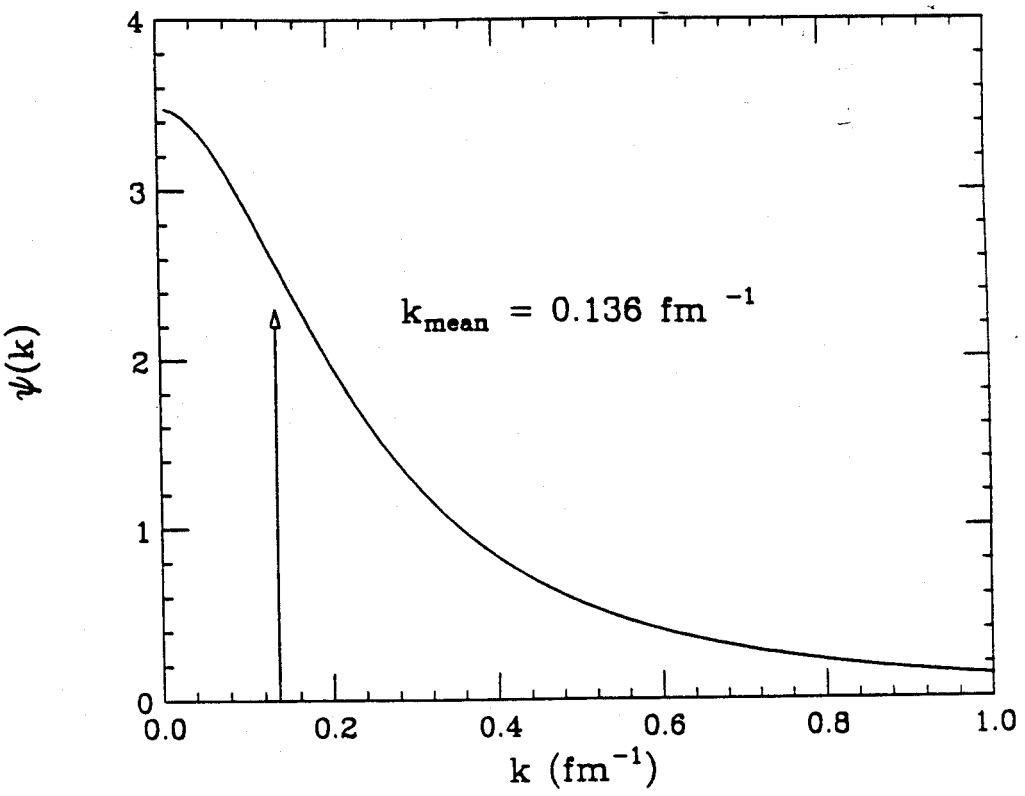

Figure 4.18: The internal momentum distribution for the deuteron which was calculated using the Fourier transform of the Hulthen wave function [DeBenedetti 67].

F Moving Source Fit

To arrive at a more systematic understanding of the experimental data a simple moving source fit to the data was used. This was a necessary to examine many of the more interesting features of the data, such as the strengths of the dipole component and the existence of a quadrupole component. Also with this model a source velocity could be extracted. A global fit to the data at all the measured laboratory angles was done simultaneously for each target using the invariant cross section for the gamma ray energy spectra. The least squares fits to the spectra were performed with the minimization package MINUIT [Minuit]. It should be noted that the response function for the BaF_2 detector was included in the minimization procedure. The fit was folded with the response function prior to the calculation of the χ^2 for each iteration. The functional form used for the least squares fit was the modified function of Nakayama and Bertsch given in Equation 4.21.

The fits for the heavy targets (zinc, lead) included an exponential function for the the statistical component at low gamma ray energies. The best fit parameters were obtained for the overall normalization, the strengths of the Legendre polynomials, and the source velocity β. The exponent in the phase space density portion of the function, λ, was allowed to vary and was found to lie in a region from 0.1 ± 0.01 for the deuterium data to 1.76 ± 0.02 for the lead target. The quality of the fits is displayed in Figure 4.19 for carbon at 145 MeV and for the lead target at 145 MeV in Figure 4.20. Also shown in Figure 4.21 are the fits to the deuterium data at 90° in the laboratory for both the beam energies. This simple parameterization of the gamma energy spectra does a better job fitting the data as the target mass is increased. The values of the reduced χ^2 vary from 10.5 for the carbon targets to 1.3 for the lead target. A complete listing of all the parameters and the reduced χ^2 is given in

Table 4.5. The statistical significance of the fourth order Legendre polynomial P_4 is not overwhelming in the sense that with the number of free parameters in the fit, the change in the χ^2 by adding this term is not large. A more stringent test on the statistical significance of this term can be done by using the F-test. On the basis of this test, the importance of this term is quite small which indicates that the term in most of the cases should not be added, or the term is just at the fringes of being rejected. Therefore, there is no strong evidence for quadrupole emission in proton induced high energy gamma ray production.

G Angular Dependence

Although a large fraction of the heavy-ion induced reactions have reported mainly isotropic emission in the nucleon–nucleon center–of–mass frame, the existence of a dipole component has been reported in measurements by Grosse *et al.* [Grosse 86], Bertholet *et al.* [Bertholet 87], Tam *et al.* [Tam 88,Tam 89a] and Murakami *et al.* [Murakami 89]. The general trend found in these works was that the dipole component was most pronounced for the lighter systems and also for the lower incident beam energies. The values for the light ion reactions ^{2}H, ^{4}He + C performed by Tam *et al.* [Tam 89a] were consistent with the long wavelength approximation for nonrelativistic neutron–proton bremsstrahlung which takes the form $(1 - \frac{3}{5}\cos^2(\theta))$. The reduction of this value for heavier systems has been attributed to secondary collisions within the overlap region. The change to isotropy for the higher energy collisions (ie. E/A $\geq$ 50 MeV) may be due to the increase of the meson exchange current between the colliding nucleons [Nakayama 89b].

The angular distributions in the nucleon-nucleon center-of-mass system for the carbon zinc and lead targets are shown in Figure 4.22, Figure 4.23 and Figure 4.24 for the 104, 145 and 195 MeV data respectively. The low energy cutoff is 40 MeV

Table 4.5: Best fit values from the modified function from Nakayama and Bertsch [Nakayama 86] which is described in Equation 4.21 for the bremsstrahlung photons in proton induced reactions at 104 and 145 MeV.

N_1 μb/(MeV-sr)	a_2	a_4	λ	β^-	Reduced χ^2 $\chi^2/(N_{free} - \nu)$
Carbon 104 MeV					
17.3 ± 0.6	0.0	0.0	0.90 ± 0.01	0.23 ± 0.4	11.0
17.4 ± 0.7	0.06 ± 0.01	0.0	0.90 ± 0.01	0.23 ± 0.3	10.5
17.6 ± 0.9	-1.3 ± 0.3	-1.5 ± 0.4	0.77 ± 0.01	0.23 ± 0.03	7.95
Zinc 104 MeV					
5.2 ± 0.3	0.0	0.0	1.49 ± 0.02	0.23 ± 0.02	3.84
5.3 ± 0.1	0.30 ± 0.02	0.0	1.51 ± 0.03	0.23 ± 0.03	2.97
4.8 ± 0.4	-1.25 ± 0.25	-1.44 ± 0.2	1.44 ± 0.02	0.23 ± 0.04	2.66
Lead 104 MeV					
8.6 ± 0.7	0.0	0.0	1.58 ± 0.02	0.16 ± 0.01	5.10
9.2 ± 0.2	0.65 ± 0.02	0.0	1.61 ± 0.01	0.16 ± 0.06	2.67
7.0 ± 0.6	-0.47 ± 0.2	-1.0 ± 0.2	1.60 ± 0.02	0.15 ± 0.05	2.53
Deuterium 145 MeV					
131 ± 5	0.0	0.0	0.12 ± 0.01	0.26 ± 0.03	9.4
139 ± 5	-0.3 ± 0.02	0.0	0.10 ± 0.01	0.26 ± 0.03	8.5
130 ± 5	-0.7 ± 0.04	-0.8 ± 0.06	0.10 ± 0.01	0.25 ± 0.04	7.04
Carbon 145 MeV					
4.3 ± 0.2	0.0	0.0	1.09 ± 0.09	0.27 ± 0.05	13.9
4.7 ± 0.4	-0.27 ± 0.01	0.0	1.07 ± 0.08	0.27 ± 0.03	12.10
4.6 ± 0.5	-0.61 ± 0.02	-0.67 ± 0.2	1.06 ± 0.02	0.27 ± 0.04	10.50
Zinc 145 MeV					
2.31 ± 0.05	0.0	0.0	1.61 ± 0.05	0.20 ± 0.05	2.28
3.2 ± 0.4	0.37 ± 0.02	0.0	1.56 ± 0.03	0.27 ± 0.03	2.00
1.9 ± 0.5	-1.63 ± 0.7	-2.3 ± 0.8	1.57 ± 0.02	0.27 ± 0.04	1.99
Lead 145 MeV					
3.06 ± 0.02	0.0	0.0	1.75 ± 0.01	0.27 ± 0.02	1.52
3.0 ± 0.1	0.23 ± 0.02	0.0	1.76 ± 0.02	0.27 ± 0.03	1.32
2.94 ± 0.02	0.18 ± 0.04	-0.06 ± 0.04	1.76 ± 0.02	0.27 ± 0.03	1.32
Deuterium 195 MeV					
181 ± 14	0.0	0.0	0.14 ± 0.02	0.30 ± 0.02	2.17
179 ± 12	-0.3 ± 0.05	0.0	0.13 ± 0.02	0 .30 ± 0.03	2.07
173 ± 13	-0.4 ± 0.06	-0.3 ± 0.1	0.13 ± 0.02	0.30 ± 0.02	2.04

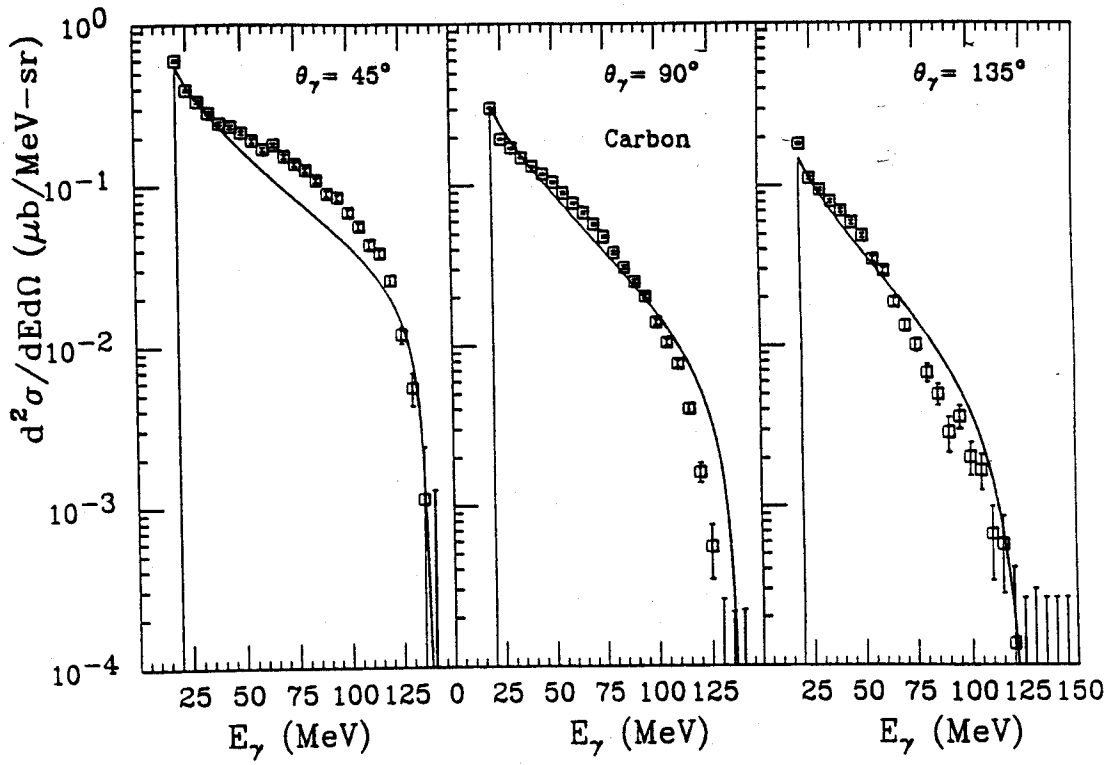

Figure 4.19: A comparison of the energy spectra for the carbon target at 145 MeV and the results of a least squares fit to the data by the function given in Equation 4.21 at 45°, 90°, and 135° in the laboratory.

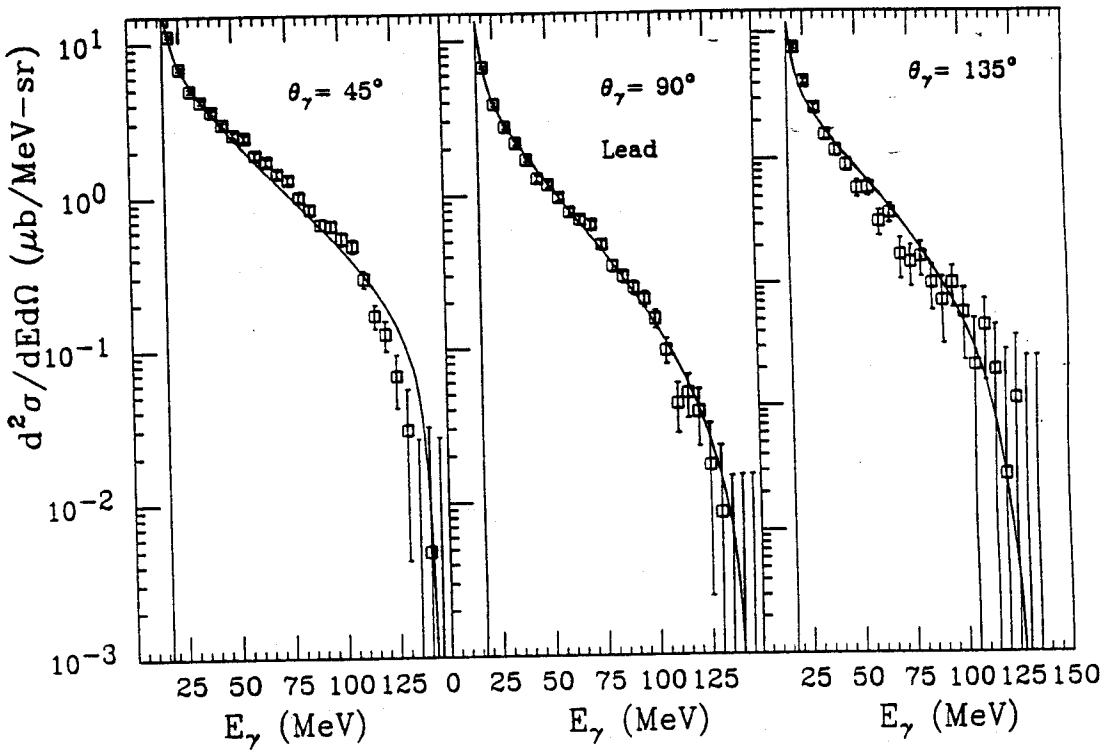

Figure 4.20: A comparison of the energy spectra for the lead target at 145 MeV and the results of a least squares fit to the data by the function given in Equation 4.21 at 45°, 90°, and 135° in the laboratory.

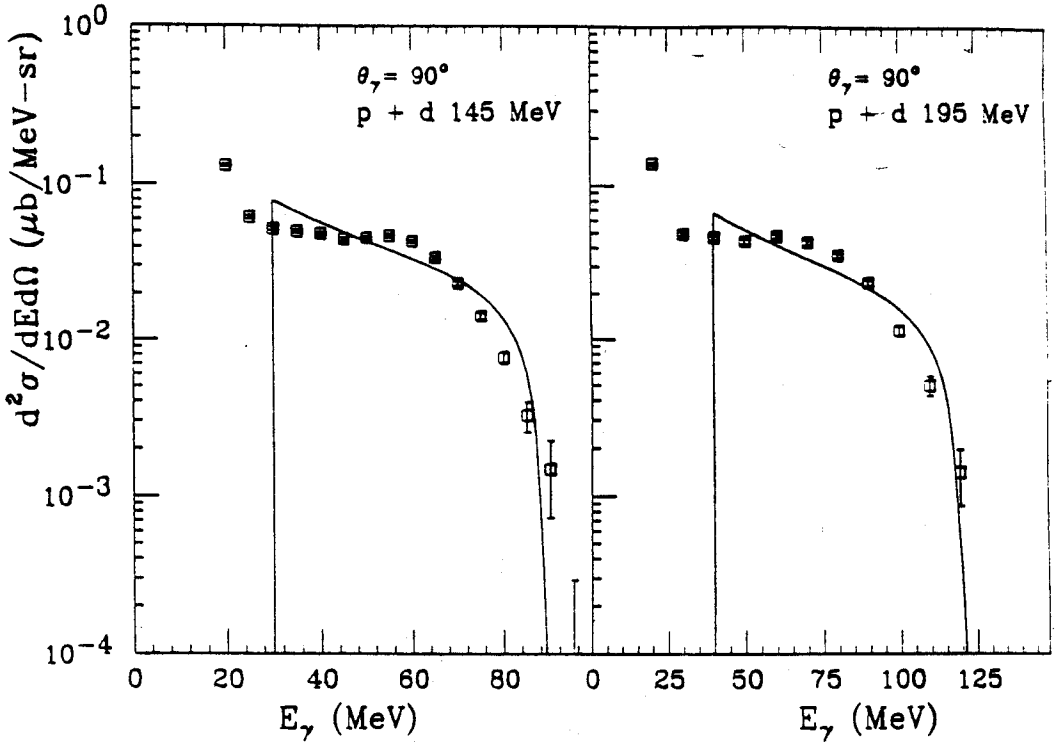

Figure 4.21: A comparison of the energy spectra for the deuterium target at 145 and 195 MeV and the results of a least squares fit to the data by the function given in Equation 4.21 at 90° in the laboratory.

in the nucleon-nucleon center of mass frame. The solid lines are fits to the angular distribution of isotropic plus dipole terms. The spectra show a trend toward becoming more isotropic in the nucleon–nucleon frame as the target mass is increased with the strongest anisotropy for the deuterium target. The angular distributions for the deuterium target at 145 and 195 MeV are displayed in Figure 4.25. The cross section $d\sigma/d\Omega$ for the deuterium has a forward backward ratio of approximately 3. The same ratio for the carbon is roughly 1.8. The angular distribution for the deuterium target exhibits an isotropic plus $\cos(\theta_{cm})$ distribution. This type of an angular distribution is due to the asymmetry of the collision. In heavy-ion reactions one averages over neutrons from the target interacting with protons from the projectile and also protons from the target interacting with neutrons from the projectile which leads to symmetry in the reaction. In this reaction the proton interacts with the target neutron, and the angular distribution should reflect this fact. The fits for all the data show reasonable agreement which indicates again that there is no statistically significant quadrupole emission in the measured gamma ray angular distribution.

VI Polarization Information

Recent work by Nakayama [Nakayama 89a] made predictions with regard to the spin dependence of high energy gamma ray production using the T matrix to calculate the photon production cross section in neutron–proton collisions. The idea was that if any spin dependence in gamma ray production would be apparent without having both the target and incident particle polarized, it might be in the region of the spectra with the highest energy gamma rays. This was based on the assumption that the highest energy gamma rays can only come from first collisions.

The simplest of the spin dependent observables is the analyzing power A. Consider

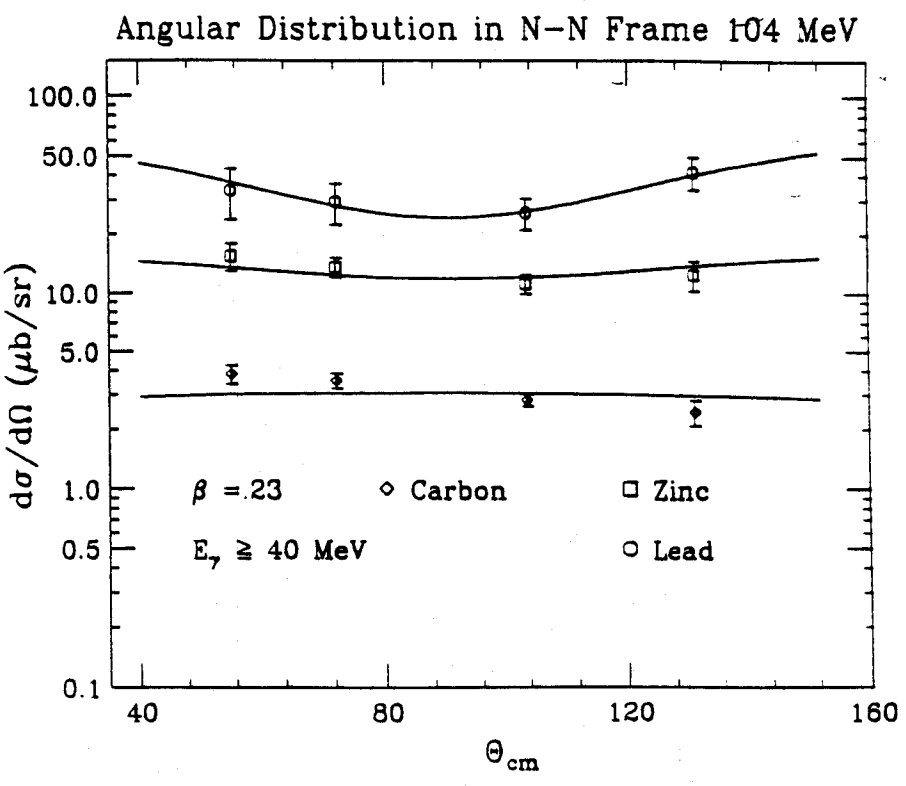

Figure 4.22: The angular distributions at a proton energy of 104 MeV for photons in the nucleon–nucleon center-of-mass with energies greater than 40 MeV in this frame.

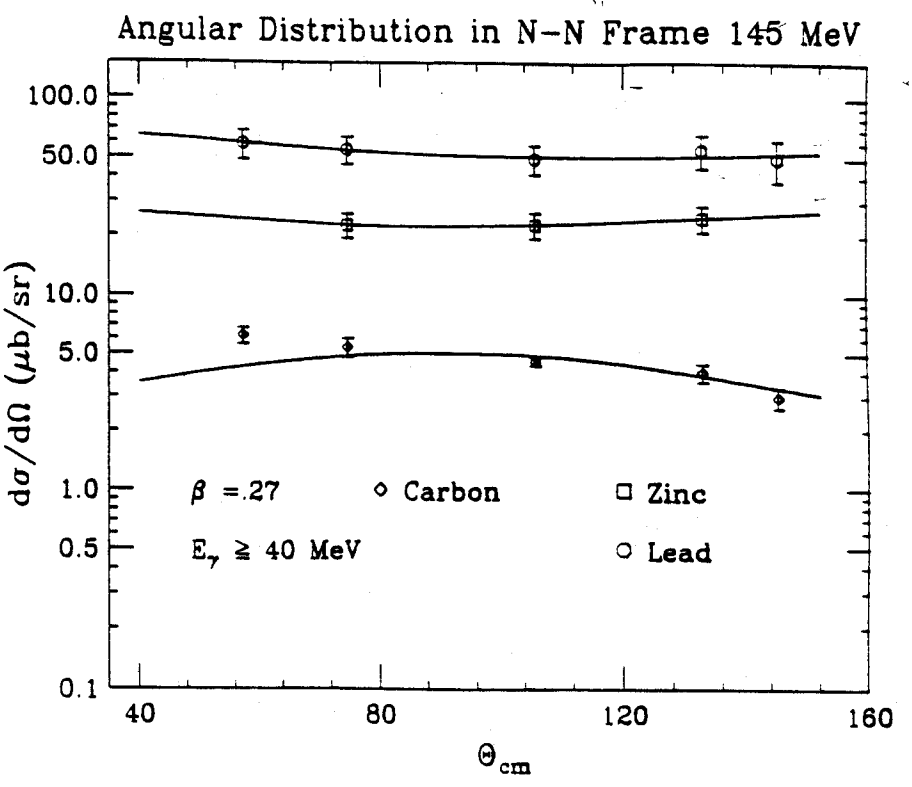

Figure 4.23: The angular distributions at a proton energy of 145 MeV for photons in the nucleon–nucleon center–of–mass with energies greater than 40 MeV in this frame.

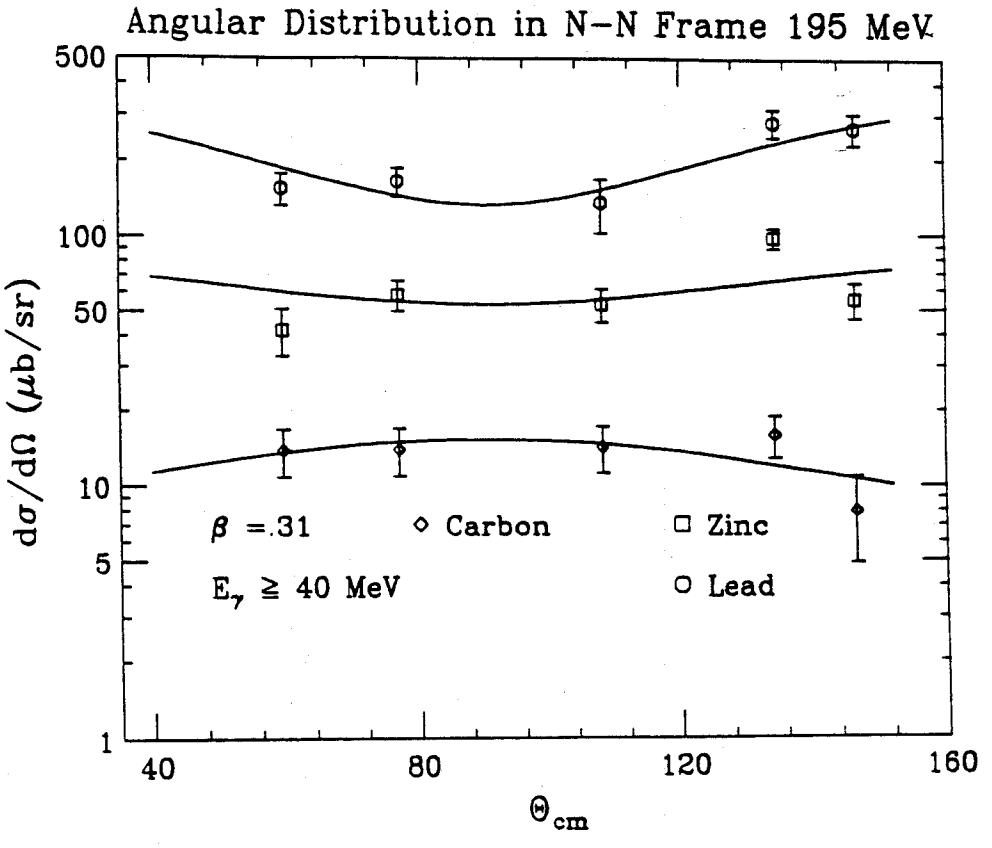

Figure 4.24: The angular distributions at a proton energy of 195 MeV for photons in the nucleon–nucleon center–of–mass with energies greater than 40 MeV in this frame. The values reported have been corrected for gamma rays arising from π^0 decay.

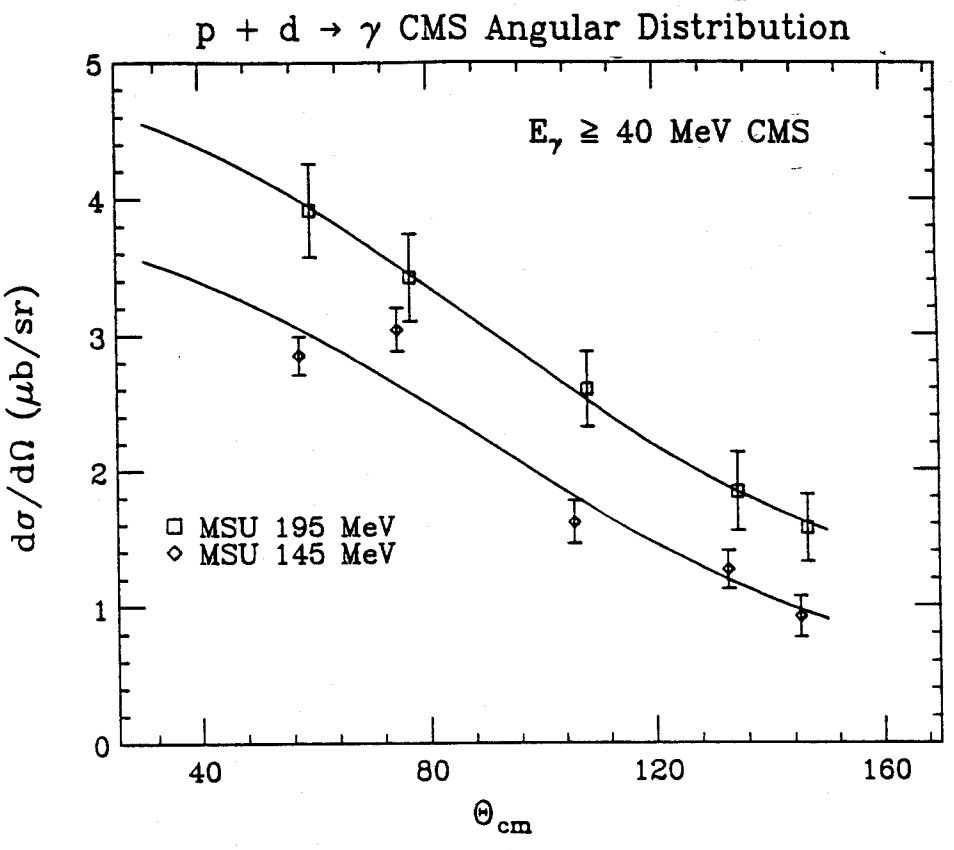

Figure 4.25: The angular distributions of photons from deuterium at proton energies of 145 and 195 MeV in the nucleon–nucleon center–of–mass. The lower limit for the cross section is 40 MeV in this frame.

the elastic scattering of a spin 1/2 particle from a spin 0 target if N_l and N_r denote the fraction of events in which the particle scatters at an angle θ to the left or right, then the analyzing power is defined by:

$$A = \frac{1}{P_b}\left(\frac{N_l - N_r}{N_l + N_r}\right) \tag{4.25}$$

where P_b is the average polarization of the incident beam. One should note that A is a function of the angle θ and the particle's momentum. To measure A in this manner would require two detectors or spectrometers. However, the same quantity A can be obtained by using one detector or spectrometer at an angle θ, and instead reversing the incident beam polarization. Then the asymmetry will be given by:

$$A = \frac{1}{P_b}\left(\frac{N_+ - N_-}{N_+ + N_-}\right) \tag{4.26}$$

where N_+ and N_- are the fractions of events with beam polarization either up or down.

A Experimental Results

Using the definition given by Equation 4.26, the analyzing power for the gamma rays when the proton beam was spin up or spin down was calculated . Since the statistics were low, the data had to be binned into coarser units of energy before any meaningful comparison could be made. Polarization information was recorded for all beam energies and all targets. However, the deuterium data was not used since the statistics are very poor. The polarization of the beam was checked several times during the experiment and was found to be roughly 80% polarized for all the runs. The results for the protons at a bombarding energy of 104 MeV for the carbon target and lead are shown in Figure 4.26. It can be clearly seen that within the uncertainty of the measurement that there is no clear signature of any polarization effects in the gamma ray spectra. Results for the lead and carbon targets at 145

MeV are shown in Figure 4.27. Again, there is no unambiguous sign of any spin information in the high energy gamma ray spectra. However, this is not the case for the data at 195 MeV. This bombarding energy, as previously mentioned, is well above the production threshold for π^0, and Figure 4.28 clearly shows a difference in the spectra for high energy gamma rays with spin up or spin down. The asymmetries for the three targets are displayed in Figure 4.29 and it can be seen that it is roughly constant with increasing target mass. Since the peak the the spectra occurs at nearly half the mass of the π^0, it was thought that the gamma ray from pion decay might still carry information regarding the asymmetry of the neutral pion.

B Monte-Carlo Calculation

In order to check the hypothesis that the nonzero asymmetry was associated with the decay of the π^0 a Monte Carlo program using the spin information and the correct kinematics was prepared. An event tag was placed on the spin of the π^0, and it was allowed to decay with the energy and position determined by a random variable. The shape of the energy spectrum used in the Monte–Carlo was an exponential. This is the shape for pion spectra from heavy-ion data and, although it may not be the actual shape of the π^0 energy spectrum from proton induced reactions, the information extracted will not be affected. The pions were assumed to be emitted isotropically in the nucleon–nucleon center-of-mass frame. The two gamma rays that were emitted in the decay were then transformed into the laboratory frame with the spin information intact. The gamma rays were then histogrammed in discrete energy bins, and the results are shown in Figure 4.30. In Figure 4.30 the decays from neutral pions with spin up have a different peak location than decays from pions with spin down which is exactly the effect that is observed in the data. Therefore, the conclusion is that the strong asymmetry observed in the single photon spectra at 195 MeV is due to

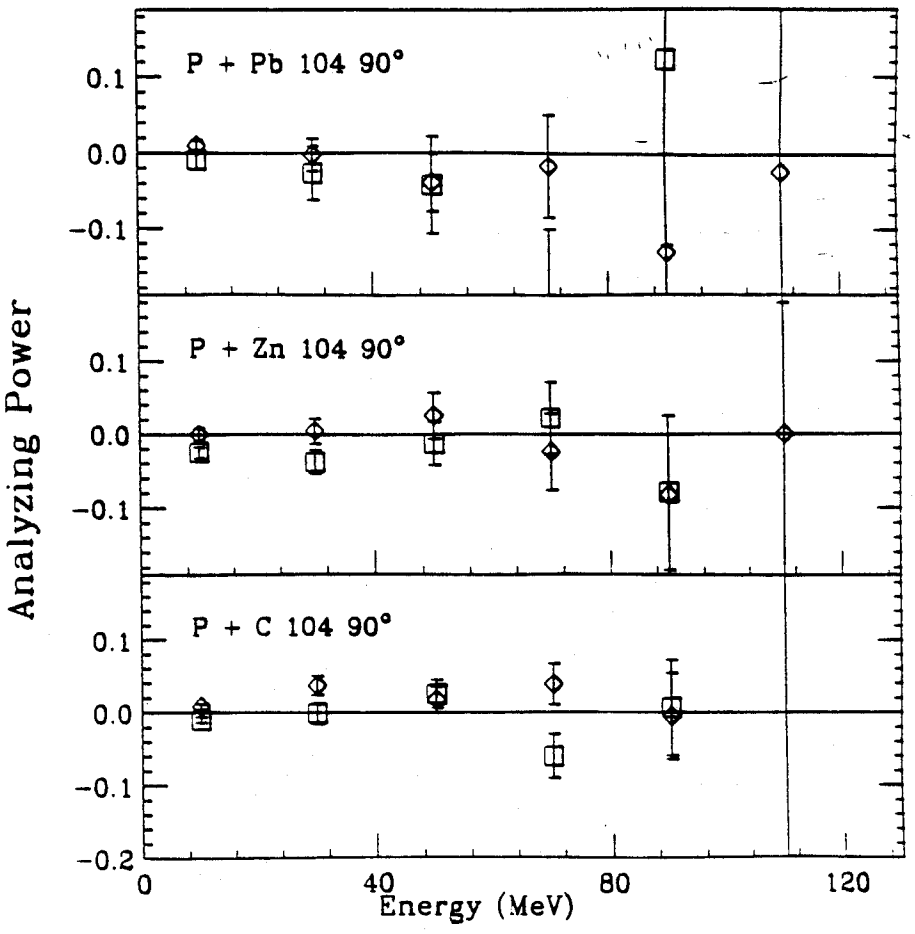

Figure 4.26: The asymmetry for gamma rays from polarized protons at 104 MeV on all the targets at 90° in the laboratory.

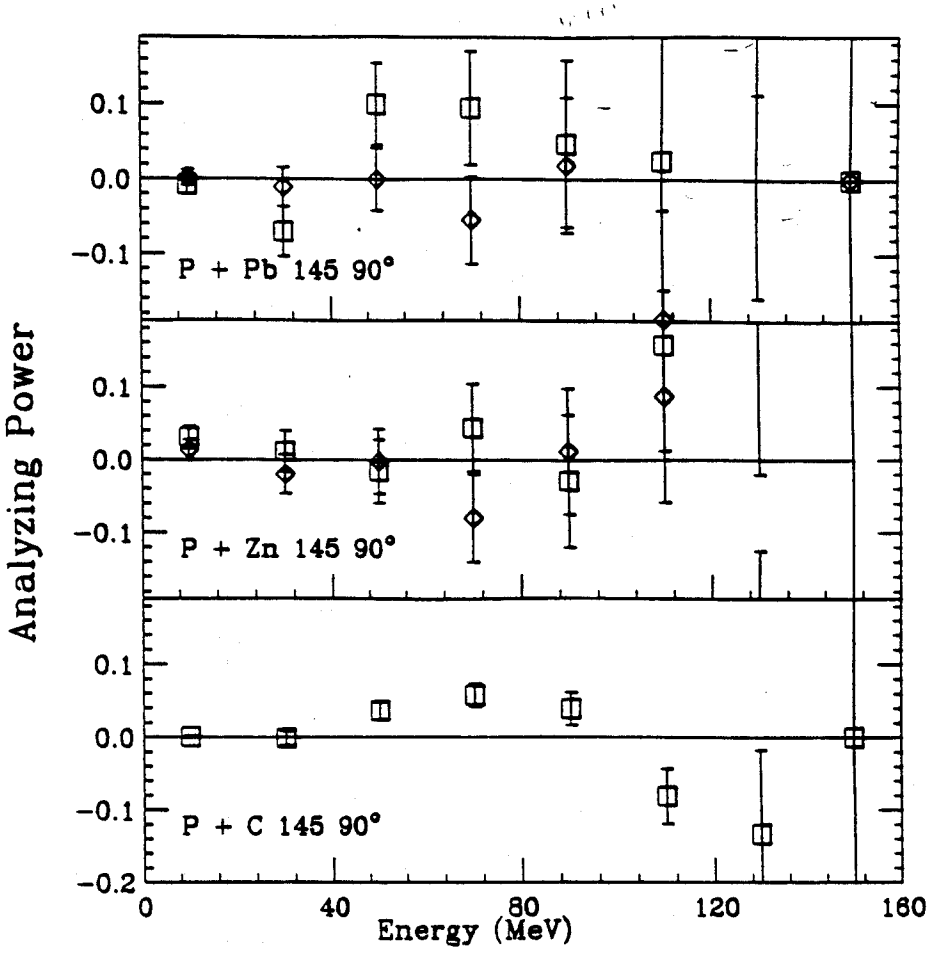

Figure 4.27: The asymmetry for gamma rays from polarized protons at 145 MeV on targets of carbon, zinc and lead at 90° in the laboratory.

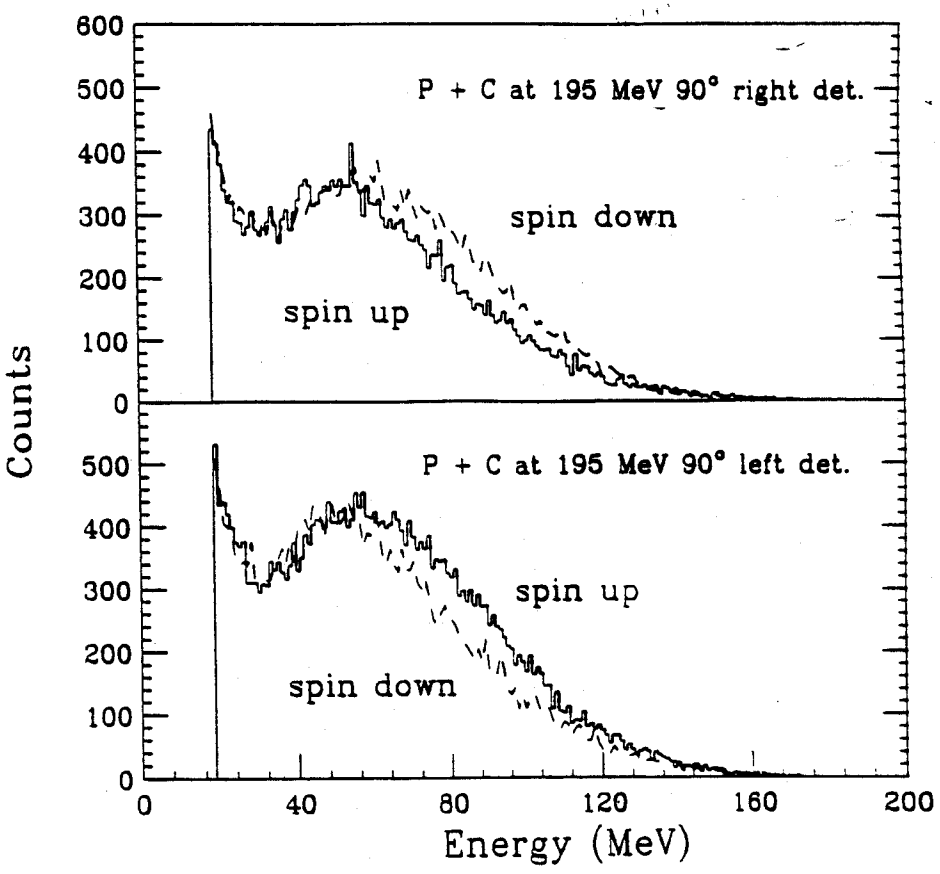

Figure 4.28: The measured gamma ray spectra for polarized protons at 195 MeV incident on a carbon target for both BaF_2 detectors at 90° in the laboratory.

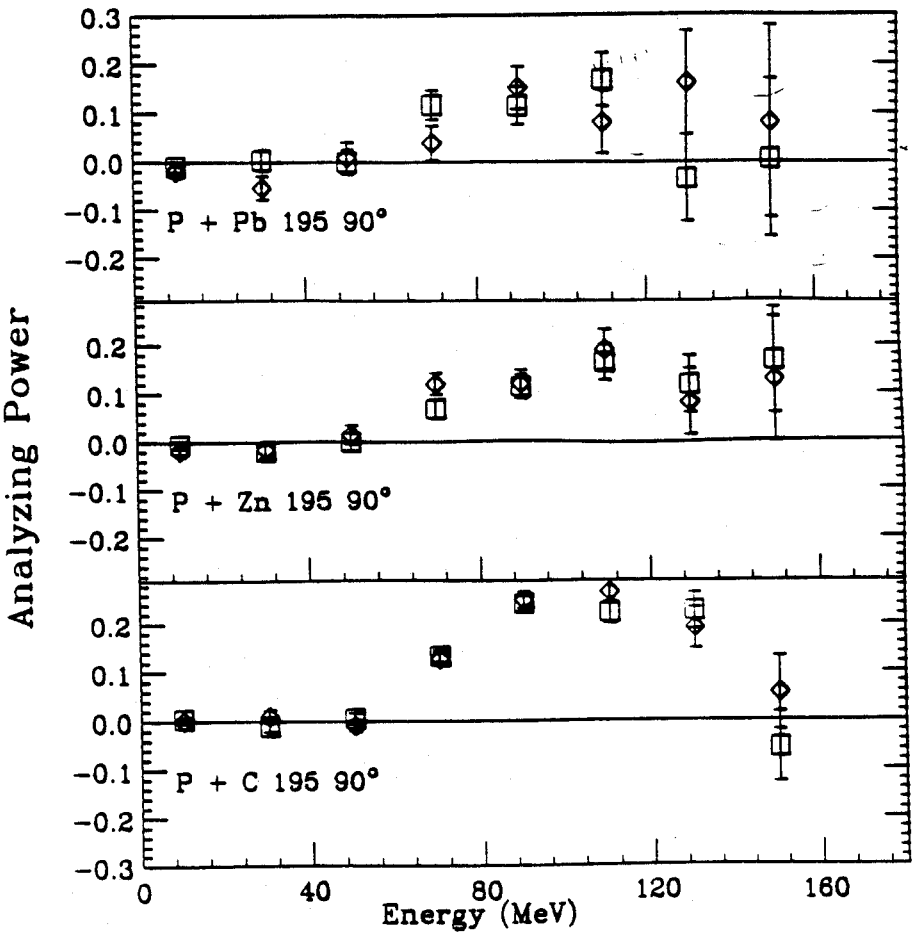

Figure 4.29: The asymmetry for gamma rays from polarized protons at 195 MeV on targets of carbon, zinc and lead at 90° in the laboratory.

asymmetry of the π^0.

VII Conclusions

The energy spectra for proton induced gamma ray production differ from the exponential shape which has been observed in heavy-ion reactions. Qualitatively, the energy spectra can be explained by a simple phenomenological model which takes into account the behavior of the high energy gamma at the energy extremes of the spectrum. The maximum energy gamma ray energy can be derived by a simple calculation which includes the recoil of the target nucleus. However, agreement with the observed endpoint energies at all angles is obtained only when the Fermi momentum of the target nucleons is taken into account. By taking slices through the rapidity distribution one can show that the data support a picture in which the highest energy gamma rays are coming from a proton colliding with a target neutron the momentum of which is pointing in a direction opposite to the incident beam direction. The energy spectra for the deuterium are extremely flat, and this may be due to meson exchange effects. The sharp drop off in the energy spectra is due to phase space and energy conservation considerations.

The predictions of the coherent nucleus-nucleus bremsstrahlung model are for a quadrupole angular distribution in the nucleus–nucleus center-of-mass system. Instead, the data support isotropic plus dipole emission in the nucleon–nucleon center-of-mass system. The angular distribution for the deuterium target can be fit with isotropic plus a $\cos(\theta_{cm})$ term. This is expected due to the asymmetry of the currents in the nucleon-nucleon center-of-mass frame.

Although there was no statistically significant asymmetry observed in the data on high energy gamma ray production with polarized protons, there is a strong asym-

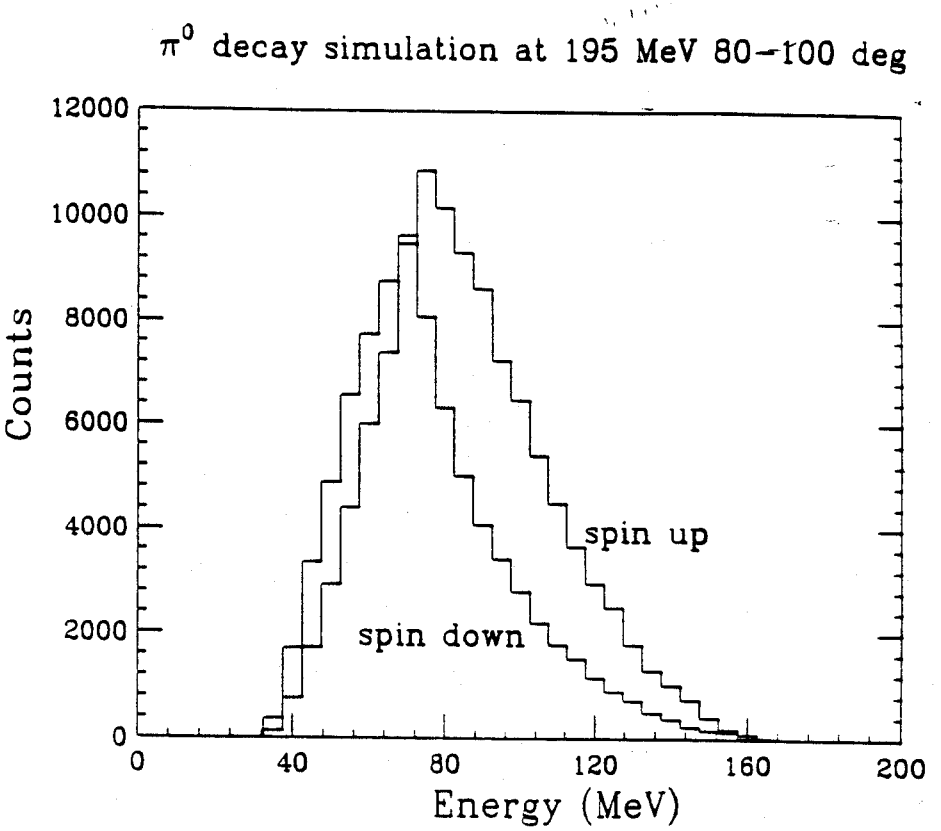

Figure 4.30: The results of a Monte-Carlo simulation on the decay of the π^0 while monitoring the spin information. The simulated energy spectra show the same dependence on the spin information as does the measured data.

metry for the π^0, and even though only one of the photons from the decay of the π^0 is observed, there is still information on the asymmetry available. A simple Monte-Carlo calculation has shown that the observed asymmetry in the 195 MeV data may arise from a doppler shift in the decay of the π^0. Therefore the observed asymmetry in the 195 MeV data is due to the large asymmetry for the π^0.

Chapter 5

Comparison with Other Measured Data

I Introduction

As was mentioned in Chapter 4 one of the main goals of the the IUCF experiment was to check on the discrepancy between the results of Edgington and Rose [Edgington 66] and the work of Kwato *et al.* [Kwato 88a] and Pinston *et al.* [Pinston 89]. In this Chapter direct comparison is made between the measurement described in this work and all of the known data sets on proton–nucleus bremsstrahlung.

A Edgington and Rose

The data published by Edgington and Rose was the first systematic study of proton induced bremsstrahlung. They made extensive investigations of the target mass and angular dependence of high energy gamma rays. In their measurement, Edgington and Rose used a large lead glass detector to detect the photons, and as was pointed out in Chapter 2 of this work, lead glass has poor energy resolution at these energies. One other significant factor was that the detector was operated in an uncollimated mode which would also decrease the overall resolution of their detector system due to lateral leakage of the electromagnetic shower. In Figure 5.1 the energy spectra for several of

the targets used in the Edgington and Rose are displayed. It should be noted that the shape of the spectra reported by Edgington and Rose were exponential which also differs from the shape reported in this work. Figure 5.2 shows a direct comparison of the data measured by Edgington and Rose at an incident proton energy of 140 MeV to the data in this work at 145 MeV. The energy spectra are plotted versus the variable E_γ/E_p which was used in Chapter 4 to compare the data at different bombarding energies. It is clear from Figure 5.2 that the measurement by Edgington and Rose is systematically lower than the data in this work by approximately a factor of 2–3. This is consistent with the value reported by Kwato *et al.* [Kwato 88a] and Pinston *et al.* [Pinston 89]. The angular distributions reported by Edgington and Rose were forward peaked in the laboratory frame and were similar in shape for the reactions p + d, p + C or p + O. The scaling of the cross section with target mass followed a $N/A^{1/3}$ law which is essentially the same as $A^{2/3}$. These features are in agreement with the present data. All of these characteristics led Edgington and Rose to conclude that the origin of the photons is individual neutron–proton collisions. The values for the integrated cross section for gamma rays with energies $E_\gamma \geq 40$ MeV as reported in the paper by Edgington and Rose are listed in Table 5.1. For comparison the total cross section for the present measurement at 145 MeV is also listed in Table 5.1. It should be noted that the total photon cross sections for this work were derived by integrating the double differential cross section at 90° in the laboratory over the energy and transforming the value to the nucleon-nucleon center-of-mass frame. The resulting value is then multiplied by 4π which yields the value reported here. This procedure was used by all of the previous measurements. The mean value for the difference between the values reported by Edgington and Rose and the present measurement is 2.7 ± 1.1, which is in agreement with the discrepancy reported by Kwato *et al.*.

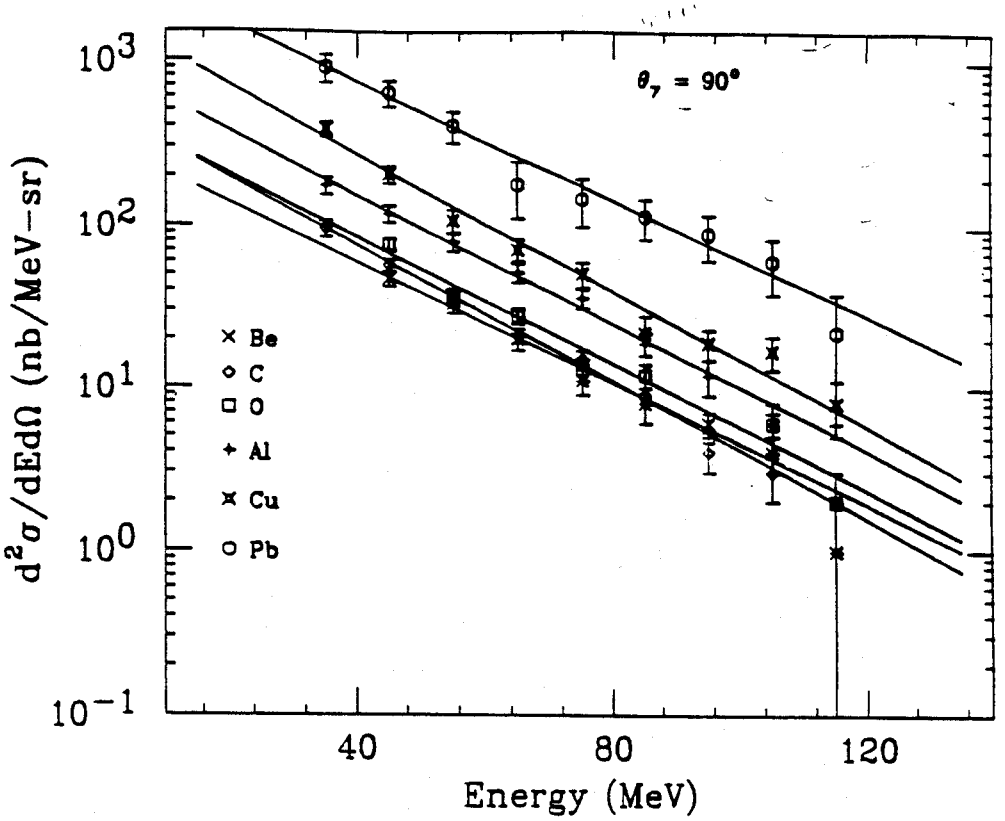

Figure 5.1: The energy spectra for several of the target measured by Edgington and Rose [Edgington 66] at 90 ° in the laboratory frame.

Table 5.1: Comparison of the total cross section for gamma rays with $E_\gamma \geq 40$ MeV from 140 MeV protons on various targets to the present data at 145 MeV. The values for the cross section at 140 MeV are from the work of Edgington and Rose [Edgington 66].

Present Data			Edgington and Rose		
E_p MeV	Target	σ_{tot} μb	E_p MeV	σ_{tot} μb	Ratio
145	^{2}H	21 ± 2	140	4.3 ± 0.3	4.88
145	C	57 ± 6	140	23 ± 3	2.48
145	Zn	282 ± 29	140	80 ± 10 Cu	2.53
145	Pb	612 ± 61	140	224 ± 27	2.73
Mean Value 2.7 ± 1.1					

B Kwato *et al.*

The results from Kwato *et al.* [Kwato 88a] at 72 MeV were the first measurements in recent years to cast doubt on the validity of the Edgington and Rose measurement. In Figure 5.3 the energy spectra for photons from the reaction p + Au at 72 MeV in the laboratory is exhibited. It is apparent from Figure 5.3 that the energy spectra are "harder" for forward emission than for backward emission. This difference in the energy spectra at different angles was one of the indications pointed out in Chapter 4 to be a signature of photon emission from a moving source. The values of the total cross section reported in the paper by Kwato *et al.* were a factor of 2–3 times larger than the values from Edgington and Rose when scaled for bombarding energy. Kwato *et al.* found that the emitting source velocity was the nucleon–nucleon center-of-mass velocity which is in agreement with this work. A direct comparison of the data from Kwato *et al.* to the measured data from this work are made in a plot of the double differential cross section versus E_γ/E_p in Figure 5.4. As opposed to the comparison between the data from Edgington and Rose and the present data, there is reasonable agreement between the data from Kwato *et al.* and the present measurement with

the exception of the carbon target which shows a slight discrepancy. The difference may be due to background problems from fast protons and neutrons in the Kwato *et al.* data. It could also be due a gain shift in the detector which was not corrected for by the experimentalists.

C Pinston *et al.*

In another measurement performed with the same detector system that was used by Kwato *et al.*, Pinston *et al.* studied proton induced bremsstrahlung at incident energies of 168 and 200 MeV on targets of C, Al Cu, Ag, Tb, Au. The measured energy spectra from p + Tb at 168 MeV are shown in Figure 5.5. Again, the spectra are "harder" for the forward angle spectra. The source velocity was extracted from the centroid of the rapidity distribution. The source velocities were found to be very close to the nucleon–nucleon center-of-mass velocity for gamma rays with energies $E_\gamma \leq 85$ MeV. However, they found that for gamma rays with energies $E_\gamma \geq 85$ MeV the source velocity was substantially less than the nucleon–nucleon velocity. The results from Pinston *et al.* are listed in Table 5.2. The trend that the source velocity is reduced for the higher energy gamma rays was discussed previously and is related to the idea that the maximum gamma ray energy requires a collision of the incident proton with a a target neutron having its momentum pointing opposite to the beam direction. An example of the rapidity distribution from Pinston *et al.* is shown in Figure 5.7.

At the beam energies reported by Pinston *et al.* the contribution from π^0 decay is important, and values of 9% and 24% for C and Au at 168 MeV and 46% and 59% for the same targets at 200 MeV have been found. The values reported by Pinston *et al.* and Kwato *et al.* are listed in Table 5.3. Also included in Table 5.3 are the values for the total cross sections from the present work at 104 and 195 MeV, and

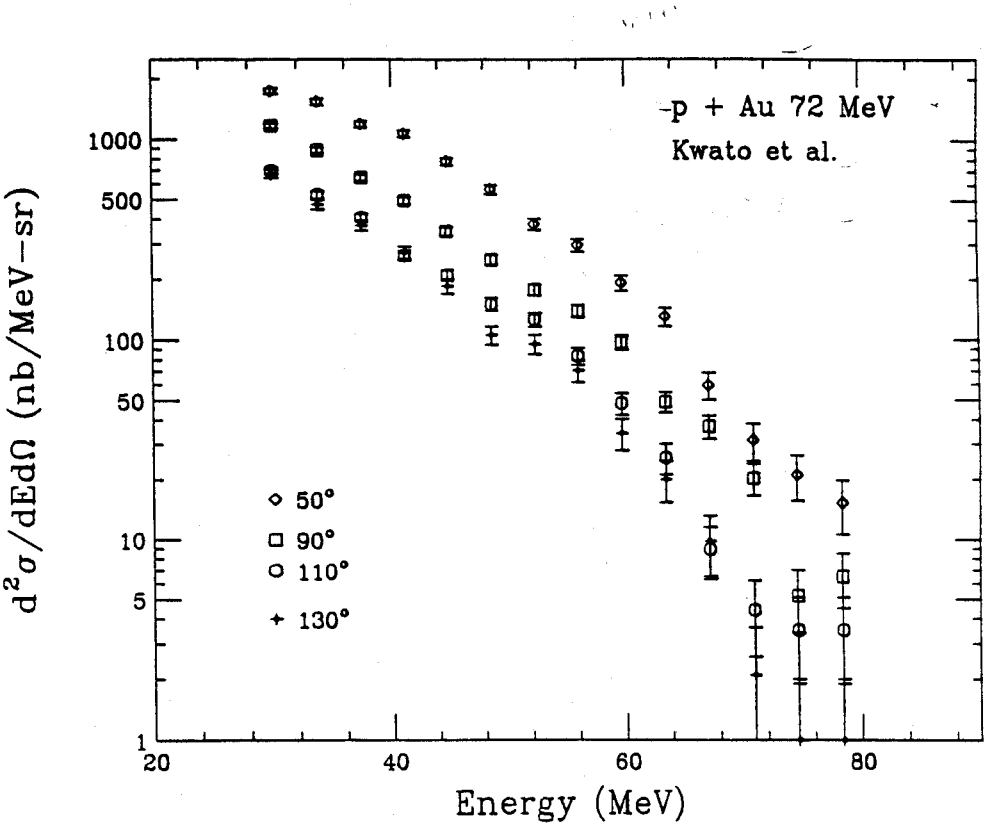

Figure 5.3: The energy spectra for p + Au at 72 MeV measured by Kwato *et al.* at 50°, 90°, 110°, and 130° in the laboratory frame [Kwato 88a].

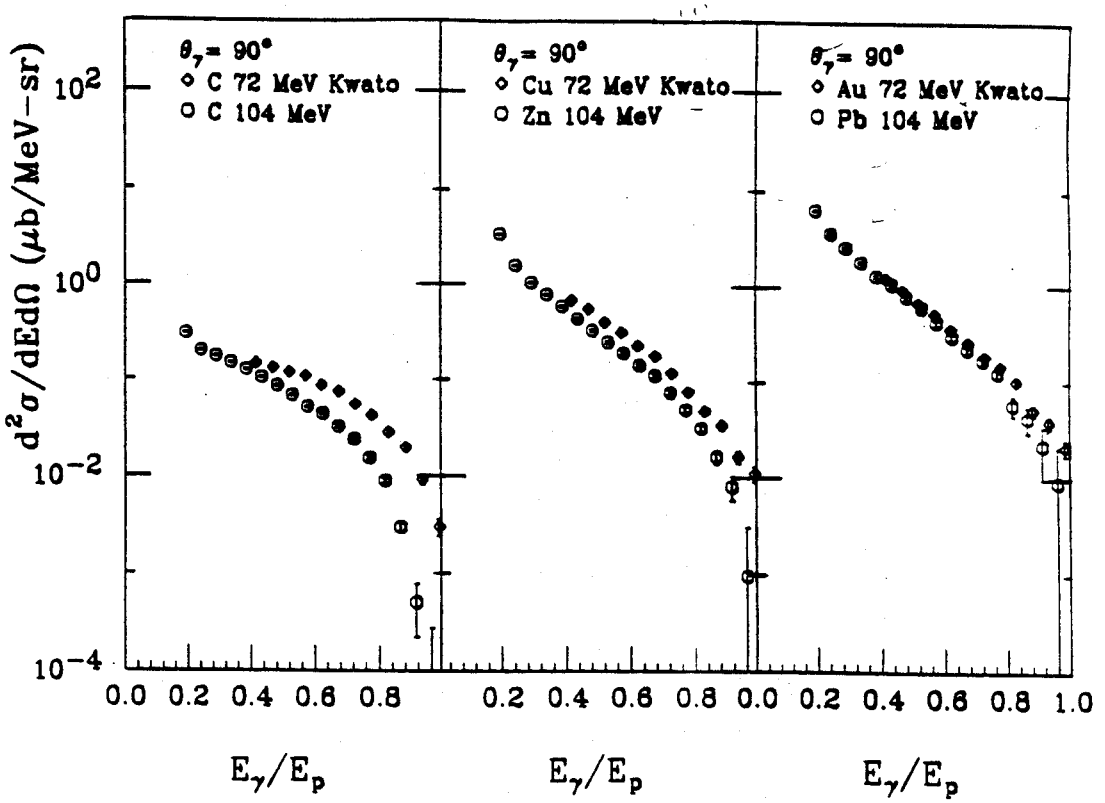

Figure 5.4: A comparison of the energy spectra measured by Kwato *et al.* at 72 MeV to the data in this work at 104 MeV. The spectra are plotted versus a reduced variable E_γ/E_p.

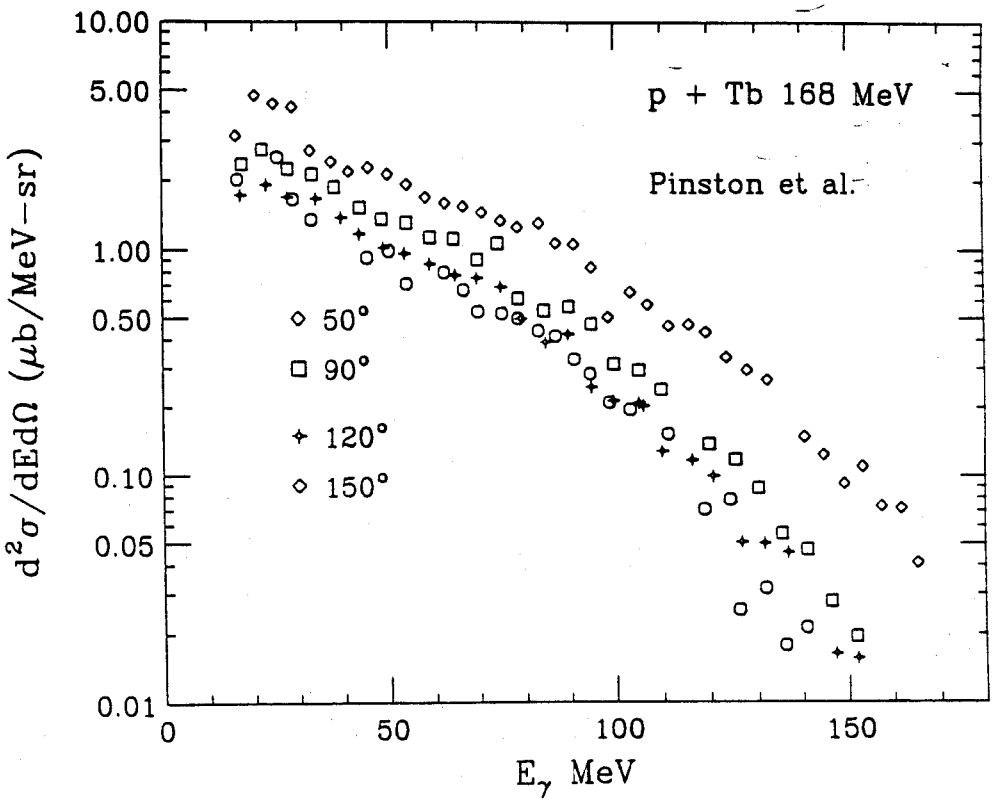

Figure 5.5: Energy spectra in the laboratory frame for the reaction p + Tb at 168 MeV measured by Pinston *et al.* [Pinston 89].

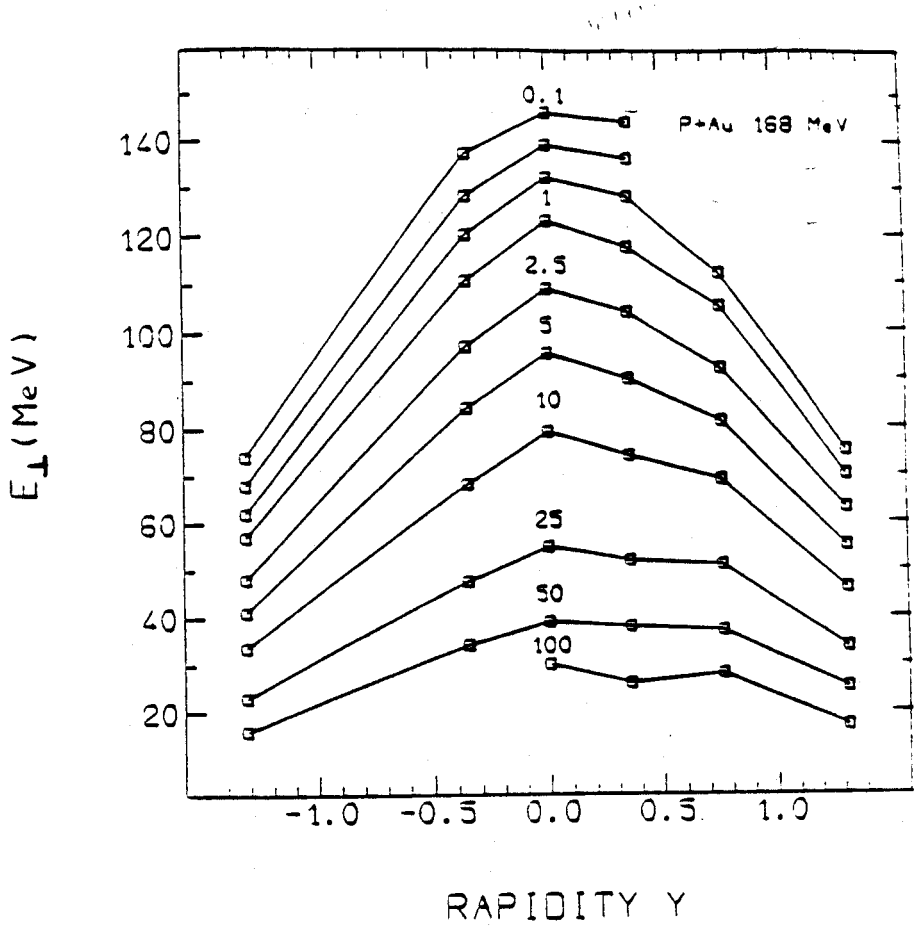

Figure 5.7: Rapidity distributions for high energy gamma rays at an incident proton energy of 168 MeV [Pinston 89].

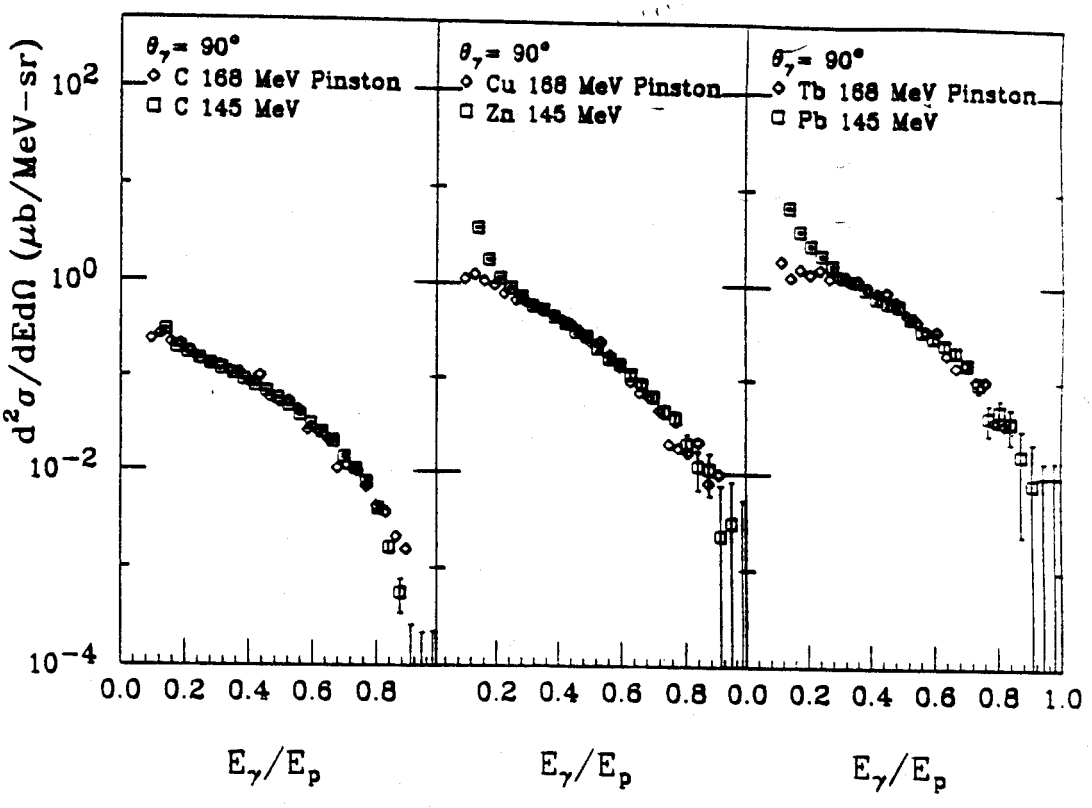

Figure 5.6: A comparison of the energy spectra measured by Pinston *et al.* at 168 MeV to the data in this work at 145 MeV. The spectra are plotted versus a reduced variable E_γ/E_p.

Table 5.2: Source velocities for gamma rays from proton induced reactions at 168 MeV [Pinston 89].

Target	$E_\gamma < 85$ MeV	$E_\gamma > 85$ MeV
C	0.28 ± 0.03	0.28 ± 0.05
Al	0.30 ± 0.03	0.20 ± 0.05
Cu	0.24 ± 0.03	0.18 ± 0.05
Ag	0.20 ± 0.03	0.17 ± 0.05
Tb	0.27 ± 0.03	0.19 ± 0.05
Au	0.22 ± 0.03	0.14 ± 0.05
Mean value	0.25	0.19

it should be noted that the values at 168, 195 and 200 MeV have been corrected for the π^0 contribution. In an attempt to find any trends among all the different targets, Pinston *et al.* used the idea of calculating the probability of gamma ray emission in a neutron–proton collision. As with high energy gamma ray production in heavy-ion reactions [Nifenecker 85] one can adapt those same concepts and arrive at a simple expression for the production cross section for high energy gamma rays. Under the assumption that the gamma rays come from neutron–proton collisions, the production cross section can be written as:

$$\sigma_\gamma = \sigma_R \, P_n \, P_\gamma \tag{5.1}$$

where σ_R is the total reaction cross section [Bauhoff 86,Hess 58]. P_n is the probability of the incident proton to undergo a collision with a target neutron, and P_γ is the probability to produce a single photon in a single neutron–proton collision. From experimental data Hess found that $\sigma_{np} \approx 3\sigma_{pp}$ [Hess 58]. So with this simplification Equation 5.1 can be rewritten and is now:

$$\begin{aligned} P_n &= \sigma_{np} \cdot \frac{N}{N\,\sigma_{np} + Z\,\sigma_{pp}} \qquad (5.2) \\ &= \frac{3N}{3N + Z} \end{aligned}$$

Table 5.3: A comparison of the total cross section of gamma rays above 40 MeV from proton induced reactions at incident energies of 72, 104, 168, 195, and 200 MeV [Kwato 88a,Pinston 89].

Kwato *et al.*		
E_p MeV	Target	σ_{tot} μb
72	C	23 ± 2
72	Cu	59 ± 6
72	Au	94 ± 9
Present Data		
E_p MeV	Target	σ_{tot} μb
104	C	35 ± 4
104	Zn	144 ± 15
104	Pb	327 ± 33
Pinston *et al.*		
168	C	90 ± 9
168	Al	221 ± 22
168	Cu	361 ± 36
168	Ag	606 ± 61
168	Tb	806 ± 81
168	Au	911 ± 91
Present Data		
195	C	179 ± 30
195	Zn	665 ± 120
195	Pb	1695 ± 300
Pinston *et al.*		
200	C	155 ± 32
200	Ag	1049 ± 208
200	Au	910 ± 269

$$\text{therefore } P_\gamma = \frac{\sigma_\gamma}{\sigma_R} \cdot \left(1 + \frac{Z}{3N}\right) \tag{5.3}$$

where N and Z are the neutron and proton number of the target. As expected from the first collision hypothesis the values for P_γ deduced from the total cross sections reported Kwato *et al.*, Pinston *et al.* and the present work are almost independent of the target. The present data are in reasonable agreement with the measurements of Kwato *et al.* and Pinston *et al.* However, the present data at 195 MeV and that of Pinston *et al.* at 200 MeV are not as precise as the lower energy data due to the subtraction of the π^0 cross section. Figure 5.8 shows the probability of gamma emission, P_γ, versus the incident beam energy. This quantity exhibits a linear increase value as the beam energy is raised.

From the theoretical aspect, a recent paper by Nakayama and Bertsch [Nakayama 89c] completed a more refined calculation based on their previous work [Nakayama 86] and found reasonable agreement between the experimental data of Pinston *et al.* and their calculation. In the calculation Nakayama and Bertsch use the first chance neutron–proton collisional mechanism. The elementary nucleon–nucleon bremsstrahlung amplitude is calculated within a meson exchange potential which includes one body as well as two body current contributions. This was an extension of the earlier work of Brown and Franklin [Brown 73]. The quality of the agreement between theory and experiment is displayed in Figure 5.9. Although Nakayama and Bertsch fit the 168 MeV data of Pinston *et al.* their calculation does not do as well in fitting the 72 MeV data from Kwato *et al.*. They found they were not able to fit the strong angular distribution found in the system p + Au at 72 MeV [Kwato 88a]. However, at forward angles the data may contain pile-up between photons and fast protons. This pile-up problem might explain the difference between the prediction of Nakayama and Bertsch and the data of Kwato *et al.* in the high energy portion of the spectrum

[Nakayama 89c].

II The Deuterium Cross Section

This section will deal only with the values of the deuterium cross section which has been experimentally measured by several groups [Edgington 66,Rothe 66,Koehler 67,Pinston 90]. The pdγ reaction makes the transition between the elementary process pnγ and proton-nucleus bremsstrahlung. The pdγ result should serve as a good approximation to the free pnγ value if a correction is made for the neutron momentum distribution inside the deuterium nucleus. The pdγ cross section can also serve as a way to observe the importance of multistep processes and phase space availability for neutron–proton bremsstrahlung in proton–nucleus reactions.

The pdγ experiments that have been reported in the literature were performed by Edgington and Rose [Edgington 66] at 140 MeV, Koehler *et al* at 197 MeV [Koehler 67] and Pinston at 200 MeV [Pinston 90]. There also is a value for pdγ at 148 MeV [Rothe 66] that has been reported in a conference proceedings by the same researchers in the paper by Koehler *et al.* but it was never published in a refereed journal. Edgington and Rose used a (D_2O -H_2O) target subtraction in conjunction with a lead glass detector and obtained a poor resolution gamma ray spectrum. The value of the total cross section for gamma rays above 40 MeV was 4.3 $\pm$ 0.3 μb. Koehler *et al.* used 197 MeV protons incident on a liquid deuterium target. In this measurement photons above 40 MeV were detected in coincidence with one or two charged particles. They found the value for the the pdγ cross section to be 35 $\pm$ 12 μb. In the original paper it was pointed out that there was a large discrepancy between the measurement of Edgington and Rose and their work. However, it was to go unnoticed until much later when the data of Edgington and Rose came under close scrutiny. The measurement

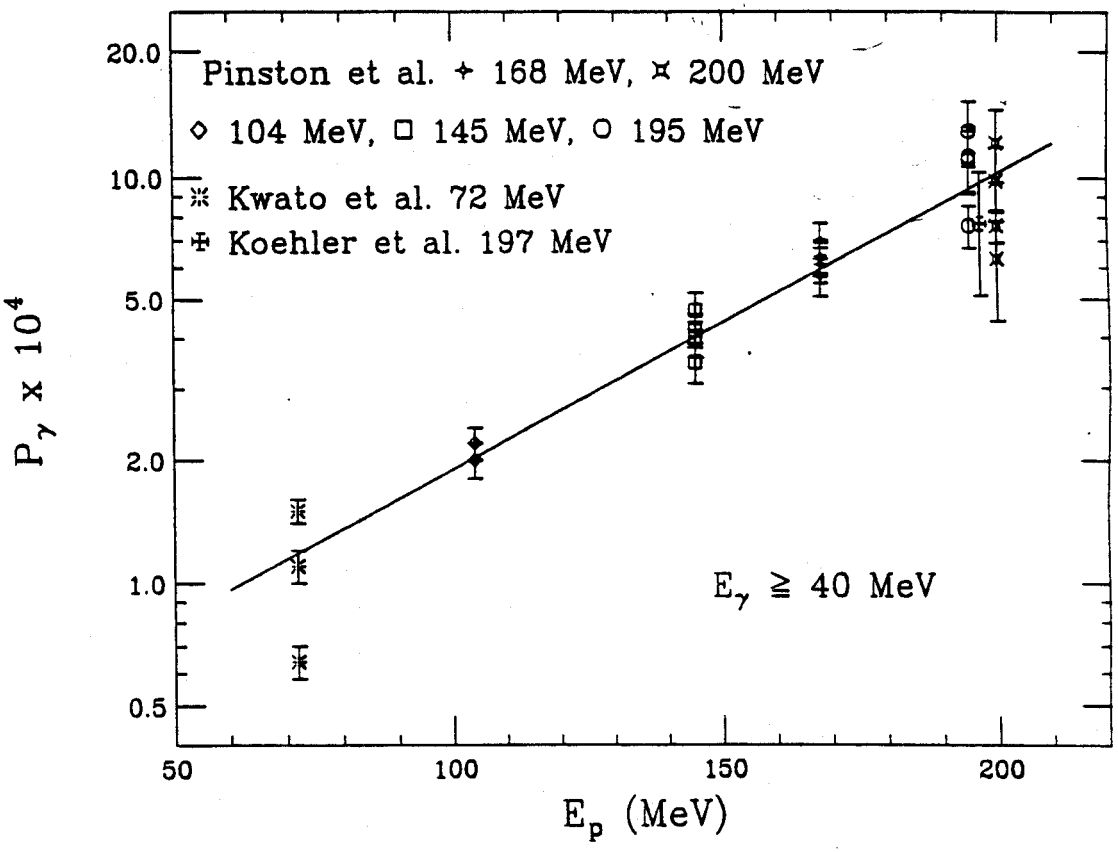

Figure 5.8: A plot of the probability of gamma ray emission in a neutron–proton collision [Pinston 89].

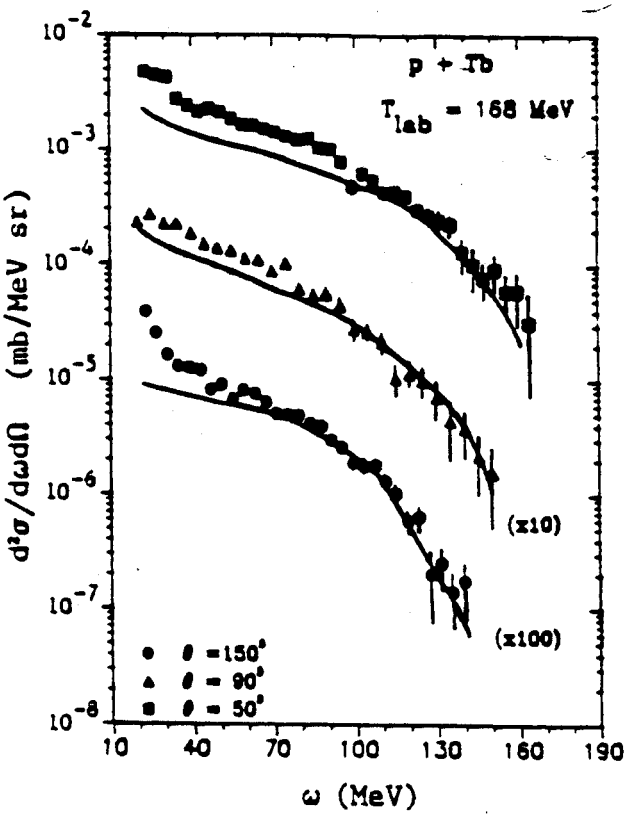

Figure 5.9: Comparison of theoretical calculations from Nakayama and Bertsch [Nakayama 89c] to the system p + Tb at 168 MeV [Pinston 89].

performed by Pinston and co-workers [Pinston 90] used the same technique as in the present experiment to extract the deuterium cross section, namely (CD_2 - C). The detector system employed was the BaF_2 converter + NaI(Tl) telescope previously discussed. Figure 5.10 shows a comparison the carbon spectra measured by Pinston and co-workers and the present measurement. There is reasonable agreement between the two spectra. In Figure 5.11 the spectra for pdγ are displayed, and once again there is reasonable agreement between the two spectra. In Figure 5.12 a comparison of the measured angular distribution from Koehler, Pinston and the present work is displayed. There is reasonable agreement between all the measurements at these energies. The value of the total cross section reported for gamma rays above 40 MeV by Pinston is $\approx$ 34 μb. This value is in excellent agreement with the value that is extracted from the data in this work at 195 MeV which is 34 $\pm$ 4 μb. It should be noted that for the data at 195 MeV in this work and that of Pinston and co-workers at 200 MeV have been corrected for the radiative capture cross section p + d $\rightarrow ^3$He + γ. Pinston and co-workers must also correct for the contribution from π^0 since they are above the threshold energy of 198.7 MeV for the reaction p + d $\rightarrow ^3$He + π^0 [Pikar 81]. This contribution was found to be small less than 10% for gamma rays with energies above 40 MeV. The data of Koehler *et al.* does not correct for the capture cross section, and they may also be complicated by the fact that they are at a incident beam energy near the threshold for π^0 production. The beam energy quoted in the paper by Koehler *et al.* was 197 $\pm$ 5 MeV.

At the lower bombarding energy of 145 MeV the value that is extracted from the data is 21 $\pm$ 2 μb which is 4.7 times larger that the value reported by Edgington and Rose. Rothe [Rothe 66] reported a value of 26 μb for gamma rays with energies greater than 25 MeV. In this measurement Rothe used a degrader to lower the beam energy from 197 to 148 MeV. Although this value is not in perfect agreement with

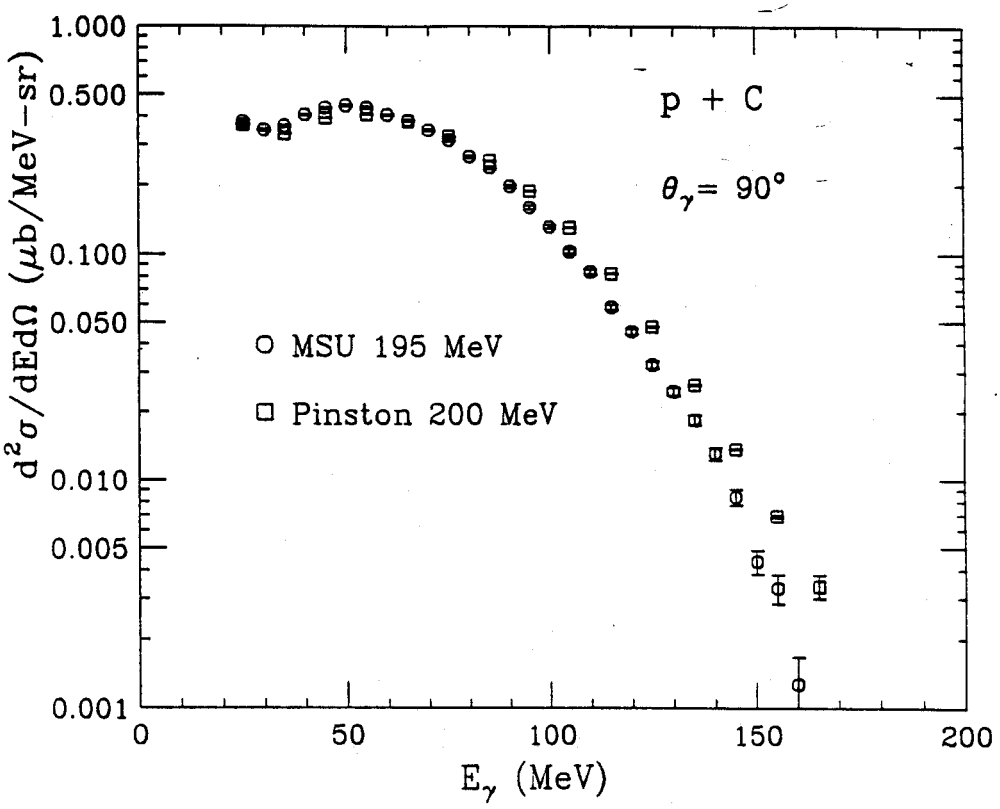

Figure 5.10: A comparison of the energy spectra from protons incident on carbon at 195 and 200 MeV [Pinston 90].

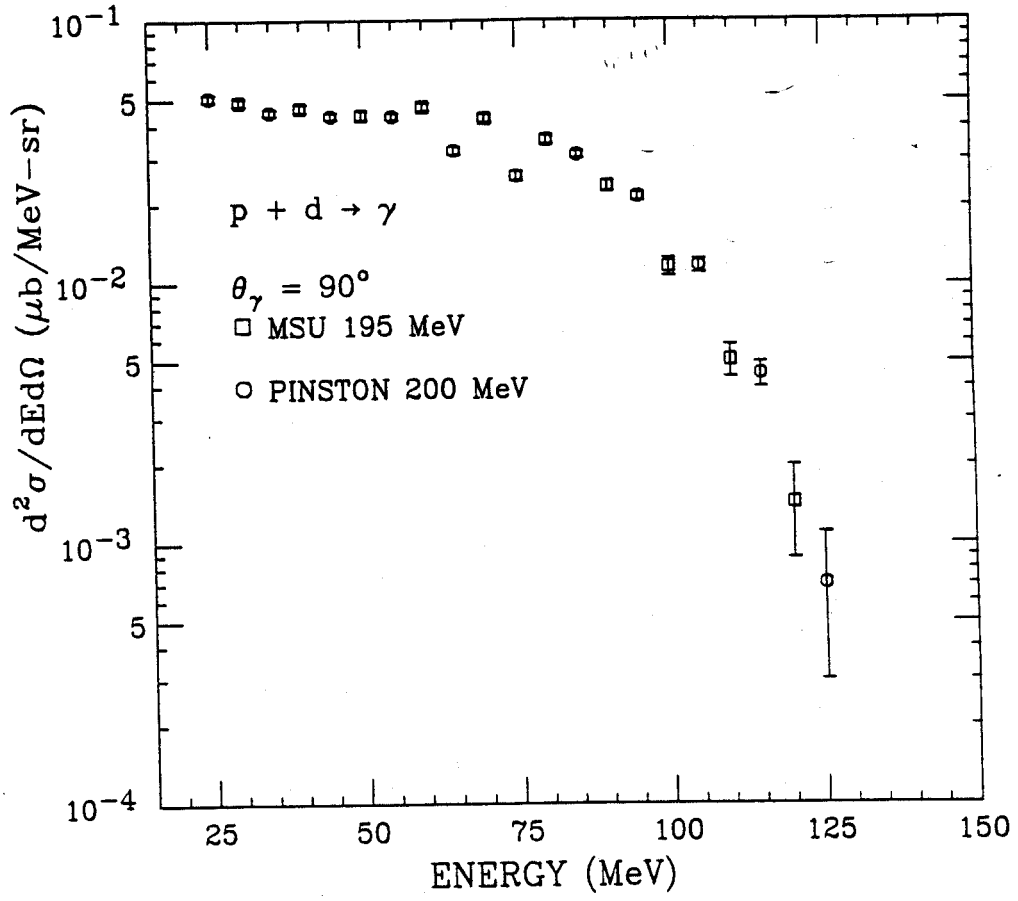

Figure 5.11: A comparison of the energy spectra from protons incident on deuterium at 195 and 200 MeV [Pinston 90].

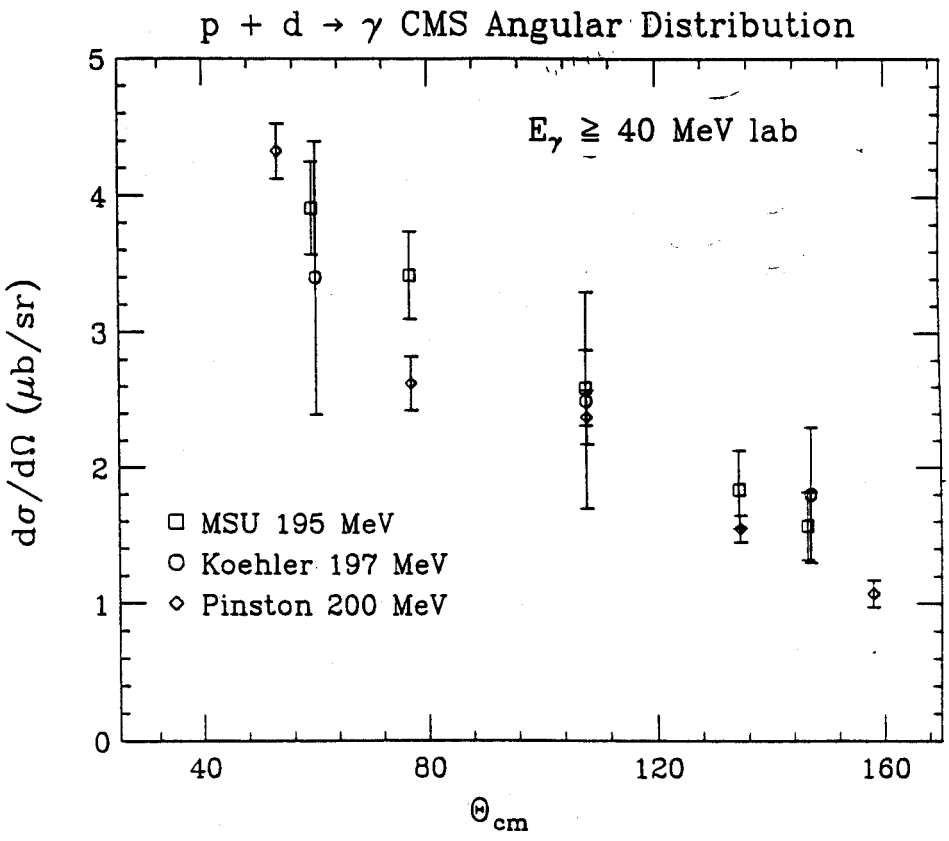

Figure 5.12: A comparison of the energy integrated cross sections for deuterium at 195, 197 [Koehler 67] and 200 MeV [Pinston 90].

Table 5.4: A comparison of the total cross section of gamma rays above 40 MeV from proton induced reactions on deuterium at incident energies of 140, 145, 148, 195, 197, and 200 MeV [Edgington 66,Rothe 66,Koehler 67,Pinston 89].

E_p	Target	σ_{tot}	Author
140	^{2}H	4.3 ± 0.3	Edgington and Rose
145	^{2}H	21 ± 2	Present Data
148	^{2}H	26	Rothe *et al.*
195	^{2}H	34 ± 4	Present data
197	^{2}H	35 ± 12	Koehler *et al*
200	^{2}H	35	Pinston *et al.*

the 145 MeV point in this work it has never been published so it should be viewed with some skepticism. Table 5.4 displays a compilation of all of the cross sections for the reaction pdγ mentioned in this chapter. From the theoretical aspect, in a very recent article Herrmann, Speth and Nakayama [Herrmann 91] calculate neutron–proton bremsstrahlung in a meson-exchange potential model. In this paper a careful treatment of the role of rescattering is completed. It was shown in the paper that this contribution enhances the cross section for photon energies near the maximum value allowed. As a function of the photon energy neutron-proton bremsstrahlung inclusive cross sections are rather flat except in the low photon energy region. Such behavior is exhibited in the data that has been measured at 145 and 195 MeV. They report values for the total cross section for photons of energy greater than 40 MeV to be 14.5 μb at 140 MeV and 22 μb at 197 MeV. In Figure 5.13 a comparison of the calculated value and the experimental value for the energy integrated cross section for gamma rays above 40 MeV in the laboratory is displayed. Figure 5.14 shows a comparison to the double differential cross section for pnγ at 150 and 200 MeV at 30 ° and 90° respectively in the center-of-mass system to the present data. For photons below about 80 MeV there is reasonable agreement with the theory for 200 MeV protons. The value for the lower energy data at 150 MeV is about 65 MeV. The data

at 145 MeV are approximately a factor of 2 higher than the theoretical prediction. The flat line shape is shown in both the calculation and the data at both energies. However, above the energy cutoffs the momentum distribution of the deuteron plays an important role.

III Conclusion

In conclusion the measurements of proton induced bremsstrahlung in this work confirm the earlier discrepancy reported by Koehler *et al.*, Kwato *et al.* and Pinston and co-workers. This new measurement is in strong disagreement with the data of Edgington and Rose and in contrast it is in reasonable agreement with the data from Koehler *et al.*, Kwato *et al.* and Pinston and co-workers. The mean value for the ratio of the present data to the data from Edgington and Rose is 2.7 ± 1.1 which is consistent with the results of Kwato *et al.*. The values for the pdγ cross section at 145 MeV and 195 MeV are in reasonable agreement to the values reported by Koehler *et al.* at 197 MeV and Pinston and co-workers at 200 MeV. The calculations by Herrmann, Speth and Nakayama show reasonable agreement to the data below 80 MeV at an incident energy of 200 MeV, but at higher energies the deuterium spectrum falls off much more slowly due to the internal momentum distribution of the deuteron. The calculation does not agree with the data at 145 MeV, although it has the shape of the low energy portion it differs by about a factor of two in terms of the absolute magnitude. Therefore, a much more detailed calculation is required to fit the energy spectrum at all photon energies for the deuterium case.

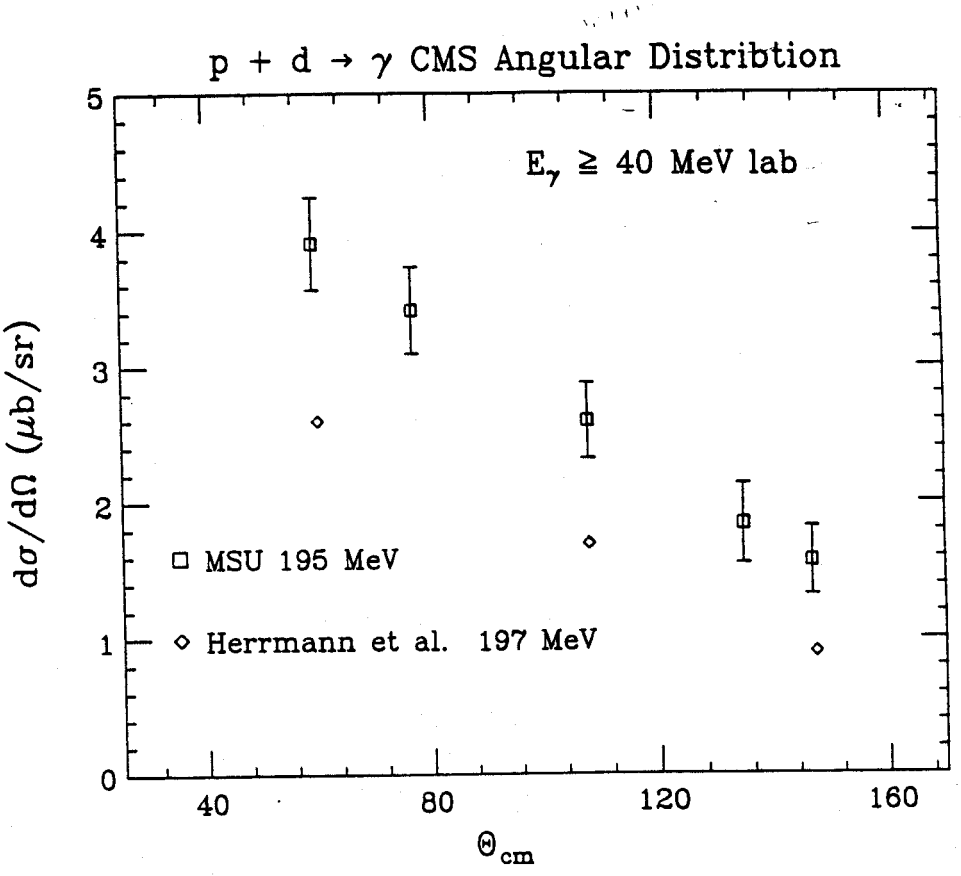

Figure 5.13: Comparison of the calculated angular distribution for 197 MeV protons on deuterium from Herrmann, Speth, and Nakayama [Herrmann 91] to the present data at 195 MeV.

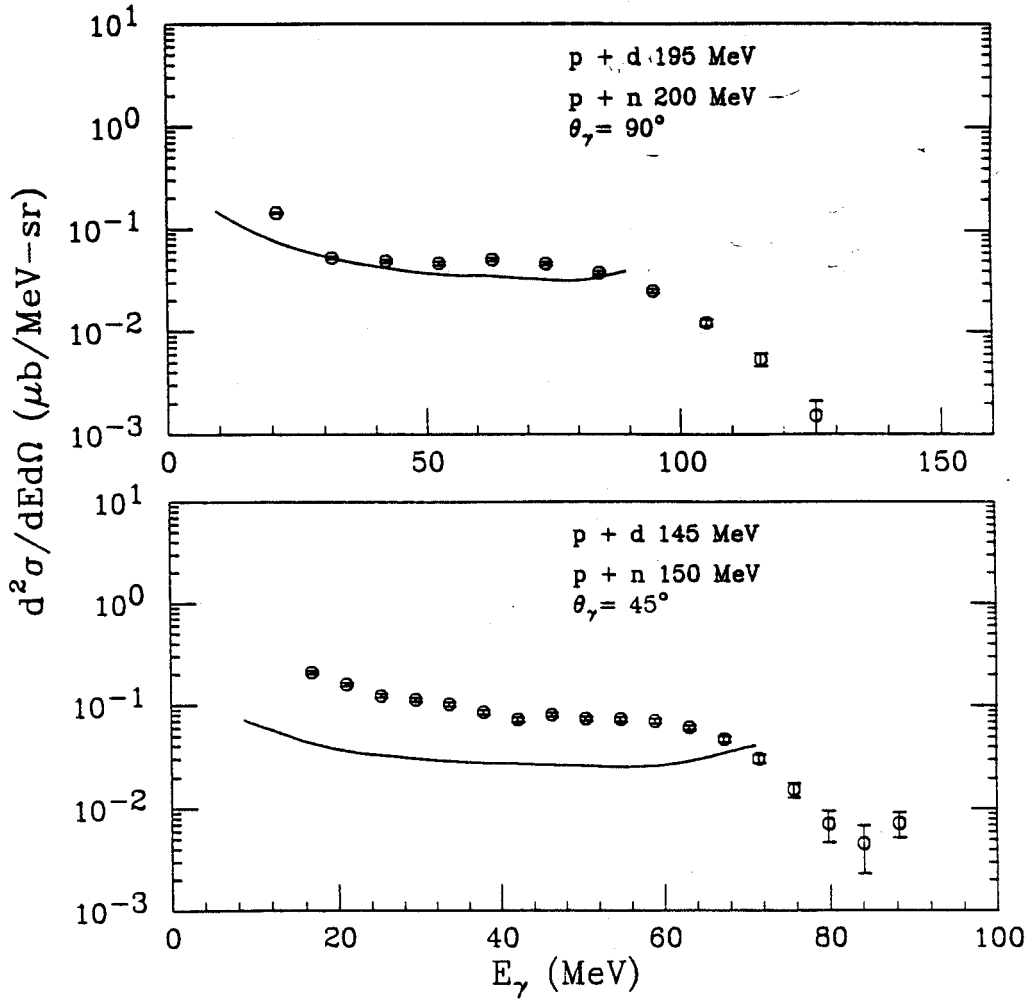

Figure 5.14: Comparison of the calculated energy spectra for 150 and 200 MeV protons on deuterium from Herrmann, Speth, and Nakayama [Herrmann 91] to the present data at 145 and 195 MeV.

Chapter 6

Summary and Conclusions

A new detector system for high energy gamma ray measurements was developed and calibrated using the tagged photon beam at the Saskatchewan Accelerator Laboratory. Detailed Monte-Carlo calculations of the electromagnetic shower were carried out using the electromagnetic shower code EGS4 [SLAC 85]. There is excellent agreement between the EGS4 calculation and the experimental results for the response function of BaF_2 in the energy range from 75 to 200 MeV. A method of transferring the energy calibration from the tagged photon experiment was devised and implemented. This method employs the passage of cosmic ray muons along the diameter of the crystal with the trajectories determined by two 160 cm^2 plastic scintillators placed above and below the crystal. The energy deposition in the BaF_2 crystal for the cosmic ray muons during the calibration was cross checked by using the the electromagnetic and hadronic shower Monte-Carlo code GEANT3.10/3.11 [GEANT 86]. The energy deposited in the BaF_2 by the muons was found to 85 MeV from the GEANT simulation and 81 MeV based on the EGS4 calibration.

The BaF_2 detectors were employed for a measurement of high energy gamma ray production in proton induced reactions. Energy spectra were obtained for high energy gamma rays at angles of 45°, 60°, 90°, 120°, and 135° in the laboratory from protons at 104, 145 and 195 MeV. The protons were incident on targets of CD_2, C, Zn, and

Pb. The double differential cross sections were parameterized for $E_\gamma \geq 35$ MeV with a function of the form:

$$\frac{d^2\sigma}{dEd\Omega} \propto \frac{(E_{max} - E)^\lambda}{E_{max}E_\gamma} \tag{6.1}$$

The general characteristics of this function are that at low energies it must vary like the classical $1/E_\gamma$ while near the maximum energy, it varies quadratically which is determined from the density of states the Fermi Gas Model. To calculate the maximum photon energy in the nucleon-nucleon center-of-mass, the internal momentum distribution of the target nucleons must be taken into account. A least squares fit to all the measured data from each target and beam energy was completed and quantities of interest were extracted.

The angular distributions are all slightly forward peaked in the laboratory frame. The ratio $\sigma(60°)/\sigma(120°)$ at 145 MeV for gamma rays with energies greater than 40 MeV are 2.3, 1.6 and 1.7 for C, Zn and Pb respectively. The source velocities were extracted from contour plots of the invariant cross section versus the the rapidity and the transverse momentum. The centroid of the rapidity was found to be nearly 1/2 the beam rapidity but there was a trend that the source for the highest energy gamma rays was moving at a velocity less than 1/2 the beam rapidity. This can be explained in the framework of incoherent neutron–proton bremsstrahlung as the incident proton with a target neutron with its momentum vector pointing in the direction opposite to the incoming proton. The values for the source velocity extracted from the least squares fit were consistent with photon emission in the nucleon-nucleon center-of-mass system. The fitting procedure also excludes the presence of any quadrupole component in the angular distribution. Instead the angular distribution can be explained by isotropic plus dipole emission. This is consistent with the majority of the theoretical predictions regarding the angular distribution. However, the angular distribution for the deuterium spectra can be fit with an isotropic plus $\cos(\theta_{cm})$ distribution. This

may be due to the asymmetry of the collision.

Although there was no statistically significant asymmetry observed in the gamma ray energy spectra with polarized protons at 104 and 145 MeV. A strong asymmetry for photons arising from the decay of the π^0 was found in the energy spectra at 195 MeV. Such behavior was explained with a simple Monte-Carlo calculation which studied the decay of the π^0 taking into account the spin information of the π^0.

Theoretical models based on first chance neutron–proton bremsstrahlung do a reasonably good job of reproducing the experimental features from heavy-ion data as well as proton induced reactions. In more recent calculations on proton-nucleus bremsstrahlung reactions by Nakayama and Bertsch [Nakayama 89c], the authors found resonable agreement to most to the general features of the bremsstrahlung gamma rays. In the case of pnγ, a very recent paper by Herrmann, Speth and Nakayama [Herrmann 91] made predictions that show resonable agreement at low photon energies to the present pdγ data at 195 MeV. The divergence in the predictions of pnγ and the experimental results on pdγ arise at high photon energies and has been attributed to the the internal momentum distribution of the neutron in the deuterium target. The absolute agreement with the deuterium energy spectrum is not as good at 145 MeV. The calculations differ from the data by approximately a factor of two. However, the shape of the energy spectra are reproduced by the calculation. The deuterium results are important because a complete calculation of this reaction may lead to understanding of the free pnγ results as well as the importance of phase space considerations and multistep processes in proton-nucleus bremsstrahlung reactions. These ideas can then be extended to explain high energy photon production in heavy-ion reaction as well.

References

[Agodi 88] C. Agodi, R. Alba, G. Bellia, R. Coniglione, A. Del Zoppo, C. Maiolino, E. Migneco, P. Piatelli, P. Sapienza and Yan Chen, *Nucl. Instr. and Meth.* **269**,595 (1988).

[Alamanos 86] N. Alamanos, P. Braun-Munzinger, R.F. Freifelder, P. Paul, J. Stachel, T. C. Awes, R. L. Ferguson, F. E. Obenshain, F. Plasil and G.R. Young, Phys. Lett. **173B**, 392 (1986).

[Amaldi 87] U. Amaldi, *Experimental Techniques in High Energy Physics*, Addison-Wesley Co. New York, 332 (1987).

[Ashkin 49] J. Ashkin and R. E. Marshak, *Phys. Rev.* **76**, 58 (1949).

[Bauer 86a] W. Bauer, W. Cassing, U. Mosel, and M. Tohyama, *Nucl. Phys.* **A456**, 159 (1986).

[Bauer 86b] W. Bauer, G. F. Bertsch, W. Cassing, and U. Mosel, *Phys. Rev.* **C34**, 2127 (1986).

[Bauer 87] W. Bauer, T. S. Biro, W. Cassing, U. Mosel, K. Nitta, A. L. De Paoli, G. F. Bertsch tsch, *Proceedings of the XXV international Winter Meeting on Nuclear Physics*, Bormio, Italy, Jan. (1987).

[Bauhoff 86] W. Bauhoff, *Atomic and Nucl. Data Tables* **35**, 429 (1986).

[Beard 85] K. B. Beard, W. Benenson, C. Bloch, E. Kashy, J. D. Stevenson, D. J. Morrissey, J. van der Plicht, B. Sherrill, and J. S. Winfield, *Phys. Rev.* **C32**, 1111 (1985).

[Bellini 89] V. Bellini, M. Bolore, J. Julien, J. M. Hisleur, A. Fallica, A. S. Figuera, R. Fonte, A. Insolia, C. Milone, G. F. Milone, G. F. Palama, G. V. Russo, M. L. Sperduto, and L. Bimbot, *Zeitschrift für Phys.* **A333**, 393 (1989).

[Bertholet 87] R. Bertholet, M. Kwato Njock, M. Maurel, E. Monnand, H. Nifénecker, P. Perrin, J. A. Piston, F. Schusslet, D. Barnèoud, C. Guet and Y. Schutz, *Nucl. Phys.* **A474**, 541 (1987).

[Bertsch 81] G. F. Bertsch and J. Cugnon, *Phys. Rev.* **C24**, 2514 (1981).

[Biro 87] T. S. Biro, *Nucl. Phys.* **A475**, 579 (1987).

[Brown 73] V. R. Brown and J. Franklin, *Phys. Rev* **C8**, 1706 (1973).

[Bonasera 88] A. Bonasera, M. Di Toro and C. Grégoire, *Nucl. Phys.* **A483**, 738 (1988).

[Budiansky 82] M. P. Budiansky, S. P. Ahlen, G. Tarle', and P. B. Price, *Phys. Rev. Lett.* **49**, 361 (1982).

[Cassing 86] W. Cassing, T. Biro, U. Mosel, M. Tohyama, and W. Bauer, *Phys. Lett.* **181B**, 217 (1986)

[Chang 87] T. Chang, D. Yin, C. Cao, S. Wang and J. Liang, *Nucl. Instr. and Meth.* **A256**, 398 (1987).

[Clayton 89] J. Clayton, J. D. Stevenson,W. Benenson, Y. Chen, E. Kashy, A. R. Lampis, M. F. Mohar, D. J. Morrissey, T. K. Murakami, M. Samuel, B. Sherrill, C. L. Tam and J. S. Winfield, *Phys. Rev.* **C40**,1207 (1989).

[Clayton 90] J. Clayton, J. D. Stevenson,W. Benenson, D. Krofcheck, D. J. Morrissey, T. K. Murakami and J. S. Winfield, *Phys. Rev.* **C42**, 1009 (1990).

[DeBenedetti 67] S. DeBenedetti, *Nuclear Interactions* 47 (1967).

[Eadie 71] W.T. Eadie, D. Drijard, F.E. James, M. Roos B. Sadoulet, *Statistical Methods in Experimental Physics* North-Holland Publishing Co. Amsterdam, 81 (1971).

[Edgington 66] J. A. Edgington and B. Rose, *Nucl. Phys.* **89**, 523 (1966).

[Eisberg 60] R. M. Eisberg, D. R. Yennie and D. H. Wilkinson, *Nucl. Phys.* **18**, 338 (1960).

[Eng 86] Scintillation Detector Catalog, Englehard Corp., Solon, OH, pg. 21.

[Englehard Corp. 88] Supplied by Englehard Corp., Solon, OH

[Evans 55] R.D. Evans, *The Atomic Nucleus*, McGraw–Hill Book Co.,New York, 712 (1955).

[Fabjan 82] C. Fabjan and T. Ludlam, *Ann. Rev. Nucl. and Part. Sci.* **32**, (1982).

[Faruki 71] M.R. Faruki and C.F. Swinehart, IEEE Trans. Nucl. Sci. NS-18, 200 (1971).

[Fetter 71] A. L. Fetter, J. D. Walecka, *Quantum Theory of Many–Particle Systems*, McGraw–Hill Book Co., New York, 145 (1971).

[Fox 89] R. Fox, R. Au, and A. VanderMolen, IEEE Trans. Nucl. Sci., 1562 (1989).

[GEANT 86] R. Brun, F. Bruyant, M. Maire, A.C.McPherson, P. Zanarini, *GEANT3 User's Guide* CERN - DD/EE/84-1 (1986).

[Giehl 88] J. Giehl, D. Hauff, J.M. Henneberg, E. Lorenz, G. Mageras and H. Vogel, *Nucl. Instr. and Meth.* **A263**, 392 (1988).

[General Electric Corp] Supplied by General Electric Corp.

[GSI 87] High Energy Photon Collaboration, *Technical Proposal for a Two Arm Photon Spectrometer* (TAPS) GSI Report **87-19** (1987).

[Grosse 85] E. Grosse in *Proceedings of the International Workshop on Gross Properties of Nuclei and Nuclear Excitations XIII*, Hirschegg, Austria, 1985, edited by H. Feldmeier (Gesellschaft für Schweeionenforschung and Institut für Kernphysik, Technische Hochschule, Darmstadt, West Germany 1985 p. 65.

[Grosse 86] E. Grosse, P. Grimm, H. Heckwolf, W. F. J. Mueller, H. Noll, A. Oskarson, H. Stelzer, and W. Roesch, *Europhysics Lett.* **2** 9 (1986).

[Hanold 88] K. Hanold and D.J. Morrissey, *Phys. Rev.* **C38**, 165 (1988).

[Harp 68] G. D. Harp, J. M. Miller and B. J. Berne, *Phys. Rev.* **165**, 1166 (1968).

[Hermann 87] N. Hermann, R. Bock, H. Emiling, R. Freifelder, A. Gobbi, E. Grosse, K.D. Hildenbrand, R. Kulessa, T. Matulewicz, F. Rami, R.S. Simon, H. Stelzer, J. Wessels. P.R. Mairenzig, A. Olmi, A. A. Stefanini, W. Kuhn, V. Metag, R. Novotny, M. Gnirs, D. Pelte, P. Braun-Munzinger, L.G. Moretto, *Phys. Rev. Lett.* **60**, 1630 (1987).

[Hermann 86] N. Hermann, R. Bock, H. Emiling, R. Freifelder, A. Gobbi, E. Grosse, K.D. Hildenbrand, R. Kulessa, T. Matulewicz, F. Rami, R.S. Simon, H. Stelzer, J. Wessels. P.R. Mairenzig, A. Olmi, A. A. Stefanini, W. Kuhn, V. Metag, R. Novotny, M. Gnirs, D. Pelte, P. Braun-Munzinger, L.G. Moretto, GSI Scientific Report, **48** (1986).

[Hermann 84] N. Herrmann, P. Braun-Munzinger, and A. Gobbi, *GSI Scientific Report*, **48** (1984).

[Herrmann 91] V. Herrmann, J. Speth, and K. Nakayama *Phys. Rev C* **C43**, 394 (1991).

[Hess 58] W. N. Hess, *Rev. Mod. Phys.* **30**, 368 (1958).

[Hingmann 87] R. Hingmann, W. Kuhn, V. Metag, R. Muhlahans, R. Novotny, A. Ruchelshausen, W. Cssing, B. Haa Cassing, B. Haas, J. P. Vivien, A. Boullay, H. Delagrange, H. Doubre, C. Gregoire, e, Y. Schutz, *Phys. Rev. Lett.* **58**, 759 (1987).

[Jackson 75a] J.D. Jackson, *Classical Electrodynamics*, J. W. Wiley and Sons, 693 (1975).

[Jackson 75b] J.D. Jackson, *Classical Electrodynamics*, J. W. Wiley and Sons, 705 (1975).

[Jackson 75c] J.D. Jackson, *Classical Electrodynamics*, J. W. Wiley and Sons, 730 (1975).

[Kapusta 77] J. I. Kapusta, *Phys. Rev.* **C15**, 1580 (1977).

[Karle 88] W. Karle, M. Knoop, K.H. Speidel, *Nucl. Instr. and Meth.* **271**, 507 (1988).

[Karwowski 86] H. J. Karwowski, K. Komisarcik, C. Foster, K. Pitts and B. Utts, *Nucl. Instr. and Meth.* **245**, 207 (1986).

[Klamra 88] W. Klamra, T. Lindblad, M. Moszynski, L.O. Norlin and J. Weimer, *Nucl. Instr. and Meth.* **A265**, 485 (1988).

[Knoll 79] G. F. Knoll *Radiation Detection and Measurement* John Wiley and Sons New York, 336 (1979).

[Ko 85] C. M. Ko, G. F. Bertsch, and J. Aichelin, *Phys. Rev.* **C31**, 2324 (1985).

[Koehler 67] P. F. M. Koehler and, *Phys. Rev. Lett.* **18**, 933 (1967).

[Kubota 86] S. Kubota, M. Suzuki, J. Ruan, F. Shiraishi and Y. Takami, *Nucl. Instr. and Meth.* **A242**, 291 (1986).

[Kubota 89] S. Kubota, T. Motobayashi, M. Ogiwara, H. Murakami, Y. Ando J. Ruangen, S. Shirato, T. K. Muraskami, *Nucl. Instr. and Meth.* **A285**, 436 (1989).

[Kwato 86] M. Kwato Njock, M. Maurel, E. Monnand, H. Nifenecker, J. Pinston, F. Schussler, and D. Barneoud, *Phys. Lett.* **175B**, 125 (1986).

[Kwato 88a] M. Kwato Njock, M. Maurel, H. Nifenecker, J. Pinston, F. Schussler, D. Barneoud, S. Drissi, J. Kern, adn J. P. Vorlet *Phys. Lett.* **207B**, 269 (1988).

[Kwato 88b] M. Kwato Njock, M. Maurel, M. Monnand, H. Nifenecker, P. Perrin, J. A. Pinston, F. Schussler and Y. Schutz, *Nucl. Phys.* **A489**, 368 (1988).

[Lampis 88] A. R. Lampis, J. D. Stevenson, W. Benenson, J. Clayton, D. Cebra, Y. Chen, D. Cebra, D. Fox, E. Kashy, D. J. Morrissey, M. Samuel, R. Smith, C. L. Tam, G. D. Westfall, K. Wilson, and J. S. Winfield, *Phys. Rev.* **C38**, 1961 (1988).

[Laval 83] M. Laval, M. Moszynski, R. Allemand, E. Cormoreche, P. Guinet, R. Odru and J. Vacher, *Nucl. Instr. and Meth.* **206**,169 (1983).

[Leo 87] W.R. Leo, *Techniques for Nuclear and Particle Physics Experiments*, Springer-Verlag, New York (1987)

[Lecroy] 2249 W ADC, Lecroy Corp, Spring Hill, NY

[Lorenz 86] E. Lorenz. G. Mageras and H. Vogel, *Nucl. Instr. and Meth.* **A249**, 235 (1986).

[Madey 87] R. Madey, R.M. Sellers, A.R. Baldwin, B.D Anderson, M. Flumley and J. W. Wat- son *Bull. Am. Phys. Soc.*, **32**, 1556 (1986).

[Majewski 85] S. Majewski and D. Anderson, *Nucl. Instr. and Meth.* **241**,76 (1985).

[Matulewicz 90] T. Matulewicz, E. Grosse, H. Emiling, R. Freifelder, H. Grein, W. Henning, N. Herrmann, R. Holzmann, R. Kulessa, R.S. Simon, H.J. Wollersheim, B. Schoch, J. Vogt, M. Wilhelm, J.V. Kratz, R. Schmidt and R.V.F. Janssens, *Nucl. Instr. Meth.* **A289**, 194 (1990).

[Matulewicz 89] T. Matulewicz, E. Grosse, H. Grein, H. Emling, R. Kulessa, F.M. Baumann, G. Domogala and H. Freiesleben, *Nucl. Instr. and Meth.* **274**, 501 (1989).

[Mc Ghan] Supplied by McGhan-Nusil Corp., CA

[Minuit] code *MINUIT*, D506, CERN Program Library

[Murakami 89] T. K. Murakami, W. Benenson, Y. Chen, J. Clayton, C. L. Tam, K. Hanold and M. F. Mohar, Phys. Rev. C **40**, 2079 (1989).

[Murakami 86] T.K. Murakami, J. Kasagi, H. Tachibanaki, K. Yoshida, Y. Shibata, T.Nakagawa M. Ogihara, S. M. Lee, T. Kubo and T. Motobayshi, *Nucl. Instr. and Meth.* **A253**, 163 (1986).

[Murashita 86] M. Murashita, H. Saitoh, K. Tobimatsu, M. Chiba and F. Takasaki,*Nucl. Instr. and Meth.* **243**, 67 (1986).

[Nakayama 89a] K. Nakayama, *Phys. Rev.* **C39**, 1475 (1989).

[Nakayama 89b] K. Nakayama and G. F. Bertsch *Phys. Rev.* **C40**, 1475 (1989).

[Nakayama 89c] K. Nakayama and G. F. Bertsch, *Phys. Rev.* **C40**, 2520 (1989).

[Nakayama 86] K. Nakayama and G. F. Bertsch, *Phys. Rev.* **C34**, 2190 (1986).

[Neuhauser 87] D. Neuhauser, and S. E. Koonin, *Nucl. Phys.* **A462**, 163 (1987).

[Nifenecker 85] H. Nifenecker, and J. P. Bondorf, *Nucl. Phys.* **A442**, 478 (1985)

[Novotny 87] R. Novotny, S. Reiss, R. Hingmann, H. Ströher, R.D. Fisher, G. Koch, W. Kühn, V. Metag, R. Mühlhaus, U.Kneissl, W. Wilke, B. Haas, J.P. Vivien, R. Beck, B. Schoch and Y. Schutz, *Nucl. Instr. and Meth.* **A262**, 340 (1987).

[Particle Data Group 88] Particle Data Group, *Rev. of Part. Prop., Phys. Lett.*, **B204**, 62 (1988).

[Pikar 81] M. A. Pikar, *AIP Conf. Proc* **79**, 541 (1981).

[Pikar 87] M. A. Pikar, H. J. Karwowski, J. D. Brown, J. R. Hall, M. Hugi, R. E. Pollock, V. R. Crups, M. Fatyga, and A. D. Bacher, *Phys. Rev.* **C35**, 37 (1987).

[Pinston 90] J. A. Pinston, D. Barneoud, V. Bellini, S. Drissi, J. Guillot, J. Julien, H. Nifenecker, and F. Schussler, *Phys. Lett.* bf 249B, 402 (1990).

[Pinston 89] J. A. Pinston, D. Barneoud, V. Bellini, S. Drissi, J. Guillot, J. Julien, M. Kwato Njock, M. Maurel, H. Nifenecker, F. Schussler, and J. P. Vorlet, *Phys. Lett.* bf 218B, 128 (1989).

[Prakash 88] M. Prakash, P. Braun-Munzinger, J. Stachel, and N. Alamonos, *Phys. Rev.* **C37**, 1959 (1988).

[Randrup 88] J. Randrup and R. Vandenbosch, *Nucl. Phys.*, **A490**, 418 (1988).

[Remington 87] B. A. Remington, M. Blann, G. F. Bertsch, *Phys. Rev.* **C35**, 1720 (1987).

[Rossi 48] B. Rossi, *Rev. of Mod. Phys.* **20**, 537 (1948).

[Rothe 66] K. W. Rothe, P. F. M. Koehler, and E. H. Thorndike, contribution to the Williamsburg Conference on Intermediate Energy Physics (1966).

[Shyam 86] R. Shyam, and J. Knoll, *Nucl. Phys.* **A448**, 322 (1986).

[Simon 50] A. Simon, *Phys. Rev.* **79**, 573 (1950).

[SLAC 85] *The EGS4 Code System*, W. R. Nelson, H. Hirayama and D. W. O. Rogers, *SLAC-265 UC-32*, Stanford Linear Accelerator Center, Stanford University, Stanford CA, 94305 (1985).

[Stevenson 86] J. D. Stevenson, K. B. Beard, W. Benenson, J. Clayton, E. Kashy, A. Lampis, D. J. Morissey, M. Samuel, R. J. Smith C. L. Tam, and J. S. Winfield, *Phys. Rev. Lett.* **57**, 555 (1986).

[Tam 89b] C. L. Tam, **Ph D. Thesis**, unpublished (1989).

[Tam 89a] C. L. Tam, J.D. Stevenson, W. Benenson, J. Clayton, Y. Chen, E. Kashy, A. R. Lampis, M. F. Mohar, D.J. Morrissey, T.K. Murakami, M. Samuel, B. Sherrill, and J.S. Winfield, *Phys. Rev.* **C39**, 1371 (1989).

[Tam 88] C. L. Tam, J. D. Stevenson, W. Benenson, J. Clayton, Y. Chen, E. Kashy, A. R. Lampis, M. F. Mohar, D. J. Morrissey, T. K. Murakami, M. Samuel, B. Sherrill, and J.S. Winfield, *Phys. Rev.* **C38**, 2526 (1988).

[Vasak 85] D. Vasak, B. Muller and W. Greiner, *J. Phys. G: Nucl. Phys.* **11**, 1309 (1985).

[Vasak 86] D.Vasak, *Phys. Lett.* **176B**, 276 (1986).

[Weidner 81] V. R. Weidner and J. J. Hsia, J. Opt. Soc. Am. **71**, 856 (1981).